

Fluid dynamics of basal entrainment by geophysical gravity-driven flows

THÈSE N° 6765 (2015)

PRÉSENTÉE LE 9 OCTOBRE 2015

À LA FACULTÉ DE L'ENVIRONNEMENT NATUREL, ARCHITECTURAL ET CONSTRUIT
LABORATOIRE D'HYDRAULIQUE ENVIRONNEMENTALE
PROGRAMME DOCTORAL EN MÉCANIQUE

ÉCOLE POLYTECHNIQUE FÉDÉRALE DE LAUSANNE

POUR L'OBTENTION DU GRADE DE DOCTEUR ÈS SCIENCES

PAR

Belinda Margaret BATES

acceptée sur proposition du jury:

Prof. F. Gallaire, président du jury
Prof. C. Ancey, directeur de thèse
Prof. J. McElwaine, rapporteur
Prof. A. Mangeney, rapporteuse
Dr B. Sovilla, rapporteuse



ÉCOLE POLYTECHNIQUE
FÉDÉRALE DE LAUSANNE

Suisse
2015

The strongest argument proves nothing so long as
the conclusions are not verified by experience.
Experimental science is the queen of sciences,
and the goal of all speculation.
— Roger Bacon, c. 1267



Acknowledgements

First of all I would like to thank my thesis supervisor and academic guide, Prof. Christophe Ancey. I am lucky to have had such a trusting and open-minded supervisor, who is not only academically rigorous but also approachable and generous with his time.

Thank you to the members of my examining Jury: François Gallaire, Jim McElwaine, Anne Mangeney and Betty Sovilla, for travelling to Lausanne and for their careful evaluation of this thesis and their valuable comments.

This thesis would not have been possible without the help of Bob, Nicolas and Gaël, without whom I would never have found my way around the lab. As my predecessor, Nicolas developed much of the experimental set-up which was used for the project, and was always available to help, even after leaving EPFL. Bob's can-do attitude has been essential, not only in helping to accomplish many parts of the project, but also in lifting my spirits when I needed motivation.

I am grateful for the warm welcome I received at the LHE, especially from François and Joris, who invited me everywhere and quickly introduced me to life in Lausanne. Thanks also to Barbara, for your kindness and support, and to the others at the LHE.

Since arriving in Lausanne I have been lucky to have support from a wide network of friends: my various housemates, and the friends I have made thanks to them. The girls at Lausanne Netball for my weekly dose of running around and speaking English. The guys that I've met through climbing and skiing, thanks for being so inclusive even though my schedule is pretty erratic. My friends at EPFL, thanks for the mutual support in finishing our PhDs.

Thank you also to my friends and family from the UK, who supported my decision to go abroad to do a PhD, especially those who have been to visit, and to those who haven't – you are always welcome. Finally thank you to Pierre who has been so incredibly supportive in my adjustment to Swiss life and in every problem I have faced, and with whom I have shared many of the best moments.

Lausanne, 1st September 2015

B. B.



Abstract

Geophysical gravity-driven flows – including avalanches, debris flows, pyroclastic flows and submarine turbidity currents – are multiphase natural hazards that flow under the influence of gravity. Despite their differences, they share much of the same physics, having the potential to pick up material from beneath, a process called basal entrainment during which the flow may increase in volume and velocity manyfold. Due to their complexity and unpredictability there are still many unanswered questions about their mechanics, so that many of the theoretical models in use are based on insufficient data sets and may not apply to a general case.

Here, basal entrainment by geophysical gravity-driven flows is studied by isolating the process in idealised laboratory experiments. The avalanche is simplified and controlled in such a way that any changes can be confidently attributed to the entrainment process alone. Further, the methods available in the laboratory allow the continuous, passive study of entrainment, so that for the first time full data sets of internal measurements are obtained, from experiments ranging from simple to complex. The data obtained is easily exploited for confirmation of the mathematical models developed in this thesis.

Experiments which simulated entraining avalanches as Newtonian dam-breaks along a horizontal flume and as viscoplastic dam-breaks along an inclined flume both showed an increase in front position, dependent on the amount of material available, amongst other changes. The experimental results allow the development of a theoretical thin-film model in both cases which is solved numerically and compares favourably with the data obtained. The Newtonian model reproduced the flow characteristics excellently and the viscoplastic model successfully simulated the effects of entrainable material. The possibility of performing similar experiments using a granular suspension is also investigated, with promising results.

This work shows that the effect of entrainment on gravity-driven flows can be quantified and modelled mathematically as a non-local transport process. This has implications for hazard modelling: if the quantity of available loose material is known, and its characteristics are similar to those of the flowing avalanche, the avalanche and the entrainable bed can be modelled as a continuous flow over a rigid base. Thus it is suggested that the models developed be tested in more realistic cases, e.g. in the case of an avalanche entraining material with different characteristics, or in a more complex geometry, in order to better mimic what happens in nature.

Acknowledgements

Key words: Gravity-driven flows, avalanche, debris-flow, entrainment, experimental fluid dynamics, mathematical modelling, lubrication theory



Résumé

Les courants de gravité géophysiques – y compris les avalanches, les laves torrentielles, les coulées pyroclastiques et les courants de turbidité sous-aquatiques – sont des catastrophes naturelles multiphasiques qui coulent sur des pentes sous l'effet de la gravité. Malgré leurs différences, leurs comportements physiques se ressemblent, et ils ont la capacité d'entraîner des matériaux du substrat, un processus au cours duquel le volume et la vitesse peuvent s'accroître fortement. En raison de leur complexité et leur imprévisibilité, il existe encore des questions clés au sujet de leur mécanique qui restent sans réponse, de sorte que la plupart des modèles théoriques utilisés sont basés sur un nombre insuffisant des données et peuvent ne pas appliquer à un cas général. Ici, l'entraînement de matière par des courants de gravité géophysiques s'étudie en isolant le processus dans des expériences idéalisées de laboratoire. L'avalanche est simplifiée et contrôlée de manière à ce qu'un changement de comportement puisse être attribué directement au processus d'entraînement. En outre, les méthodes disponibles en laboratoire permettent la visualisation continue et non-intrusive de l'entraînement, afin d'obtenir pour la première fois des ensembles de mesures internes, à partir d'expériences allant du simple au complexe. Les données obtenues sont facilement exploitées pour la validation des modèles mathématiques développés dans cette thèse.

Afin de simuler l'entraînement par des avalanches, des expériences ont été conçues au cours desquelles une rupture de barrage libère du fluide newtonien dans un canal horizontal, ou du fluide viscoplastique dans un canal incliné. Une augmentation de la position du front de l'avalanche, qui dépend de la quantité de fluide disponible, a été observée dans les deux cas. Les résultats expérimentaux mènent au développement d'un modèle théorique à couches minces dans les deux cas, qui est résolu numériquement et qui reproduit directement les données obtenues. Le modèle newtonien reproduit les caractéristiques d'écoulement de façon excellente et le modèle viscoplastique simule avec succès les effets de la matière entraînée. La possibilité de réaliser des expériences similaires en utilisant une suspension granulaire est également étudiée, ce qui ouvre des perspectives prometteuses.

Ce travail montre que l'effet de l'entraînement sur un courant de gravité en laboratoire peut être quantifié et modélisé mathématiquement de manière globale. Cela aura des implications pour la modélisation des risques : si la quantité de matière disponible est connue, et ses caractéristiques sont similaires à celles de l'avalanche qui coule, l'avalanche et la couche entraînable peuvent être modélisées ensemble comme écou-

Acknowledgements

lement continu sur un fond rigide. Ainsi, il est suggéré que les modèles développés soient testés dans des cas plus réalistes, par exemple, dans le cas d'une avalanche qui entraîne de la matière avec des caractéristiques différentes, ou dans une géométrie plus complexe, afin de mieux simuler ce qui se produit dans la nature.

Mots clefs : courant de gravité, avalanche, lave torrentielle, entraînement, mécanique des fluides expérimentale, modélisation mathématique, théorie de lubrification



Contents

Acknowledgements	i
Abstract	iii
List of figures	ix
List of tables	xiii
1 Introduction	1
1.1 Experimental observations of avalanches and debris flows	2
1.2 Modelling avalanches and debris flows	4
1.3 The problem of entrainment	5
1.4 Contribution	7
2 Experimental Facility and Techniques	9
2.1 Equipment	9
2.2 Experimental campaign 1: Newtonian fluid	12
2.3 Experimental campaign 2: Viscoplastic fluid	13
2.4 Experimental campaign 3: Granular Suspension	17
2.5 Error quantification	19
3 Theoretical models for thin-films	21
3.1 Newtonian dam breaks	22
3.2 Viscoplastic gravity-driven flows	23
3.3 Flows of granular suspensions	26
4 Entrainment by Newtonian Dam-Breaks	31
4.1 Experimental results	31
4.2 A model for entrainment by Newtonian gravity-driven flows	38
4.3 Numerical solution	41
4.4 Discussion	45
5 Entrainment by Viscoplastic Avalanches	49
5.1 Experimental results	49
5.2 A model for entrainment by viscoplastic gravity-driven flows	59
	vii

Contents

5.3	Numerical solution	61
5.4	Discussion	67
6	Entrainment by Granular Suspensions	71
6.1	Experimental results	71
6.2	Discussion	77
7	Discussion and Outlook	79
7.1	Summary	79
7.2	Suggestions for future work	81
	Glossary	83
	Bibliography	96
	Curriculum Vitae	99



List of Figures

1.1	Restaurant damage at St Gingolph (20minutes/lecteur reporter 2015); Uprooted trees by debris flows in the River Uina, Grisons (B. Bates 2014); Destroyed chairlift at St Francois de Longchamp, France (C. Ancey 2012)	2
1.2	A guide to reading this thesis.	8
2.1	Experimental set-up including reservoir, lock-gate, step and entrainable bed layer, and the location of the laser sheet. The flow is in motion at slope angle θ and the bed dimensions are l_{bed} long by δh deep.	10
2.2	a) Optical set up with laser, mirrors, lens and rod for creation of vertical laser sheet; b) prism to film interior of flow from below.	10
2.3	Images from Cameras 1 and 3 (top) and camera 2 (bottom) during vis- coplastic experimental campaign.	11
2.4	Shear stress versus rate of strain graph for clear and blue-dyed Carbopol Ultrez 10 at 0.3% concentration.	14
2.5	Sample image of PMMA beads after sieving, and their grain size distri- bution.	18
2.6	Refractive index-matched suspension versus an aqueous suspension: transmission of a laser beam.	19
4.1	Clockwise, from top right: Space-time plot of flow front from camera 2; Front position against time – comparison of entrainable bed depths; Comparison of bed locations; Comparison of entrainable bed lengths.	32
4.2	Top: Comparison of raw images from runs A (no entrainment) and G; Bottom: Surface height evolution in runs A and G. Measurements taken at 0.6 s intervals.	33
4.3	Influence of entrainment on upstream surface height profiles: i) Moment of contact with bed, t_e ii) $t_e + 1.2$ s iii) $t_e + 6$ s iv) $t_e + 12$ s.	34
4.4	Flow front position with time for experiment G: measurements from camera 2 supplemented with measurements from camera 3.	34
4.5	Left: 3mm-deep bed, configuration “C” for surface identification and PIV data. Right: 6mm-deep bed, configuration “R” for interface identification.	35
4.6	Schematic to show the displacement of the entrainable bed by the in- coming avalanche.	35

List of Figures

4.7	Contour plots for horizontal and vertical velocity after 1 s with velocity vectors. In the vertical velocity plots the positive velocity vectors are highlighted in red. Top: 3 mm step, bottom: 6 mm step.	36
4.8	Velocity profiles in 6 mm deep bed, after 1 s flow.	36
4.9	Progression of $d_{max}(t)$ (dimensionless) for 3 mm and 6 mm deep beds. A power law has been fitted to each set of data to guide the eye. The parameters are $\{A_3, B_3, C_3\} = \{-0.0070, -0.573, 0.186\}$ and $\{A_6, B_6, C_6\} = \{-0.0155, -0.6, 0.334\}$	37
4.10	Progression of $x_F(t)$ for 3 mm (left) and 6 mm (right) beds. The two data sets correspond to two different experiments.	37
4.11	Current enters entrainable zone of length 0.5, progression from $t = 0$ to $t = 4.4984$ (60 s dimensional time). Profiles are plotted every 4 s or 0.3 dimensionless time. Top to bottom: Bed depth $\delta h = 0$, Huppert solution; $\delta h = 3 \text{ mm}/H$; $\delta h = 6 \text{ mm}/H$	41
4.12	Comparing the numerical and experimental results for front progression in experiment G.	42
4.13	Contour plots for modelled non-dimensional velocities (u, w) inside the entraining avalanche, $l_{bed} = 1/2$. a) $u, d = 3 \text{ mm}, t = 0.075$ (1 s); b) $u, d = 6 \text{ mm}, t = 0.075$; c) $w, d = 3 \text{ mm}, t = 0.075$; d) $w, d = 6 \text{ mm}, t = 0.075$; e) $u, d = 3 \text{ mm}, t = 4.4984$ (60 s); f) $u, d = 6 \text{ mm}, t = 4.4984$	43
4.14	Velocity profiles in 6 mm deep bed, after 1 s flow: comparison between PIV measurements (solid lines and arrows) and model predictions (dashed lines)	44
4.15	Current/bed interface for modelled flows over an entrainable bed after 4 s dimensional time. Left: $\delta h = 3 \text{ mm}/H$; Right: $\delta h = 6 \text{ mm}/H$. Rigid base function shown in black.	44
4.16	Progression of the current/bed interface (left: $\delta h = 3 \text{ mm}/H$; right: $\delta h = 6 \text{ mm}/H$). Top: d_{max} , maximum interface depth (the stepped shape is due to the grid resolution). Bottom: $x_F(t)$, interface front.	45
4.17	Left: Front progression with time, $x_N(t)$ for a range of bed-depths, $l_{bed} = 0.5$ over 100 s dimensional time. The dimensional bed depths b_i are $\{0, 0.5, 1, 2, 3, 4, 5, 6, 7, 8, 9\}$ mm, corresponding to lines shaded from dark to light. Right: Log-log plot of front advancement with time, $\Delta X_i(t) = x_{N,i}(t) - x_{N,0}(t)$, for a bed of i mm compared with no bed. The initial progression is fitted by $\log \Delta X_i(t) = 5/9 \log t + C_i$, where $C_i \approx \log(3.174 \max b_i ^{1.646})$	46
5.1	Time-space plots from camera 2, showing front progression and bed position. Experiments 16-3Cc & 16-6Cc.	50
5.2	Experiments 20-0a and 20-6Ca. a: entry time, $t = t_e$. b: $t = t_e + 45 \text{ s}$. c: $t = t_e + 112.5 \text{ s}$. d: $t = t_e + 202.5 \text{ s}$. e: $t = t_e + 315 \text{ s}$	50

5.3	(a) Front position with time for flows over entrainable beds of increasing depth: 16° slope, 30 cm-long bed as indicated by arrow. (b) Front position with time for flows over entrainable beds of increasing lengths, indicated by arrows. 6-mm deep bed at 20°. (c & d) Comparing front position between entraining and non-entraining flows for different slopes.	51
5.4	L: Progression of surface profile including surface irregularity (stars) originating from the original dam-break front. 6 mm deep by 30 cm long bed at 20°. R: Difference in surface height profiles, avalanche flowing over entrainable bed (experiment 20-6Ca, light colour) versus avalanche on a rigid base (20-0a, dark colour).	52
5.5	Schematic to show the displacement of the bed by the incoming avalanche.	53
5.6	Entrainment illustrated using a sequence of raw images and velocity vectors. 6 mm deep by 30 cm long bed at 20°. Surface indicated to exclude refraction effects.	54
5.7	a – d: Velocity profiles for 16° slope, $l_{step} = 90$ cm, comparison between entraining (16-6Cb) and non-entraining (16-0b) cases at $t=34$ s and $t=114$ s. e – h: Velocity profiles for 24° slope, comparison between entraining and non-entraining cases at $t=2.25$ s and $t=5.5$ s.	55
5.8	Velocity fields for horizontal (L) and vertical (R) velocity components. 16-6Ca: 16° slope, 6 mm deep by 30 cm long bed. Plotted at times 10.5 s (top) and 24 s (middle) after front entry into bed. Velocities and lengths non-dimensionalised. Bottom: equivalent non entraining flow after 24 s.	56
5.9	Velocity fields for horizontal (L) and vertical (R) velocity components. (a & b) 12-6Ca, 12°, bed at 70 cm, (c & d) 16-6Cc, 16°, bed at 70 cm, (e & f) 16-6Cd, 16°, bed at 90 cm, (g & h) 24-6Ca, 24°, bed at 90 cm.	57
5.10	L: Raw images showing different interface shapes for 12° and 24° slopes. R: plotting the interface intrusion - maximum downstream point x_F plotted against maximum interface depth d_{max} . N.B. for 12° and 16° the bed was located at $l_{step} = 70$ cm and for 20° and 24° the bed was located at $l_{step} = 90$ cm.	58
5.11	A reproduction of figure 5.3 (c & d), showing the numerical solution overlaid by experimental observations.	61
5.12	Comparison of surface height profiles for front travelling over entrainable bed, 6 mm-deep at 20°. For qualitative comparison only – times do not correspond. Experiment 20-6Ca.	63
5.13	Comparison of surface height profiles (solid line) and yield surfaces (dashed line) for flows travelling over entrainable beds 3 (L) and 6 mm-deep (R). From top to bottom: flow front at 90 cm, bed at 70 cm for 12° and 16°; flow front at 110 cm, bed at 70 cm for 16°; flow front at 105 cm, bed at 90 cm for 16°, 20° and 24°; flow front at 130 cm, bed at 90 cm for 20° and 24°.	64
5.14	A sample of modelled velocity fields for experiment 20-6Ca.	65

List of Figures

5.15	Difference in front position between entraining and non-entraining flows $\Delta X_i(t) = x_{N,i}(t) - x_{N,0}(t)$. Top: 20° , different bed depths (1-9 mm) and bed lengths (10, 20, 30 or 50 cm); Middle: 20° , different bed depths and bed lengths – later time; Bottom: different slopes: 12° and 16° with $l_{step} = 70$ cm, 16° , 20° and 24° with $l_{step} = 90$ cm.	66
5.16	Bed buckling on a 12° slope, L: 3 mm deep bed. R: 6 mm deep bed. . .	68
6.1	Raw images from Camera 1. Top: 3.8 kg released on a slope of 12° , 6 mm-deep bed. Middle: 3.25 kg released on a slope of 12° , 3 mm-deep bed. Bottom: 3.8 kg released on a slope of 16° , 3 mm-deep bed	72
6.2	Velocity profiles. L: Run 16-3b, at times (im 320 and 1020) R: Run 16-6a , at times (im 420 and 1500). In all images the dotted grey line shows a limit above which the image is significantly blurred. Velocities averaged over 5 timesteps.	73
6.3	Images converted to velocity field using PIV. Experiment 16-3b.	74
6.4	Front progression during entrainment. The entrainable bed begins on the left and is 30 cm long. Top: Bird's eye view: The three dark lines show three of the pressure sensors, at 3.5, 7 and 10.5 cm from the beginning of the bed. Bottom: Time-space images from camera 1 show a line of pixels in the entrainable bed, for experiments 12-6c (L) and 16-6a (R). .	75
6.5	Schema showing a recirculation zone being set up due to a concentration difference in the bed. Lighter = less concentrated.	76
6.6	Differential pressure sensor signals, showing arrival of the front.	76



List of Tables

2.1	Experiments performed using glycerol	13
2.2	Viscoplastic experiments performed: dyed with Methylene Blue	15
2.3	Viscoplastic experiments performed: seeded for PIV	17
2.4	Suspension experiments performed.	19



1 Introduction

In Switzerland, debris flows account for around 4.5 % of storm-related damage, amounting to 350 million EUR over the period 1972-2007 [1], and every year around 25 avalanche deaths are reported¹. In the notorious Winter of 1999, around 1 billion CHF of direct damage was caused by snow avalanches in Switzerland, despite significant expenditure on avalanche defences in the preceding 50 years [2]. In Spring 2015, persistent rain combined with snowmelt caused a debris flow in the river Morge, which significantly damaged two restaurants in St Gingolph, VS, and required evacuations and considerable clean-up efforts. In 2014, a deadly debris flow in Oso, Washington, USA destroyed a village, blocked a highway and claimed 43 lives [3], and in China hundreds of lives are lost every year [4], highlighting that these extreme events occur in developed as well as developing countries, where damage and lives lost may not be reported. Some of the most deadly debris flows are detailed by the USGS online². Due to the destruction caused by these natural disasters it is important that their physics are properly understood for better planning and protection of at-risk areas.

When a snow avalanche or a debris flow occurs, it usually encounters previously deposited or loosened material along its path. For snow avalanches this is likely to be undisturbed snow, and for debris flows this is generally loose sediment and rocks, although these phenomena are often forceful enough to dislodge larger boulders or uproot trees and sometimes even destroy installations and buildings, carrying away the rubble (Figure 1.1).

This entrained material has an important role in the flow's evolution, as its volume can increase many-fold between release and final arrest [5–7], and the run-out distance increases with flow volume [8]. Unfortunately information about its exact effect is lacking, as conclusions are often drawn from individual post-event field studies where flowing masses, velocities and so on are estimated from back-analysing flow tracks

¹http://www.slf.ch/praevention/lawinenunfaelle/lawinenunfaelle/lawinenstatistik/index_EN

²<http://landslides.usgs.gov/learn/majorls.php>



Figure 1.1: Restaurant damage at St Gingolph (20minutes/lecteur reporter 2015); Uprooted trees by debris flows in the River Uina, Grisons (B. Bates 2014); Destroyed chairlift at St Francois de Longchamp, France (C. Ancey 2012)

and deposits [9–15]. The complexity of these flows means that the cause of any one behaviour is difficult to isolate, and many avalanches at many different sites should be studied to understand their mechanics. Therefore there is a clear case for obtaining new and reliable data on entrainment in the general case.

This chapter details what is currently known about entrainment and its effects on avalanches and debris flows, based on existing field studies and experimental campaigns. To begin, a brief summary of the physics of these phenomena is presented.

1.1 Experimental observations of avalanches and debris flows

Recently, good quality, full-scale data has been obtained by instrumenting test sites which are known for avalanches or debris flows. Either avalanches are triggered such as at Vallée de la Sionne in Switzerland [16] and Rygfonn in Norway [17], or a triggered measurement system can be installed as in the Illgraben, Switzerland [18] and at Vallée de la Sionne [19], where seismic signals trigger downstream recording equipment during spontaneous events. When a site is instrumented, measurements can be obtained continuously throughout the flow, but usually at discrete geographic locations [7, 20, 21]. Radar and other scanning methods are being tested to give more continuous measurements throughout the flow but this method is currently restricted to velocity, height and temperature measurements [22, 23].

Iverson [24] presents a review of research into the structure and behaviour of debris flows, much of which was based on field observations and full-scale measurements. Debris flows are mixtures of different solid materials and fluid, usually initiated by landslides, dam collapse or heavy rainfall [25] and are self-organizing during flow under gravity [26]. As the mixture flows downstream the smaller particles drop to the bottom and larger stones and boulders are forced upwards in a process called grain-size segregation. In this way, the larger blocks flow over the smaller ones and end up at the front and sides of the flow, creating an unsaturated bouldery front and

1.1. Experimental observations of avalanches and debris flows

confining lateral levees [27]. A similar process occurs in snow avalanches [28].

After the front has passed, the middle section or body of the flow arrives. This part of the flow is saturated and contains a range of particle sizes which appear to flow as a dense, fast-moving liquid, exhibiting plastic behaviour [5, 29, 30]. A similar region exists at the base of snow avalanches, but due to their layered structure it is often obscured in observations by the saltation layer and powder cloud [17]. The tail of a debris flow is more watery and may sometimes transform into a hyperconcentrated flow [31, 32]; an avalanche tail is shallower than the body and experiences increased friction so that deposition often occurs [33]. Surges are common in debris flows and avalanches, meaning that during one event multiple flow fronts may travel down the same channel [22, 25, 34].

Due to the complex composition of avalanches and debris flows, their motion depends strongly on internal interactions between their components [35] and external interactions with their environment [36]. Two important dynamic controls on debris flow and avalanche mobility are pore pressure (pressure in the interstitial fluid) and basal shear stress. Under certain conditions, debris flows can travel much further and faster than expected [31, 37]. Iverson [37] suggests two reasons for long run-out in their large-scale experiments: bed roughness – which increases basal shear – led to flow sorting which increased run-out by creating levees that channelled the flow, and increased pore pressure due to mud content led to reduced flow resistance. McArdell et al [38] used geophone data from the Illgraben site to infer that sustained increased pore pressure during debris flows contributed to their increased mobility, but they did not find a link with basal shear. Results from the Chalk Cliffs site in Colorado [31] also found a link between high pore pressure and long run-out distances in debris flows. Large-scale experiments, such as those carried out on debris flows by Iverson and colleagues at USGS, have also been performed using snow at the Weissfluhjoch in Switzerland, to investigate their velocity profiles and rheological behaviour [39].

Due to the complications associated with studying gravity flows in nature, an effective alternative is to move to the laboratory. Here, simplified experiments can be performed in which one process is isolated and cause and effect is easier to attribute. Iverson [40] discusses the applicability of small-scale experiments to large-scale natural phenomena and concludes that bigger is better, yet the strategy of the Laboratory of Environmental Hydraulics (LHE) is to understand individual processes by simplifying systems, and this is the approach adopted in this thesis.

Most laboratory studies use idealised material in place of natural material, in order to avoid the complications of working with snow and mud. For example, Larcher et al [41] used water-saturated PVC pellets in a steady uniform flow and filmed from the side in order to see the flow structure throughout the depth. Four different flow regimes applicable to real debris flows were found, with differing amounts of stratification.

However natural geophysical gravity flows are not steady and uniform, and some authors have developed novel facilities in order to study non-uniform flows. In a rotating drum, an avalanche is stationary in the fixed frame of reference so that it can be analysed, e.g. for the effect of composition on rheological behaviour [42], its dynamic properties including velocity profiles and pore pressure [43], its structure [44], particle interactions [45] or to see bedrock erosion [46]. Other authors have used an upwards-moving conveyor belt to study a gravity flow in a stationary way [47, 48].

The evolution of a gravity-driven flow from start to finish is perhaps best studied as part of a simplified dam-break study. The classic work by Huppert [49] on a viscous gravity-driven flow propagating over a horizontal surface has given rise to many more complex studies, for example, propagation of a gravity-driven flow along a fluid interface [50], along channels of varying geometry [51], down a slope [52, 53] or over a lubricating layer [54]. The problem has been extended to viscoplastic dam breaks on slopes [55–60], and to suspensions and fluid-solid mixtures in which novel imaging techniques allow the study of the flow in the centre of the flume, in order to avoid wall effects in dam breaks of fluid-solid mixtures [61–63].

1.2 Modelling avalanches and debris flows

In many models, the complexity of mixture flows is treated by depth averaging over a flow column, as in the St. Venant approach [64]. The Savage Hutter depth-averaged model for granular motion is perhaps the key reference upon which many models are based, and it describes the motion of a mass of grains moving downslope, with considerations for particle interactions and basal friction from a Coulomb yield criterion. This model assumes that the fluid phase is passive and does not influence the flow. Over a planar base this model yields two equations for the evolution of flow height $h(x, t)$ and depth-averaged slopewise velocity $\bar{u}(x, t)$:

$$\begin{aligned}\frac{\partial h}{\partial t} + \frac{\partial}{\partial x}(h\bar{u}) &= 0, \\ \frac{\partial \bar{u}}{\partial t} + \bar{u}\frac{\partial \bar{u}}{\partial x} &= (\sin \theta - \tan \delta \operatorname{sgn}(\bar{u}) \cos \theta) - \beta \frac{\partial h}{\partial x}.\end{aligned}$$

Here, interactions with the external environment occur through the basal friction angle δ , the slope angle is denoted by θ , and β dictates the relationship between normal and shear stresses, depending on the internal friction angle. No considerations are made for vertical velocities and the velocity profile is set to uniform.

More recently, theoretical models have focused on taking into account the different phases [65], i.e. solid and fluid phases which interact through various forces including buoyancy and drag [66, 67], varying internal friction angles to allow for fluid-solid transitions [64] and vertical particle rearrangement [68].

A variety of commercial models are used by engineers to predict the dynamics of avalanches and debris flows, usually with the goal of generating risk maps and planning defences for inhabited zones and areas where new buildings or infrastructure are proposed. In general these models are based on shallow continuous flows with some rheology considerations to account for basal and internal friction. As an example, the RAMMS model was developed at the SLF in Switzerland for snow avalanches [69] but has been extended to debris flows and rock avalanches. It solves the depth-averaged equations of avalanche motion [70] with either Voellmy Salm frictional rheology [71] or a rheology based on random collisions dissipating kinetic energy [72].

Rickenmann et al [73] evaluated three debris flow models of this kind, including a finite volume model with Herschel Bulkley rheology, and found reasonable results. Some authors have added further detail, for example dilatancy and pore fluid pressure [74]. Many other models exist in the literature, all with differing physical assumptions, usually concerning the material rheology.

1.3 The problem of entrainment

Observations in the field have revealed a variety of different entrainment mechanisms in snow avalanches and debris flows. In snow avalanches, four mechanisms were suggested: particle impact, abrasion, ploughing and fluidization by excess pore air pressure [75]. Sovilla et al [7] presented radar measurements showing step entrainment when soft snow, initially protected by a strong layer, is entrained instantaneously. In debris flows progressive entrainment of sediments was observed in all sections of the flow [76] and was faster when sediment was saturated, indicating a shear-induced pore-pressure control on entrainment [77].

Not all available models take into account mass entrainment, and those that do often use crude methods. For example RAMMS [69] assumes snowpack fragmentation when the avalanche arrives, and an entrainment rate proportional to the snow density and flow velocity. Other models require an entrainment rate selected by the user or calibrated constants [78, 79]. However it has been shown that models taking entrainment into account – even using a simple model – do significantly better at predicting run-out, flow velocities and flow heights [7, 80].

In depth-averaged models for avalanches and debris flows, the question of entrainment is problematic as it occurs only at the base. Often these models include a local exchange rate $E(x, t)$ which defines how much loose material is entrained or how much of the flow is deposited [79, 81], but the definition of this rate varies throughout the literature [82, 83] and is usually fitted to experimental results e.g. from granular heap

experiments [84]. These equations usually take a form similar to:

$$\begin{aligned}\frac{\partial h}{\partial t} + \frac{\partial h\bar{u}}{\partial x} &= E, \\ \frac{\partial h\bar{u}}{\partial t} + \frac{\partial h\bar{u}^2}{\partial x} &= gh \sin \theta - gh \cos \theta \frac{\partial z_b}{\partial x} - \bar{u}E - \frac{\tau_b}{\rho}, \\ \frac{\partial z_b}{\partial t} &= -E,\end{aligned}\tag{1.1}$$

where $z_b(x, z, t) - z = 0$ defines the exchange surface, and τ_b is a basal shear stress term, which is defined depending on the rheology of the material.

The local nature of this exchange rate means that it describes the vertical enlargement of one column of flow at position x and time t . Iverson & Ouyang [83] present a review of many existing depth-averaged models which consider entrainment effects, highlighting the different formulae for E , and note that many of them violate essential conservation laws when exchange occurs between flow and substrate. In order to rectify these violations, a number of jump conditions are proposed which must hold on the surface $z_b(x, z, t)$.

Other models simplify the flowing mass using a model with a yield stress [85, 86] and comparing the avalanche's basal shear stress with the entrainable bed's yield stress [87, 88]. Issler [89] presents a detailed derivation of an abrasion-type entrainment rate, however the analysis is based on a moving column of material, and not a full avalanche. Further theoretical mechanisms are a mixing layer between flow and substrate based on kinetic theory [90], increased pore pressure at the entrainment interface [91], and fluidized zones in the bed [92, 93]. Although somewhat differing, many of these analytical works have one thing in common: they bemoan the lack of high quality data from idealised laboratory studies (e.g. [89]).

Most existing laboratory studies have focused on entrainment by dry granular avalanches. For example, slope angle was seen to be a controlling factor in the effects of entrainable material [94], with a critical angle of 12° identified, below which entrainment decreased run-out and above which it increased run-out by up to 40%. Further controls on bed excavation were identified above this angle [95] in particular entrainable bed depth, flow volume and flow velocity. Barbolini et al [96] found that ploughing and abrasion were the two most significant mechanisms in entrainment, whereas Roche et al [97] found evidence for block entrainment by increased pore pressure gradients. The photoelastic techniques used by Estep & Dufek [98] showed that force chains may propagate far ahead of the flow front into the entrainable bed, potentially dislodging the substrate, yet in cases with rough substrate these force chains may stabilise the bed and halt the avalanche [99]. Very little work has been done on saturated granular flows, finding for example that bed sediment size affected the entrainment rate [100].

These experimental studies are limited, due to their only being observable from the exterior, and as such the results may have been influenced by the flume walls. For instance, examining an entraining avalanche after arrest [101] it was found that features on the entrainment interface at the centre were not seen at the edge. This therefore calls for a study that takes continuous internal measurements during entrainment, so that the fluid mechanics far from the side walls may be studied.

1.4 Contribution

This work is an experimental and theoretical study of entrainment by idealised dam-breaks. Experimental techniques are used to provide new, high-quality data on entrainment by geophysical gravity-driven flows, by reducing the problem to the simplest Newtonian and viscoplastic cases. The experimental data is then exploited for the development of new theoretical lubrication models – in which entrainment is modelled as non-local transport – which successfully reproduce observations.

This thesis makes an novel contribution due to the following two reasons.

- As far as I am aware, the experiments performed represent the first study in which entrainment is studied continuously within the flowing avalanche, by adapting the experimental system of Andreini et al [62] for non-intrusive measurements of gravity flows.
- The lubrication models developed model the transport of entrained material in a non-local way, assuming that the dam-break and all entrainable material – even material far downstream which may never be disturbed – flow as a continuum. This removes the need to define local exchange terms, which have been a sticking point for many previous models.

Figure 1.2 is a map showing the three experimental campaigns of increasing complexity and the questions asked at each stage.

Measurements of bulk and internal dynamics are taken in order to respond to the following two questions:

- How does an avalanche interact with entrainable material lying in its path?
- What happens to the avalanche as a result of entraining material during flow?

This thesis presents two principle experimental studies: a dam-break of Newtonian fluid which flows down a horizontal channel containing an entrainable layer, and a gravity-driven flow of viscoplastic fluid entraining material in an inclined channel. In

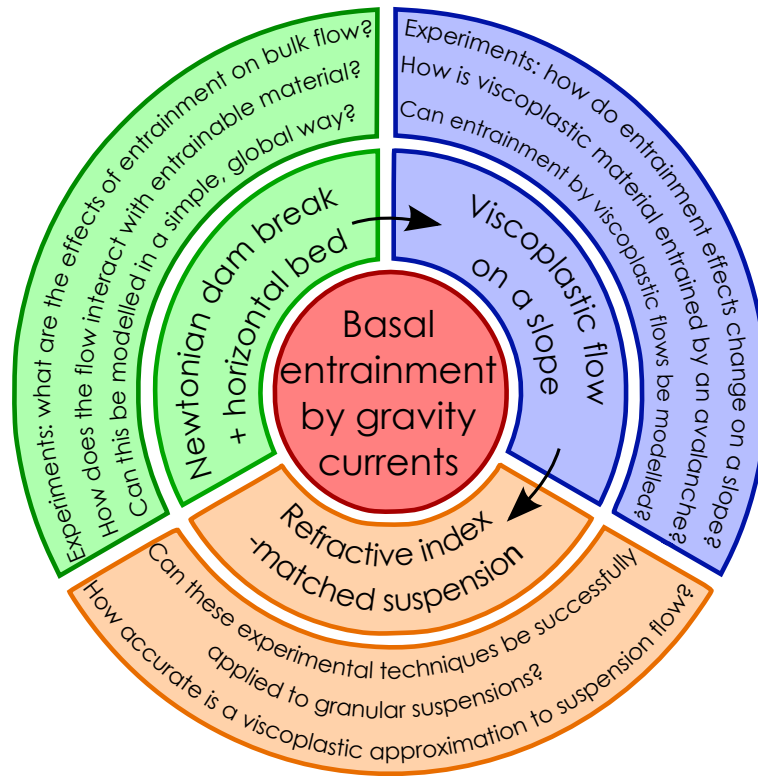


Figure 1.2: A guide to reading this thesis.

the simpler case of an entraining Newtonian dam break, a classical analytical thin-film model [49] was adapted for this new case including entrainment. The model was solved numerically, with results showing a good agreement with all of the experimental data.

The success of the lubrication model in the Newtonian case led to the idea of adapting a model for viscoplastic dam breaks to the problem at hand. Although this kind of model has been shown to have its drawbacks (e.g. [53]), it perfectly predicts the effect of the entrainable material on the position of the flow front, whilst qualitatively reproducing the surface height of the flow.

A detailed study of entraining dam-breaks of granular suspensions is shown as practically feasible, pending several improvements, and is left as a suggestion for future work.

Experimental Facility and Techniques

This chapter presents the experiments performed to investigate entrainment: first the equipment is described, and then the three experimental campaigns are presented in detail. The three studies increase in complexity: the first is a Newtonian dam-break flowing down a horizontal flume, then similar methods are applied to a viscoplastic fluid on a slope, and finally a granular suspension is studied.

2.1 Equipment

Flume

A 3.5 m long by 10 cm wide inclinable flume [62] was modified for this work. The flume was constructed to study internal velocities in gravity-driven flows, and as such was made with a polymethyl methacrylate (PMMA) base and a 50 cm long viewing window on each side. The observation area was fixed, so for this thesis a mobile pneumatic lock-gate was added in order to release the material at the appropriate distance. Two shallow sheets of PMMA were placed along the flume, making a false bottom. A gap was left between the two pieces and filled with entrainable material, so that the dam-break initially flowed over a rigid base, then over a finite layer of loose material – the entrainable bed – before continuing over a rigid base (figure 2.1).

Laser and PIV set-up

A 2 W Diode-Pumped Solid State Nd:YAG laser with wavelength 532 nm was used with the optical set-up shown in figure 2.2 to create a vertical laser sheet down the centre of the flume in the observation zone, so that particle image velocimetry (PIV) could be performed. PIV is a flow visualisation technique in which a seeded flow is filmed at high speed so that the instantaneous velocities can be found by comparing the distribution of seeds in two consecutive images. The seeds used in this study were

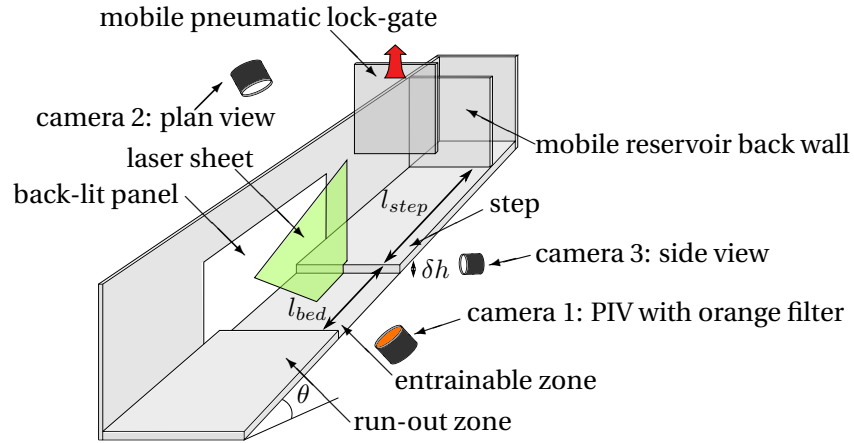


Figure 2.1: Experimental set-up including reservoir, lock-gate, step and entrainable bed layer, and the location of the laser sheet. The flow is in motion at slope angle θ and the bed dimensions are l_{bed} long by δh deep.

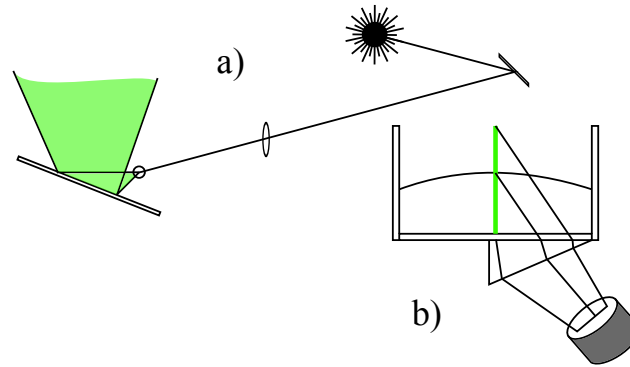


Figure 2.2: a) Optical set up with laser, mirrors, lens and rod for creation of vertical laser sheet; b) prism to film interior of flow from below.

20 μm PMMA beads tagged with rhodamine 6G, a stain which is fluorescent in green light. In this way only the particles in the central laser sheet were illuminated and only they were filmed.

The suspension experiments (described in section 2.4) required a slightly different technique and a stronger laser. Instead of seeding the suspension – small particles may act as lubricating fines or cause unwanted effects such as grain size segregation – rhodamine 6G was mixed directly into the suspending fluid so that it fluoresced and the grains did not, and PIV was possible in this way. Contrary to the fluids, the transmission of light through the suspension was not perfect, and so a better focus was required for sufficient image quality. With a smaller aperture the focus was improved, however images were much darker, and so a 4 W laser was chosen for these experiments.

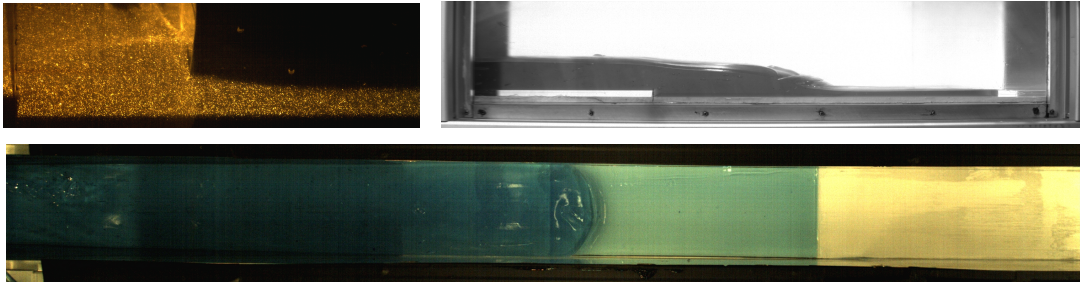


Figure 2.3: Images from Cameras 1 and 3 (top) and camera 2 (bottom) during viscoplastic experimental campaign.

Cameras and image acquisition

Three different high-speed cameras were used in the experiments. Camera 1 filmed the illuminated internal section of the flow through an orange filter: the light emitted by rhodamine has a longer wavelength than that absorbed and the orange filter blocks the green light of the laser but allows the transmission of the emitted light. This camera was placed below the flume and filmed through the transparent base and a prism, using a tilted lens for the Scheimpflug principle [102] in order to obtain clear images from a focal plane which is non-parallel to the image plane. Usually PIV is performed by filming from the side, but the flow front in many of these experiments was significantly curved in the cross-stream direction, and so images were acquired through the base to avoid distortion at the flow front. Camera 1 was a Basler A403k camera, and was calibrated for each experiment using a grid immersed in fluid in the flume. PIV measurements were taken in a 6.5 cm long central streamwise section in the entrainment zone.

Camera 2 (also a Basler A403k) filmed from above to show the progression of the flow front, through a red filter if the laser was on. Camera 3 was used to film through the observation panel in the side of the flume in order to obtain the flow and bed surface elevation during entrainment. This was a Basler acA2000-165um USB 3.0 camera and an LED panel provided backlighting. Figure 2.3 shows some examples of raw images taken during the viscoplastic experimental campaign.

PIV software

To obtain measurements from camera 1's images, the velocity field was calculated using PIV between two images an appropriate time-step apart. This was then filtered with a signal to noise ratio (SNR) of 1.3 and a local filter of 2.7, then all removed vectors were interpolated linearly. All measurements were corrected for perspective using a calibration grid. The PIV software used was the opensource package MatPIV [103]. Error quantification in PIV remains difficult, but it is known that strong velocity

gradients reduce measurement accuracy [104], so steps were taken to minimise errors, such as choosing the optimum seeding density and correlation window size.

2.2 Experimental campaign 1: Newtonian fluid

A natural starting point for fluid dynamics investigations is to perform a simplified exploratory experimental campaign. Keeping in mind the goal of simulating and understanding entrainment by avalanches on slopes, initial experiments were carried out using a Newtonian fluid in the flume set to 0° inclination. This allowed the development of techniques and was of interest in itself, as a previously unsolved problem about what happens when a moving layer of viscous fluid flows over a layer of stationary fluid.

The fluid used was glycerol (supplied by Alfa Aesar GmbH, Germany) diluted to a 98.5% volume concentration aqueous solution. This was done because glycerol has a high affinity for water, and is unstable at high concentrations, absorbing water vapour quickly from its surroundings. At this concentration, its density is $1257.5 \text{ kg m}^{-3} \pm 0.5 \text{ kg m}^{-3}$. As glycerol has a highly variable viscosity with temperature and concentration, its viscosity was closely monitored and experiments were performed as close to 20°C as possible.

Two main experimental campaigns were undertaken. In one, the fluid was dyed with Methylene blue and filmed from above over the entire flow length, and through the 50 cm long transparent side-panels, in order to obtain information about the bulk flow characteristics, namely the front position with time and the surface height profile during entrainment. In the other campaign, the flow was seeded and filmed for PIV at the entry to the entrainment zone, in order to study the internal dynamics of interaction between the dam-break and the bed. A summary of the experiments performed is presented in table 2.1.

In most cases the length of the reservoir (behind the lock-gate) was kept constant at 30 cm; only in the two experiments in which 1500 ml fluid was released was the reservoir the shorter length of 20 cm. The length l_{step} is the distance from the reservoir back wall to the step and so includes the length of the reservoir. Based on calculations by Didden & Maxworthy [105] l_{step} was chosen so that it was always $\gg (\rho^2 g V_0^5 / \mu^2)^{1/7}$, where ρ is the fluid density, μ its kinematic viscosity, and V_0 is the volume per unit width. This guarantees a dominant balance between gravity and viscous forces, with inertia playing a less significant role. The length of the entrainable bed l_{bed} was varied between 10 and 50 cm, and its depth was either 3, 6 or 9 mm, to be compared with the no-entrainment case.

For the bulk experiments, cameras 2 and 3 had frame rate: 20 frames per second,

2.3. Experimental campaign 2: Viscoplastic fluid

Table 2.1: Experiments performed using glycerol

Run	Vol, ml	l_{step} , cm	δh , mm	l_{bed} , cm	l_{res} , cm	μ , Pa s	temp, °C
Bulk A	800	-	0	-	30	1.041	20.10
Bulk B	800	50	3	50	30	0.916	19.95
Bulk C	800	50	6	50	30	1.038	20.30
Bulk D	800	50	9	50	30	0.902	20.05
Bulk E	800	50	6	30	30	1.007	-
Bulk F	800	50	6	10	30	1.009	20.05
Bulk G	800	60	6	30	30	1.011	20.10
Bulk H	800	70	6	30	30	0.984	20.00
Bulk I	1500	-	0	-	20	0.843	19.50
Bulk J	1500	60	6	50	20	0.835	19.50
PIV A	800	50	3	50	30	1.121 ± 0.062	19.5
PIV B	800	50	6	50	30	1.121 ± 0.062	19.5

except for runs I & J where the frame rate was 33.3 frames per second. For the internal experiments, camera 1 had parameters: exposure time 3000 μ s, frame period 7500 μ s, acquisition time 12 s and image size 600×2352 pixels.

In the bulk tests both the bed and the reservoir fluid were dyed blue, but for the internal measurements two configurations were used for visualizing the flow (see figure 4.5). In a “reservoir run” denoted by the letter R, the fluid released from the reservoir was seeded and the bed fluid was largely without seeds. The idea here was to show a clear and measurable interface between the substrate and the avalanche. A “combined run” denoted by a C, refers to experiments where all fluid was seeded, thus providing detailed velocity measurements in all of the system, but the interface is not shown. A similar set of configurations was also used for the viscoplastic experiments.

2.3 Experimental campaign 2: Viscoplastic fluid

In order to study entraining flows on a slope, it was necessary to choose a material which could act as both a stationary bed layer – mimicking undisturbed mud or snow – and a flowing avalanche. An aqueous solution of Carbopol Ultrez 10 (manufactured by Lubrizol), a viscoplastic “micro-gel” is an appropriate choice, as it exhibits a yield stress, remaining plastic on a slope until sufficient shear is applied (i.e. by the overriding avalanche), causing it to yield and flow. This is because it contains polymer chains which, when sheared, are forced to untangle and unwind. It differs from other polymers as the chains are highly-branched, making them sponge-like [106], thus allowing high viscosities at low concentrations and shear thinning without the stringiness of an extensional flow [107].

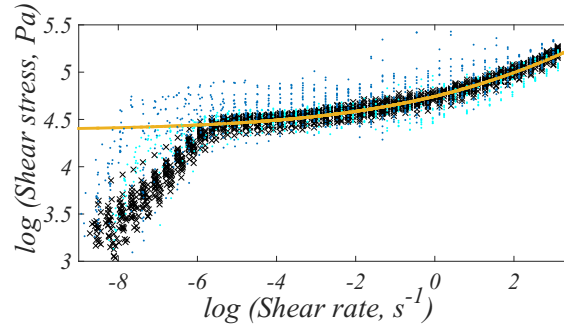


Figure 2.4: Shear stress versus rate of strain graph for clear and blue-dyed Carbopol Ultrez 10 at 0.3% concentration.

Carbopol has been shown to be well modelled by the Herschel Bulkley constitutive law, which makes it an appropriate substitute for snow or mud [108]. The Herschel Bulkley model describes a yield stress, below which no flow occurs and above which a change in viscosity occurs. The relationship between shear stress and strain rate is $\tau = \tau_c + K\dot{\gamma}^n$ where τ_c is the critical shear stress, K is a property called the consistency and n the power law index [30, 107]. When $n < 1$ the material is shear-thinning above the yield stress. Its surface tension has been measured and found to be around 10% less than that of water [109].

Carbopol is transparent and easily seeded with fluorescent tracking micro-particles, without significantly changing the material rheology. Nanoparticles are known to affect the rheology of Carbopol polymer solutions by interfering with the polymer chains, however small concentrations of microparticles such as used here have no effect [110]. Nonetheless it was necessary to check that no significant rheological effects were caused by these tracers, for example by altering the pH of the mixture, as this is known to significantly change the rheological properties of Carbopol gels. Rotational rheometry showed no significant difference between seeded and unseeded Carbopol for any of the rheological tests performed.

Further advantages of Carbopol Ultrez 10 are its low toxicity, the facility of preparation and the easy control of rheological parameters by varying the concentration. It is also non-thixotropic. The Carbopol was prepared as follows: the powder was first added to the required amount of deionized water at 60°C, and left until it sank to the bottom, over a few hours or one night. Then it was stirred for around two hours and left to settle for a further few hours. Finally an aqueous solution of NaOH was prepared and mixed with the Carbopol-water solution, for neutralisation. It is during this final step that the mixture takes on its viscoplastic gel-like appearance. Once prepared, the bubbles must be removed, which is easily achieved by stirring at a constant, low speed for around one hour.

Based on results from Cochard & Ancey [60] and some preliminary tests, the Carbopol

2.3. Experimental campaign 2: Viscoplastic fluid

Table 2.2: Viscoplastic experiments performed: dyed with Methylene Blue

run name	$\theta, ^\circ$	$\delta h, \text{ mm}$	config	$M, \text{ kg}$	$l_{step}, \text{ cm}$	$l_{bed}, \text{ cm}$	temp, $^\circ\text{C}$
12-0a	12	-	-	3	70	-	19.20
12-6Ra	12	6	r	3	70	30	19.20
12-6Ca	12	6	c	3	70	30	19.30
16-0c	16	0	-	3	70	-	19.50
16-3Rd	16	3	r	3	70	30	19.90
16-3Cc	16	3	c	3	70	30	19.85
16-3Re	16	3	r	3	80	20	19.90
16-3Cd	16	3	c	3	80	20	19.90
16-6Rc	16	6	r	3	70	30	19.70
16-6Cc	16	6	c	3	70	30	19.50
16-9Ra	16	9	r	3	70	30	20.00
16-9Ca	16	9	c	3	70	30	20.00
16-6Rd	16	6	r	3	90	30	19.90
16-6Cd	16	6	c	3	90	30	19.65
16-6Cf	16	6	c	3	90	20	19.90
16-6Cg	16	6	c	3	90	15	19.50
16-0e	16	0	-	3	90	-	19.60
20-0a	20	0	-	3	90	-	19.45
20-6Ra	20	6	r	3	90	30	19.95
20-6Ca	20	6	c	3	90	30	20.10
20-6Rb	20	6	r	3	90	20	20.00
20-6Cb	20	6	c	3	90	20	19.80
20-6Rc	20	6	r	3	90	10	19.50
20-6Cc	20	6	c	3	90	10	19.65
20-6Cd	20	6	c	3	110	10	19.65
20-6Rd	20	6	r	3	110	10	19.90
20-6Ce	20	6	c	3	100	20	19.95
20-6Re	20	6	r	3	100	20	19.60
20-3Ra	20	3	r	3	90	30	19.55
20-3Ca	20	3	c	3	90	30	19.95
24-0a	24	-	-	3	90	-	19.45
24-3Ra	24	3	r	3	90	30	19.50
24-3Ca	24	3	c	3	90	30	19.40
24-6Ra	24	6	r	3	90	30	19.20
24-6Ca	24	6	c	3	90	30	19.20

solution chosen was 0.3% concentration by weight, and its rheological properties were determined using a Bohlin Gemini rotational rheometer, supplied and maintained by Instrumat SA, distributors of Malvern Instruments Ltd. Tests were performed in which the shear stress was measured in response to an increasing applied strain, and also in which the elastic response to very gentle rotation was measured. Striated parallel plates were chosen to reduce slip due to wall depletion effects [111], with diameters of

Chapter 2. Experimental Facility and Techniques

40 and 25 mm, and the gap size was either 1 mm or 0.5 mm. Cone-plate geometries were also tested due to the independence of the measurement on the radius, however the results were far less conclusive.

Two sets of experiments were carried out. In one set the fluid was stained with Methylene Blue so that accurate front tracking could be performed by camera 2 down the length of the flume, and so that surface heights could be measured by camera 3. The slope was varied between 12 and 24°, the mass released was kept constant, the bed location was varied in some cases and the bed length and depth was varied at some slopes. Table 2.2 shows the experiments performed in this set-up. A Herschel Bulkley model was fitted to the rheometry measurements and the fluid was found to have rheological parameters $K = 35 \text{ Pa s}^n$, $n = 0.33$, $\tau_c = 78 \text{ Pa}$ as shown in figure 2.4 (black crosses). Adding Methylene Blue appeared to change the accuracy of the fitted law, but not the parameters (blue dots). To the eye there was no obvious change.

In the other set of experiments PIV measurements were taken to identify any internal changes due to entrainment. A reduced set of experiments was performed, shown in table 2.3. This batch of Carbopol was found to have rheological parameters $K = 35 \text{ Pa s}^n$, $n = 0.33$, $\tau_c = 58 \text{ Pa}$. The fluid had been prepared and stored for two months prior to use, and perhaps this caused the yield stress to fall, however this is not a problem if it is properly taken into account when the results are interpreted.

These rheological parameters, and the characteristic length-scales of the experiments performed mean that the Bingham number, defined as $B = \tau_c / (\rho g H \sin \theta)$ [53] where H is the characteristic height scale, is never greater than 1. In this regime, the slope effects are dominant over yield stress effects [112] and so the shear layer at the base of the flow is significant, in comparison with yield stress dominated flows in which the pseudo-plug extends almost to the base.

The mass released, the concentration of the Carbopol, and the slopes were all chosen so that the flow released from the dam-break was fast enough, but the layer of fluid in the entrainable bed stayed still. The bed location was then chosen so that a viscoplastic version of Didden & Maxworthy's force balance applied: to guarantee viscous forces were greater than inertial forces, $\tau L W \sim K L W U^n / H^n \gg \rho V_0 L W / T^2$, where L, H, U, W are scalings for length, height and velocities respectively, $T = L / U$ and $V_0 = L \times H$. Then balancing buoyancy with viscous forces, $U^n = \rho g \sin \theta H^{n+1} / K$, so that $L \gg (\rho V_0 (g \sin \theta)^{1-n/2} / K)^{2/(3n+2)}$. For this reason the bed begins at least 70 cm downstream for slopes 12° and 16°, but at least 90 cm downstream for slopes 20° and 24°.

In these experiments, care was taken to remove bubbles from the fluid and to perform the experiments as close to 20°C as possible. Further, precautions were taken to minimise slip on the PMMA base – an ionic reaction causes increased wall depletion, which leads to excess lubrication on the base – covering the flume with Carbopol and

2.4. Experimental campaign 3: Granular Suspension

Table 2.3: Viscoplastic experiments performed: seeded for PIV

run name	$\theta, ^\circ$	$\delta h, \text{ mm}$	config	$M, \text{ kg}$	$l_{step}, \text{ cm}$	$l_{bed}, \text{ cm}$	temp, $^\circ\text{C}$
12-0a	12	0	-	3	70	-	20.00
12-6Ra	12	6	r	3	70	30	20.35
12-6Ca	12	6	c	3	70	30	20.25
16-0a	16	0	-	3	70	-	20.00
16-0b	16	0	-	3	90	-	19.80
16-6Ra	16	6	r	3	70	30	19.90
16-6Ca	16	6	c	3	70	30	19.65
16-6Cb	16	6	c	3	90	30	19.70
20-0a	20	0	-	3	90	-	19.70
20-6Ra	20	6	r	3	90	30	20.15
20-6Ca	20	6	c	3	90	30	20.00
24-0a	24	0	-	3	90	-	19.60
24-6Ra	24	6	r	3	90	30	19.60
24-6Ca	24	6	c	3	90	30	19.75

letting it dry was found to significantly reduce this effect [62].

2.4 Experimental campaign 3: Granular Suspension

The most complex experiments performed in this thesis used a refractive-index-matched suspension, in this way building on the experimental work described in e.g. Ancey et al [63], and bringing the experiments more in line with natural multi-phase flows.

The suspension released from the reservoir behind the lock-gate contained 57% concentration by volume PMMA beads, from Altuglas International (France), which had been sieved in a Retsch sieving stack with 200 and 180 μm sieves in order to filter out the smallest particles (figure 2.5). This was intended to reduce any unwanted effects arising from particle size differences such as lubrication by small particles and particle size segregation. A sample of 2900 filtered beads were analysed using a series of image processing operations in Matlab and they were found to be roughly normally distributed with mean diameter just less than 200 μm . A secondary peak is shown near zero. This is partly anomalous due to the image processing program detecting some badly resolved larger beads as several small beads, and to dirt being detected as beads. However there are a number of small beads which were not removed, as static charges prevented them from passing through the sieves.

Once filtered, the beads were suspended in a fluid mixture of Triton X-100, a detergent with density 1065 kg m^{-3} , supplied by Chimie Brunschwig, and UCON 75-H-4500, a

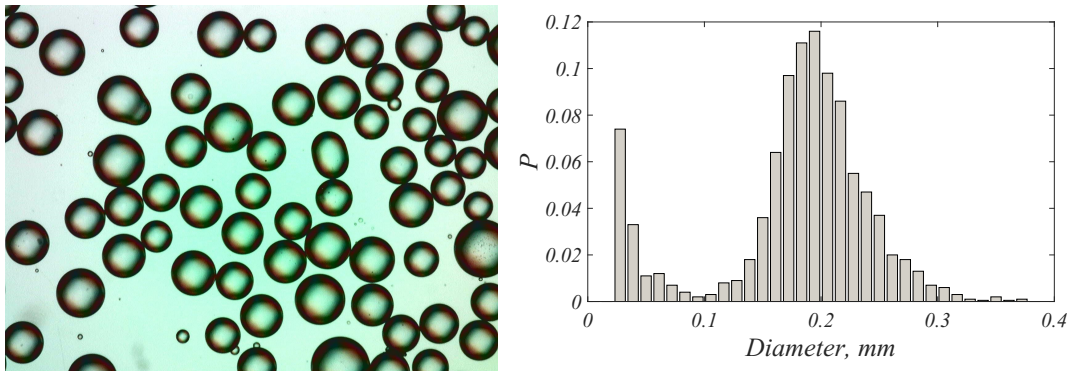


Figure 2.5: Sample image of PMMA beads after sieving, and their grain size distribution.

lubricant with density 1095.2 kg m^{-3} supplied by Dow Chemicals. The UCON was mixed with the Triton until the mixture refractive index was between 1.48850 and 1.48900 at 20°C . A total fluid mixture volume of 7.644 l was produced, with density 1068 kg m^{-3} , thus for a concentrated suspension of 57% particle volume 10.133 l or 11.997 kg of PMMA beads were required, at a density of 1184 kg m^{-3} . Other authors have made use of density matching in suspensions [62, 63], however due to the small phase density difference (less than 10%) and the short duration of the experiments (less than 5 minutes) compared to the timescale of sedimentation, I decided that this extra step was not necessary. Finally a small amount of rhodamine 6G was added to the suspension so that when illuminated by the laser, the fluid would fluoresce and the beads would show on the images as dark spots. This mixture was stirred continuously under a vacuum of at least 900 mBar below atmospheric pressure so that any trapped bubbles disappeared. Figure 2.6 shows the difference between the beads suspended in a refractive index-matched mixture and beads in water with rhodamine.

The experiment was conducted on a slope of angle either 12° or 16° . These slopes were chosen due to the flow properties of the suspension: the slope must be steep enough that the avalanche flows sufficiently fast yet shallow enough that the suspension lying in the entrainable zone does not flow away. This was also the reason for the choice of suspension concentration: lower concentrations were too liquid and separated too quickly and higher concentrations were too dense and didn't flow quickly enough. At each slope six dam-breaks were released. Three entrained a bed 3 mm deep and three entrained a bed 6 mm deep. The laser was turned on before the lock-gate was opened, leading to some degradation of the rhodamine in the bed layer. This unexpected side-effect meant that the bed material could be easily distinguished from the overriding avalanche during entrainment. For each experiment, the refractive index and temperature were checked, and the mass released was carefully measured to be either 3.25 kg or 3.8 kg. Table 2.4 details the different experiments performed.

The flume was also equipped with differential pressure sensors at four locations below

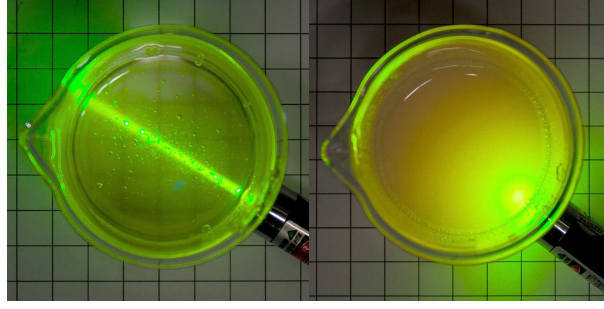


Figure 2.6: Refractive index-matched suspension versus an aqueous suspension: transmission of a laser beam.

Table 2.4: Suspension experiments performed.

run name	$\theta, ^\circ$	$\delta h, \text{ mm}$	$M, \text{ kg}$	$l_{\text{step}}, \text{ cm}$	$l_{\text{bed}}, \text{ cm}$	RI	temp, $^\circ\text{C}$
12-3a	12	3	3.25	60	30	1.4884	20.80
12-3b	12	3	3.25	60	30	1.48831	20.90
12-6a	12	6	3.25	60	30	1.48825	21.00
12-6b	12	6	3.8	60	30	1.48828	20.65
12-6c	12	6	3.8	60	30	1.4882	20.70
16-3a	16	3	3.25	60	30	1.48825	20.65
16-3b	16	3	3.8	60	30	1.48821	20.65
16-3c	16	3	3.8	60	30	1.48813	20.40
16-6a	16	6	3.8	60	30	1.48815	20.50
16-6b	16	6	3.8	60	30	1.48815	20.60
16-6c	16	6	3.8	60	30	1.48817	20.50

the entrainable material. Their purpose was to see what happened to the basal pressure signal during entrainment and whether it increased corresponding to when the surface height increased. These Honeywell sensors were connected to a National Instruments acquisition card, which was also connected to the cameras, so that the images obtained could be compared with the pressure signals to see where the front was in relation to each pressure sensor.

2.5 Error quantification

Inherent to any experimental study are measurement errors, for example it has already been noted that quantification of errors in PIV is difficult, and therefore error bounds on (u, w) are not possible to define. The other errors originating from measurements are discussed here.

- *Volume/mass of fluid/suspension.* In all cases this was measured as a mass, by weighing the container before and after the fluid had been extracted to be put

in the flume reservoir. For Newtonian and viscoplastic studies this was accurate to within 10 g. For the suspension this was within 20 g. For the Newtonian and suspension experiments, some fluid was lost down the sides of the inserted steps. The maximum estimate for lost fluid is 1.5 ml based on the size of the two thin gaps either side, which is maximum 0.18% of the 800 ml Newtonian fluid released and maximum 0.1% of the fluid phase in the suspension experiments with mass $M = 3.25$ kg.

- The *set-up lengths* were measured with a tape measure or ruler with 1 mm markers, and therefore are accurate to within around 0.25 mm.
- *Viscosity of glycerol*. This was a tricky parameter to measure – an Ostwald viscometer was used to measure viscosity for the bulk experiments, yet the results were variable. Thus many measurements were taken for each sample and the error was around 1%. The PIV experiments were performed earlier and the viscosity was calculated by measuring the glycerol concentration by its specific gravity (using a hydrometer) and reading its viscosity from a table.
- *Rheology of Carbopol*. It has been noted [47, 53] that Carbopol preparations are very sensitive to concentration and they may change their properties over a short period of time. For this reason there is some margin of error around each of τ_c , n and K . Analysing the spread of the rheometric measurements gives an error for K of around 5%, similar for n , and around 3% for τ_c .
- *Measurements from cameras 2 and 3*. Using the calibration grids, camera 2's resolution was roughly 2 pixels per mm and camera 3's resolution was around 3 pixels per mm. Thus measurements from these two cameras (surface height and flow front position) can be estimated to be accurate to within 0.5 mm, taking into account effects such as shadows in camera 2 and surface curvature in camera 3.

At each step in this investigation, a model is sought to try to reproduce the experimental results. As such, a summary of the details of lubrication models is presented for Newtonian and viscoplastic gravity-driven flows, and a review of what is known about granular suspensions is presented.

The starting point for the derivation of these flow models is to take the Cauchy equations for conservation of mass and momentum, together with the constitutive equation for the extra stress tensor. This describes the relationship between stresses and the strain rate which is dictated by the rheological properties of the material under investigation. Then the equations are simplified based on the flow regime – i.e. whether inertia, gravity, pressure gradient or viscous forces have the dominant effects on the flow – and the flow geometry, for example whether one spatial dimension is much larger than the others.

In two dimensions the full equations are

$$\begin{aligned}
 u_x + w_z &= 0 \\
 \rho \frac{Du}{Dt} &= \rho g \sin \theta - \frac{\partial p}{\partial x} + \frac{\partial \sigma_{xx}}{\partial x} + \frac{\partial \sigma_{xz}}{\partial z} \\
 \rho \frac{Dw}{Dt} &= -\rho g \cos \theta - \frac{\partial p}{\partial z} + \frac{\partial \sigma_{xz}}{\partial x} + \frac{\partial \sigma_{zz}}{\partial z},
 \end{aligned} \tag{3.1}$$

where (u, v) are the velocities in the slope-wise and slope-normal directions (x, z) , D/Dt is the convective derivative, ρ the density, θ the slope angle, p the pressure and Σ or σ_{ij} is the Cauchy stress tensor. A summary of the notation used is presented in the Glossary at the end of this thesis.

The flow is assumed to be two-dimensional in the slope-wise and the slope-normal directions, neglecting cross-stream effects, although it has been noted that channeled viscoplastic flows had reduced basal shear stress [109]. This is something to bear in

mind in what follows.

Boundary conditions are usually given by the no-slip condition at the rigid base $u = w = 0$ for $z = 0$, and the stress-balance condition at the flow surface with normal $\mathbf{n} = (h_x, -1)$ and tangent $\mathbf{t} = (1, h_x)$, as well as the kinematic boundary condition that a particle on the surface remains on the surface, so that (neglecting atmospheric pressure and surface tension) on $z = h$

$$\begin{aligned} \mathbf{n} \cdot \Sigma \cdot \mathbf{t} &= 0 & \Rightarrow & \sigma_{xz} + \sigma_{xx}h_x = 0 \\ \mathbf{n} \cdot \Sigma \cdot \mathbf{n} &= 0 & \Rightarrow & \sigma_{zz} - \sigma_{xz}h_x = 0, \\ h_t + uh_x &= w. \end{aligned} \tag{3.2}$$

In the above experiments, the flume length was chosen so that viscous forces were dominant over inertial forces in the arguments presented by Didden & Maxworthy [105], so that the role of inertia is minimised. In this way the characteristic length of the flow is much greater than its height and a lubrication model provides the simplification required [58, 113].

The chief assumptions of the lubrication approximation are that the characteristic flow height H is much smaller than the characteristic flow length L and by mass conservation the downstream velocity is much greater than the slope-normal velocity. In this case, and with negligible inertia the model simplifies to:

$$\begin{aligned} u_x + w_z &= 0 \\ 0 &= \rho g \sin \theta - \frac{\partial p}{\partial x} + \frac{\partial \sigma_{xz}}{\partial z} \\ 0 &= -\rho g \cos \theta - \frac{\partial p}{\partial z}. \end{aligned} \tag{3.3}$$

In what follows these equations are adapted to a Newtonian flow and then a flow described by the Herschel Bulkley rheology.

3.1 Newtonian dam breaks

Huppert [49] treats the case of a non-entraining two-dimensional viscous gravity-driven flow, in which a dam-break is modelled under the assumptions of lubrication theory. Beginning with equations (3.3) at $\theta = 0^\circ$, and supposing that the density and pressure of the ambient fluid is small, it is found that

$$p = -\rho g(z - h(x, t)) \tag{3.4}$$

where $h(x, t)$ is the surface elevation. In this way, and with $\sigma_{xz} \approx \mu \partial u / \partial z$,

$$\frac{\partial^2 u}{\partial z^2} = \frac{g}{\nu} \frac{\partial h}{\partial x}. \quad (3.5)$$

Then with the no-stress condition at the flow surface and the no-slip condition at $z = 0$,

$$u(x, z, t) = -\frac{g}{2\nu} \frac{\partial h}{\partial x} z(2h - z). \quad (3.6)$$

At this point, the depth-integrated continuity equation is used to give an equation for the flow height $h(x, t)$

$$\frac{\partial h}{\partial t} - \frac{g'}{3\nu} \frac{\partial}{\partial x} \left(h^3 \frac{\partial h}{\partial x} \right) = 0, \quad (3.7)$$

where g' is the reduced gravity and is equal to g , the acceleration due to gravity, when the density of the ambient fluid is small, and ν is the fluid's kinematic viscosity. Volume is conserved between the front $x_H(t)$ and the origin at $x = 0$

$$\int_0^{x_H(t)} h(x, t) dx = V_0, \quad (3.8)$$

which yields an analytical solution for the surface height of a dam-break of a constant volume per unit width V_0 , by searching for a similarity solution to (3.7) with the variable $\eta = (3\nu/g'V_0^3)^{1/5} x t^{-1/5}$. The front position, $x_H(t)$ is found by solving $h(x_H, t) = 0$ to be

$$x_H(t) = \eta_H \left(\frac{gV_0^3}{3\nu} \right)^{1/5} t^{1/5}, \quad (3.9)$$

where $\eta_H = 1.411 \dots$ is the value of the similarity variable η at the flow front $x = x_H$.

3.2 Viscoplastic gravity-driven flows

Various constitutive equations can be used to characterise non-Newtonian materials by describing the shear stress response to a varying strain rate and subsequently obtaining the viscosity; this is their rheology. For example in Newtonian fluids the shear stress increases linearly with strain rate, therefore they have a constant viscosity. The simplest model to incorporate a yield stress is the Bingham rheology [114]: a yield stress must be exceeded in order for flow to occur, and once this happens, the viscosity is roughly linear. Iverson [24] notes that this model could be adapted so that the yield stress depends on the internal friction of the material and the viscosity depends on the deformation rate, but in practice this is often not done.

Now a more complex model is often used to model natural viscoplastic materials.

Chapter 3. Theoretical models for thin-films

The Herschel Bulkley model is a generalised Bingham model and has been found to describe both snow [39] and muddy debris [55] well. The Herschel Bulkley constitutive equation has been used by many authors, [47, 53, 55, 56, 58, 112, 113, 115] and can be incorporated into the simplified Navier Stokes equations (3.3) by

$$\sigma = \begin{pmatrix} \sigma_{xx} & \sigma_{xz} \\ \sigma_{xz} & \sigma_{zz} \end{pmatrix} = \frac{(\tau_c + 2^n K \dot{\gamma}^n)}{\dot{\gamma}} \mathbf{d}, \quad (3.10)$$

where

$$\mathbf{d} = \begin{pmatrix} u_x & (u_z + w_x)/2 \\ (u_z + w_x)/2 & w_z \end{pmatrix}.$$

$\dot{\gamma}$ is defined as the second invariant of this strain rate tensor, $\dot{\gamma} = \sqrt{\frac{1}{2}\text{tr}(\mathbf{d}^2)}$, and the total stress τ is defined as the second invariant of σ , the extra stress tensor, so that $\tau = \sqrt{I_2} = \sqrt{\frac{1}{2}\text{tr}(\sigma^2)} = |\tau_c + 2^n K \dot{\gamma}^n|$.

Ancey & Cochard [53] show the lubrication method to be successful in two regimes: the diffusive regime for gentle slopes where the pressure gradient balances viscous forces and gravity has little effect; and the slope-dominated regime where pressure gradient forces become small compared to gravity and viscous forces. The slopes considered here are moderate, from 12° to 24° . Using the scaling $U^n = \rho g \sin \theta H^{1+n}/K$, the slope-dominated regime is selected and the derivation of the (dimensional) evolution equation is as follows.

Solving system (3.3), the expression for the shear stress distribution becomes:

$$\sigma_{xz} = \rho g \sin \theta (h - z) \left(1 - \cot \theta \frac{\partial h}{\partial x} \right). \quad (3.11)$$

In this case, using the approximation $\dot{\gamma} \approx \frac{1}{2}|u_z|$ for lubrication flows, the expression for $\sqrt{I_2}$ becomes $\sqrt{I_2} \approx \sigma_{xz} = |\rho g \sin \theta (h - z)(1 - \cot \theta \partial h / \partial x)|$, and $u(x, z, t)$ is found by solving the differential equation

$$\left| \frac{\partial u}{\partial z} \right| = \left[\frac{1}{K} \left(\rho g \sin \theta (h - z) \left(1 - \cot \theta \frac{\partial h}{\partial x} \right) - \tau_c \right) \right]^{1/n}, \quad (3.12)$$

with

$$Y = h - \frac{h_c}{|1 - \cot \theta \partial h / \partial x|}, \quad \text{and} \quad h_c = \frac{\tau_c}{\rho g \sin \theta}. \quad (3.13)$$

This yield surface $Y(x, t)$ separates the shear flow below from the plug flow above and is found by solving $\sigma_{xz} = \tau_c$. It should be noted that the strain rate in the plug layer is

actually slightly non-zero [116] as found using an asymptotic expansion, but for this work, the approximation of plug flow is sufficiently accurate.

With this definition of the yield surface $Y(x, t)$, the equation to solve becomes

$$\left| \frac{\partial u}{\partial z} \right| = A (1 - \cot \theta h_x)^{1/n} (Y - z)^{1/n}, \quad (3.14)$$

with $A = (\rho g \sin \theta / K)^{1/n}$ and $S = \cot \theta$. This is solved in the shear layer to give

$$u_S(x, z, t) = \frac{-nA}{n+1} (1 - Sh_x)^{1/n} \left[(Y - z)^{\frac{n+1}{n}} + C_S \right]. \quad (3.15)$$

Subscripts S and P denote the shear and plug layers respectively. Then the no-slip condition $u_S(x, 0, t) = 0$ fixes $C_S = -Y^{\frac{n+1}{n}}$, and continuity is used across the yield surface so that u_P is constant with z and given by $u_S(x, z = Y, t)$. Then

$$\begin{aligned} u_S(x, z, t) &= \frac{nA}{n+1} (1 - Sh_x)^{1/n} \left[Y^{\frac{n+1}{n}} - (Y - z)^{\frac{n+1}{n}} \right] \\ u_P(x, z, t) &= \frac{nA}{n+1} (1 - Sh_x)^{1/n} Y^{\frac{n+1}{n}} \end{aligned} \quad (3.16)$$

and the continuity equation for each layer – using no normal velocities on $z = 0$ and continuity across the yield surface – leads to

$$\begin{aligned} w_S(x, z, t) &= \frac{Sh_{xx}}{n+1} (1 - Sh_x)^{1/n-1} A \left[\frac{n}{2n+1} \left((Y - z)^{2+1/n} - Y^{2+1/n} \right) + Y^{1+1/n} z \right] \\ &\quad - (1 - Sh_x)^{1/n} AY_x \left[Y^{1/n} z + \frac{n}{n+1} \left((Y - z)^{1+1/n} - Y^{1+1/n} \right) \right], \\ w_P(x, z, t) &= \frac{Sh_{xx}}{n+1} (1 - Sh_x)^{1/n-1} A \left(Y^{1+1/n} z - \frac{nY^{2+1/n}}{2n+1} \right) \\ &\quad - (1 - Sh_x)^{1/n} AY_x \left(Y^{1/n} z - \frac{nY^{1+1/n}}{n+1} \right). \end{aligned} \quad (3.17)$$

From the kinematic boundary condition, the evolution equation for $h(x, t)$ is therefore

$$\frac{\partial h}{\partial t} + A \frac{\partial}{\partial x} \left[\frac{nY^{1+1/n}}{(2n+1)(n+1)} \left(1 - \cot \theta \frac{\partial h}{\partial x} \right)^{1/n} ((2n+1)h - nY) \right] = 0. \quad (3.18)$$

Andreini et al [62] and Anczyk & Cochard [53] compared this model to experimental results with Carbopol Ultrez 10 at varying concentrations. They found that the model worked best at slopes around 25° and less well for shallower slopes, but failed to

describe the complex behaviour observed inside the head of the fluid. Surprisingly, Ancey et al [117] found that the simpler kinematic wave approximation [118] for slightly non-uniform flows predicted the front position with time better, although the front shape was unrealistically approximated as a shock. Chambon et al [47] found a better agreement between lubrication theory and experimental results for velocity profiles in stationary surges of Kaolin and Carbopol at 0.1% concentration on a conveyor belt.

Ancey & Cochard [53] derived a composite model including an inner solution in the nose of the flow, where surface curvature was strong. Results obtained for a similar model in the Newtonian case – which did not include an inner solution at the nose – showed a close fit with experimental measurements (see chapter 4), and so it was decided that including the inner solution may well be more trouble than it is worth.

3.3 Flows of granular suspensions

An entraining avalanche or debris flow can be modelled as a granular suspension. This section discusses the definition, the properties and the complexities of a granular suspension.

Definition

A suspension is defined as a mixture of undissolved (usually solid) particles in a liquid, where the particles are of diameter $d > 1 \mu\text{m}$. Coussot & Ancey [119] present a qualitative overview of the different flow regimes possible in suspension flow, based on the type of particle interactions. Here, only non-colloidal suspensions are used, meaning that the particles are easily mixed with the suspending fluid, but can be mechanically separated (e.g. by sieving); equally, Brownian effects are assumed unimportant. The grains used are hard, non-deformable spheres, which interact through inelastic collisions and interactions with the interstitial fluid. The interstitial fluid itself is incompressible and Newtonian, and so if two particles approach each other, they can slow down significantly due to an increase in the lubrication forces (from the pressure in the squeezed fluid). A suspension is said to be concentrated when the distance between two grains is smaller than the radius of a single grain [120], and a particle volume fraction of around 0.4 usually corresponds to this definition.

A brief history of granular suspension research

In 1851 Sir George Gabriel Stokes linked the terminal velocity for a sphere falling in a viscous liquid with the frictional drag force acting on it through a law which came to be known as Stokes's law. Since then, problems involving one or two spheres in a suspending liquid have been addressed [121], leading to a comprehensive description

of dilute suspensions which behave in a Newtonian way. Increasing the volume fraction leads to a deviation from this simple behaviour [122, 123] where lubrication theory may still perform reasonably well in front prediction up to a volume fraction of around 56%, but not in the description of the internal dynamics [63]. This change in behaviour shows that non-Newtonian effects become important and these have been attributed to effects such as particle migration, dilatancy and jamming.

A variety of experimental configurations have been used to try to understand the behaviour of dense granular suspensions, usually focusing on the rheology [63, 123–132]. A rheological description has proved elusive as inhomogeneities in flowing suspensions appear due to particle migration and a bulk volume fraction is difficult to define [133]. For this reason, many authors have obtained measurements of particle concentration and internal velocities in conjunction with bulk measurements, using such methods as nuclear magnetic resonance (NMR) imaging [124, 129, 134], Laser Doppler velocimetry (LDV) [122, 135] and particle tracking / particle imaging velocimetry (PIV) [126, 136–138].

For homogeneous and isotropic suspensions, a well-accepted result is that the bulk viscosity μ_b depends on the particle concentration ϕ and the fluid viscosity μ_0 through the Krieger-Dougherty relation [139],

$$\mu_b(\phi) = \mu_0(1 - \phi/\phi_m)^{-\beta} \quad (3.19)$$

with $\beta = 2.5\phi_m$ assuming that the random close packing volume fraction ϕ_m is well defined (a fact disputed by Torquato [140]). However Leighton & Acrivos [127] observed that viscosity initially increased and then gradually decreased during the period of shear and subsequently studied particle flux in a sheared suspension [126]. They proposed that particles would be irreversibly displaced when interacting with two or more other particles and developed a probability density function for the position of a particle at time t depending on a diffusivity coefficient which was found as $D = \dot{\gamma}a^2\bar{D}(\phi)$, where \bar{D} is a self-diffusion coefficient and a is the particle radius. Later, the coefficient D was found to increase significantly for $\phi > 55\%$ [141].

Local inhomogeneities

These concepts have been expanded by adding considerations of local particle concentrations. The diffusive flux model [124] incorporates a local particle concentration which evolves in time due to spatial variations in the viscosity and in the shear rate, used in a Newtonian constitutive equation with locally varying viscosity. The particle concentration is well modelled in rectangular channels [122] and Couette cells, but not in a parallel plate rheometer [129] as no radial migration is observed. Criticisms have been made that as a continuum model, the motion of particles across the stream are not accounted for, leading to velocity profiles that are heavily “blunted” in comparison

with the theory. Further, there is no particle size consideration [142].

The “suspension balance” model [142] analyzes particle fluctuation velocities or temperature in Stokesian Dynamics simulations by splitting particle motion into a mean part and a fluctuation about the mean, in analogy with temperature in kinetic theories [143]. Here, the particle temperature is linked to the suspension pressure in conservation equations for suspension mass, momentum, and energy. This model was later extended to non-neutrally buoyant flows, in which gravitational settling plays a role [144].

Lyon & Leal [135] found that a third model for particle migration performed better than these two at reproducing their experimental data for monodisperse suspensions. This model was devised by Mills and Snabre [145] and its novelty is that the transverse diffusive flux of particles is generated by lubrication drag forces arising from microflows in the interstitial fluid during particle collisions. In this way a stress tensor resulting from particle interactions can be incorporated into the viscous stress tensor. This model correctly predicts no migration in parallel plate rheometers and has proved successful in predicting velocity profile shape in channel flows [146].

Investigating shear-induced normal stress anisotropy, Zarraga et al [147] found a linear relation between shear and normal stresses, confirming that shear-induced normal stresses were important in particle migration and re-suspension, which enabled them to calculate the particle phase pressure using a new definition for the bulk viscosity based solely on particle volume fraction,

$$\mu_b(\phi) = \frac{e^{-2.34\phi}}{(1 - \phi/\phi_m)^3} \quad (3.20)$$

with $\phi_m = 0.62$.

Due to this increased particle phase pressure, during free-surface flow particles in concentrated suspensions may migrate towards the free surface, thus causing surface deformation [136]. Ovarlez et al [128] were able to obtain local concentration and viscosity measurements for a suspension in the range 55-60% volume fraction, in which jammed and sheared zones coexisted, and migration happened quickly. They proposed a new constitutive law based on a critical shear rate, below which no flow can occur and above which the Krieger-Dougherty relation applies, with $\beta = 2$ and $\phi_m = 0.605$. Bonnoit et al [132] retrieved bulk viscosity measurements in a free surface channel flow which compared well with the local measurements found by Ovarlez et al [128], suggesting that particle migration could be neglected in the bulk dynamical description.

A successful description of bulk rheology was obtained for concentrated suspensions of $\phi \geq 56\%$ away from the front [63, 137]. A power law rheological model gave a good

fit to the velocity profiles when it was of the form

$$\sigma_{xz} = \kappa \dot{\gamma}^n \quad \text{with} \quad u(x, z, t) = \frac{n\kappa^{1/n}}{n+1} (h^{1+1/n} - (h-z)^{1+1/n}). \quad (3.21)$$

This did not apply near the front, though, as the velocity profile appeared parabolic.

Static-flowing transitions

An important issue in suspension rheology and in the present entrainment study is the transition between static and flowing grains. Heymann et al [131] found that the behaviour of concentrated granular suspensions changed from elastic solid to Newtonian with increasing shear stress. At moderate stresses which depend on the volume concentration and the duration of shear, a transition regime was found where the material began to flow. Fall et al [134] found that shear banding and yielding occurred at a lower volume fraction for non-density matched suspensions. In a later paper, Fall et al [148] showed that the critical shear rate required for yield in non-density matched suspensions was when viscous forces were comparable to gravity forces, thus homogenizing the suspension and suppressing particle sedimentation. Indeed it was found by Hanes & Inman [125] that shear and normal stresses were almost linearly related at the yield surface, suggesting that overburden weight should balance with shear stress for stratification and yield.

Suspensions may also undergo shear thickening. Brown & Jaeger [149] examined discontinuous shear thickening where there is a jump in shear stress as the strain rate is increased. They found that for settling suspensions, this regime begins when the hydrostatic pressure from overburden weight causes dilation and shearing of neighbouring particles. Further, when there is a confining stress such as the surface tension at the air-liquid interface, dilation may be frustrated, causing further frictional dissipation.

Entrainment by Newtonian Dam-Breaks

In this section the results from the first experimental campaign using Newtonian gravity-driven flows are presented, and a model is proposed for this problem, based on classical thin film theory for spreading viscous dam breaks.

4.1 Experimental results

Bulk flow

As described in section 2.2, experiments were performed to investigate the bulk dynamics of gravity-driven flows entraining different quantities of material. Specifically, the surface height profile and the position of the flow front were studied, and compared to the case without entrainment (which should follow Huppert's predictions). To this end, flows were filmed from above and from the side.

The images obtained from Camera 2 paint a clear picture. The time space plot has been created by sampling a central line of pixels in the image at each time step, then the front is found using image processing techniques in MatLab. A Newtonian dam-break will travel further if it entrains material along its path. In figure 4.1 the flow front is plotted with time for all bulk experiments performed. It is clear that the most influential parameter is l_{bed} , the length of the entrainable layer, as the front position is significantly increased with increasing l_{bed} . The bed depth δh has a small effect, and the position of the bed has no significant effect within the range considered.

Figure 4.1 also highlights the problem of calculating the position of the front as it passes over the entrainable bed. The front position was found by identifying the interface between the dark colour of the flowing material and the light colour of the rigid base. In what follows the flow front is defined as the furthest downstream point where the surface height is non-zero. As will be shown shortly the flow front contains uplifted bed material, and so the entrainable bed was also chosen to be dyed blue. Unfortunately

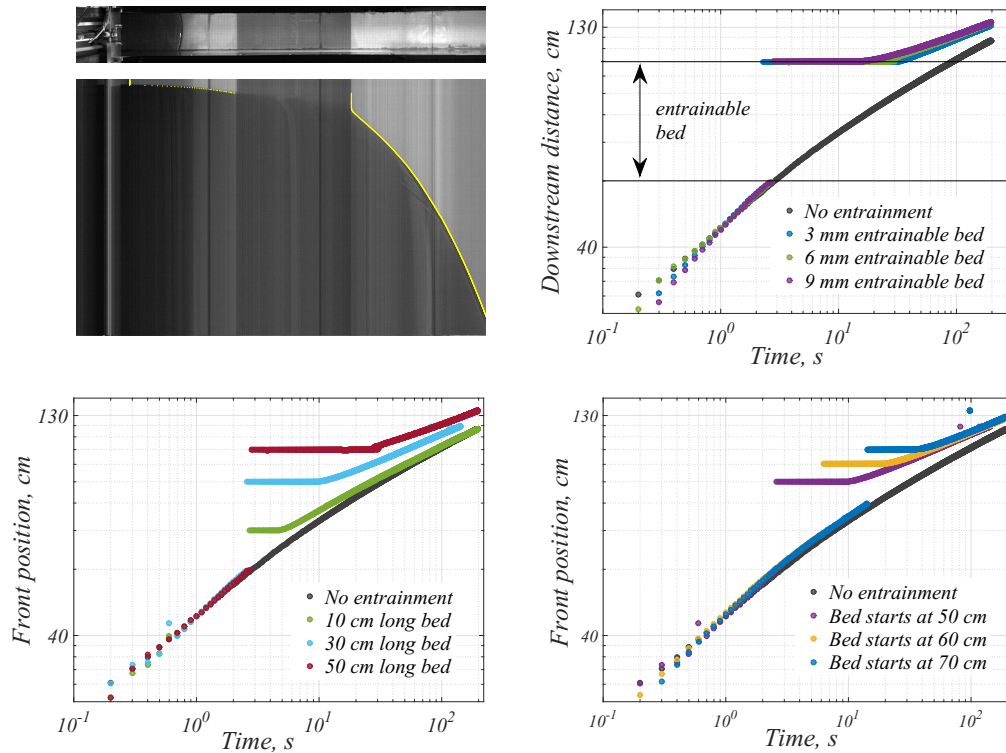


Figure 4.1: Clockwise, from top right: Space-time plot of flow front from camera 2; Front position against time – comparison of entrainable bed depths; Comparison of bed locations; Comparison of entrainable bed lengths.

this meant that camera 2 could not provide accurate flow front measurements over the entrainable bed, explaining the absence of data here.

Figure 4.2 shows surface height measurements taken from camera 3 at time intervals of 0.6 s for a non-entraining and an entraining dam-break. When the flow first contacts the entrainable bed, the total surface height profile is composed of the original current plus the initially flat surface of the entrainable layer. The mobility of the bed then allows the discontinuity at the current front to be quickly smoothed out in a diffusive way. For example, comparing experiment G with experiment A in figure 4.2, the differences are clear. Further, there is a kink in the surface just downstream of the step, here defined as a local curvature maximum, which connects the incoming dam-break with the flow over the bed at all times. This shows that after the material has moved out onto the entrainable bed, it flows away faster than the supplying gravity-driven flow.

There are two possible explanations for this. The first takes into account contact line singularities. When no entrainment occurs the dam-break flows over a rigid base and the flow front is abrupt with a moving contact line singularity at the liquid-solid-air interface [150]. If the current entrains loose material, after the flow front has made contact with the surface of the entrainable bed the only liquid-solid-air interface is at

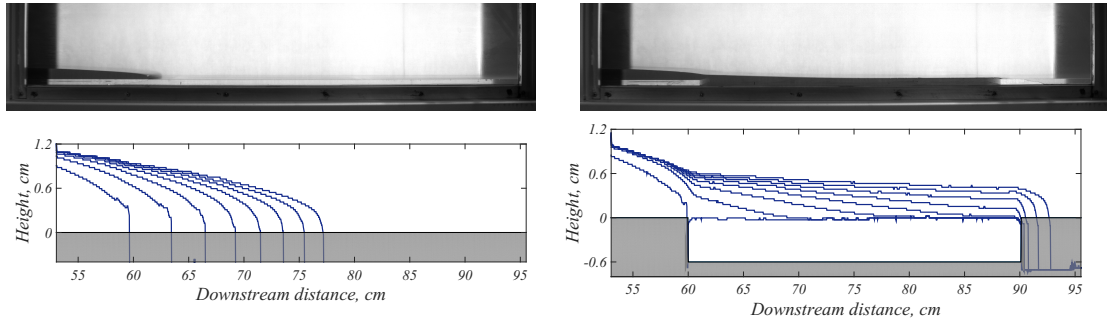


Figure 4.2: Top: Comparison of raw images from runs A (no entrainment) and G; Bottom: Surface height evolution in runs A and G. Measurements taken at 0.6 s intervals.

the end of the bed. Thus the surface height profile continuously extends to the end of the entrainable layer. Obviously this raises important questions about the moment that the flow front contacts the bed fluid for the first time. There is a singularity at the step, before which the current flows over a rigid base, and after which it flows over entrainable material. The details of this technical question will not be investigated further in this thesis, as the model developed in the following section is solved in a domain with no corners and reproduces the results well.

A second explanation involves the no-slip condition. When the current begins flowing over the entrainable bed, it is no longer subject to the no-slip condition at $z = 0$ in this region, instead this now applies at $z = -\delta h$, where δh is the depth of the bed. In this way, the stress which was acting on the rigid base now acts on the surface of the entrainable bed. The bed is quickly set into motion, which will be shown algebraically in section 4.2, allowing greater surface flow velocities as shear may occur over a greater vertical distance. A clue to the importance of this effect is given in figure 4.1. The presence of an entrainable bed accelerates the flow front, yet doubling and even tripling the depth of the bed has only a small effect. Thus it is suggested that the lowering of the no-slip condition to allow more vertical shear is less important than the removal of the contact line singularity at the step.

When the flow front reaches the end of the entrainable bed, it is seen to slow down significantly and even stop while the surface elevation increases, before flowing over the rigid base once more. Examining the side-view images, it seems that the flow thickness above the step must reach a critical value before the flow front is able to exit the entrainable zone. In the following subsection it will be shown that this behaviour is reproduced by a model which considers neither surface tension nor a geometry with corners. For this reason it is hypothesised that this is a constraint posed by the viscosity of the fluid and the no slip condition on the rigid base.

Figure 4.3 shows experiments I and J, carried out with a larger volume of 1500 ml. The idea was to see how entrainment in one area affected the avalanche bulk upstream.

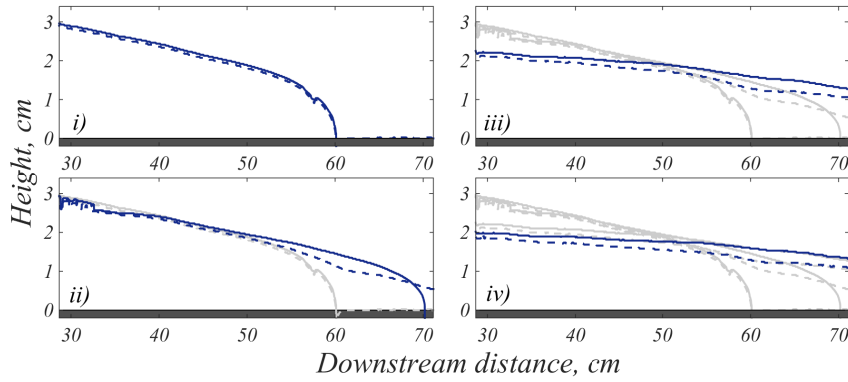


Figure 4.3: Influence of entrainment on upstream surface height profiles: i) Moment of contact with bed, t_e ii) $t_e + 1.2$ s iii) $t_e + 6$ s iv) $t_e + 12$ s.

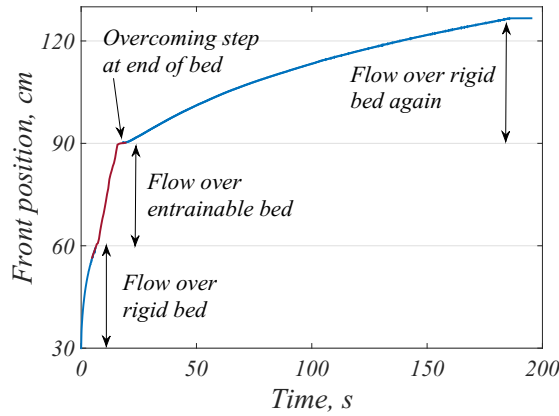


Figure 4.4: Flow front position with time for experiment G: measurements from camera 2 supplemented with measurements from camera 3.

The difference is subtle but becomes more obvious with time. In Figure 4.3 i) the two flows have roughly the same surface height profile, bar a small experimental difference. By image iv), 12 s later, there is a significant difference. As the nose of the flow moves further downstream due to entrainment, it is perhaps natural to expect, by conservation of volume, that there is less fluid upstream and therefore a decreased surface height compared to the no entrainment case.

Measurements from camera 3 are not only able to show the evolution of surface height in response to entrainment, but also to complete the picture of front propagation, as shown in figure 4.4. The conclusion is clear: the front markedly accelerates over the entrainable bed.

In the next subsection, internal velocity measurements will be examined to complete the picture of the interaction between gravity-driven flow and entrainable bed.

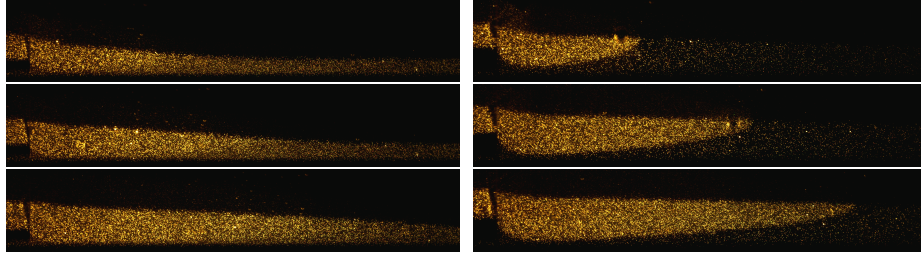


Figure 4.5: Left: 3mm-deep bed, configuration “C” for surface identification and PIV data. Right: 6mm-deep bed, configuration “R” for interface identification.

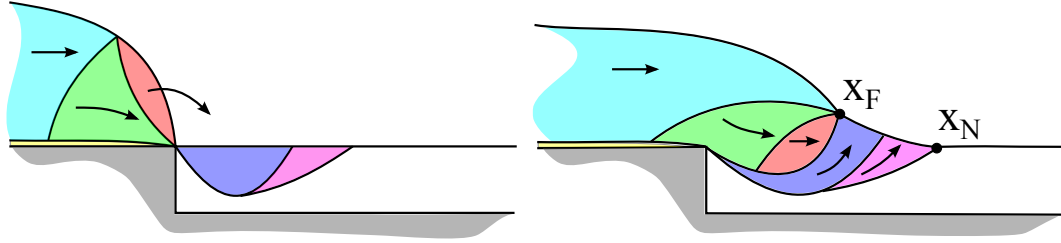


Figure 4.6: Schematic to show the displacement of the entrainable bed by the incoming avalanche.

The internal velocity field

Figure 4.5 shows the raw images obtained using camera 1, and it is now possible to tackle the question: how do the flow and the entrainable bed interact? On the left are images from the combined “C” runs where the entire flow is visualised, and on the right are images from the reservoir “R” runs where the bed surface is shown to be deformed as the current passes over it.

The bed fluid is set into motion almost instantaneously when the flow front makes contact with its surface. The motion is predominantly due to streamwise shear as the horizontal velocity in the front is greater than the vertical velocity but there is a small normal force which causes weak vertical velocities in the bed. After the bed fluid is set into motion, the current sinks downwards near the step to replace the material that has been advected downstream, explaining the convex shape of the current/bed interface shown in the right-hand images of figure 4.5. Figure 4.6 shows this process schematically.

In figure 4.7 the velocity components (\hat{u}, \hat{w}) at $t = t_e + 1$ s (1 s after entry into the entrainable bed) found from PIV, are shown as contours and a vector field, here non-dimensionalised with the scalings: $x \rightarrow L\hat{x}$, $(h, z) \rightarrow H(\hat{h}, \hat{z})$, $u \rightarrow U\hat{u}$ and $w \rightarrow \epsilon U\hat{w}$, where $\epsilon = H/L \ll 1$ and $U = \epsilon^3 L^2 g / \nu$ m s⁻¹. The values for these dimensional parameters were $L = 1$ m, $H = 0.0185$ m (which comes from the modelled maximum flow height when Huppert’s solution arrives at the step), $\nu = \mu/\rho = 8.915 \times 10^{-4}$ m²

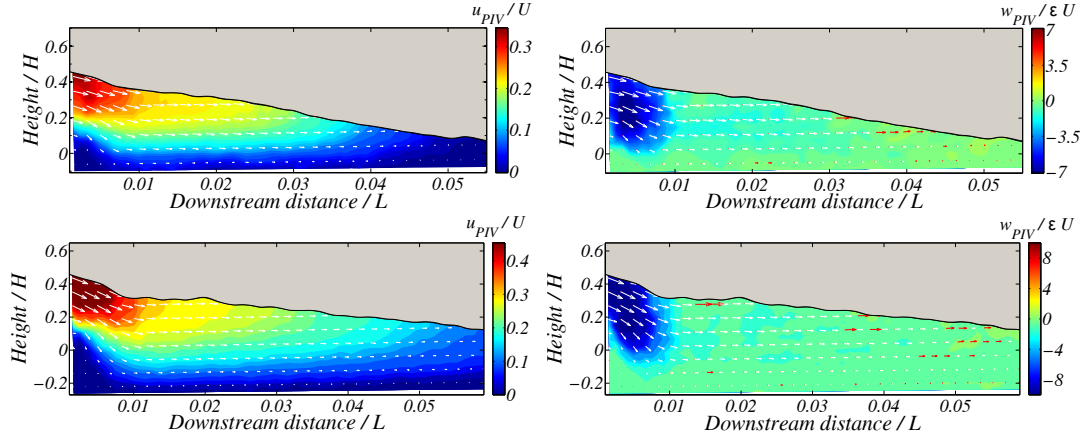


Figure 4.7: Contour plots for horizontal and vertical velocity after 1 s with velocity vectors. In the vertical velocity plots the positive velocity vectors are highlighted in red. Top: 3 mm step, bottom: 6 mm step.

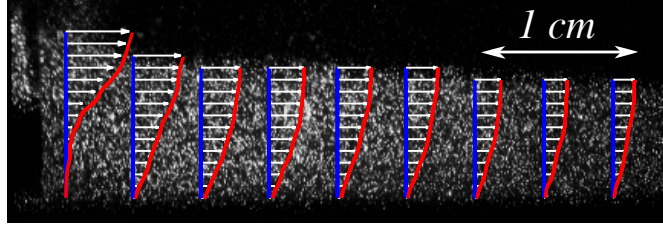


Figure 4.8: Velocity profiles in 6 mm deep bed, after 1 s flow.

s^{-1} and $g = 9.81 \text{ m s}^{-2}$. When t is non-dimensionalised, its scaling is $T = L/U = \nu L^2/H^3 g = 14.27 \text{ s}$.

The motion is predominantly horizontal, as shown by the vectors in all velocity fields. The left hand images show the horizontal velocity, \hat{u} , which is strongest just above the step. In the case with the deeper bed, the flow is faster and fluid is in motion farther downstream after the same amount of time. In the right hand plots of vertical velocity, the deeper bed also induces stronger velocities, but it is more enlightening to look at the direction of the flow. Near the flow front some regions of positive \hat{w} are found, indicated by red arrows, which show that when the dam-break flows into the entrainable bed it induces uplift of bed material further downstream. This explains why, if the flow front $x_N(t)$ is defined as the furthest point downstream with $h(x, t) > 0$, it is further downstream than the front of the original current, called the interface front, $x_F(t)$ (see figure 4.6).

In all cases there is a stagnant corner next to the step where there is no flow. Figure 4.8 shows the horizontal velocity profiles, which are typical of viscous fluids, except for next to the step, where the velocity profile has a concave shape. Fluid in this corner will not be entrained or replaced by incoming fluid.

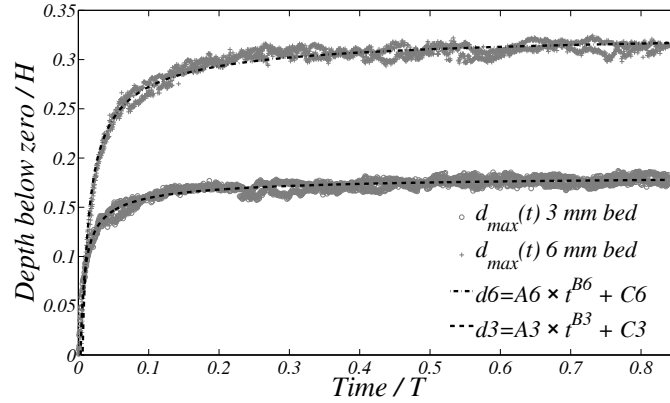


Figure 4.9: Progression of $d_{max}(t)$ (dimensionless) for 3 mm and 6 mm deep beds. A power law has been fitted to each set of data to guide the eye. The parameters are $\{A_3, B_3, C_3\} = \{-0.0070, -0.573, 0.186\}$ and $\{A_6, B_6, C_6\} = \{-0.0155, -0.6, 0.334\}$.

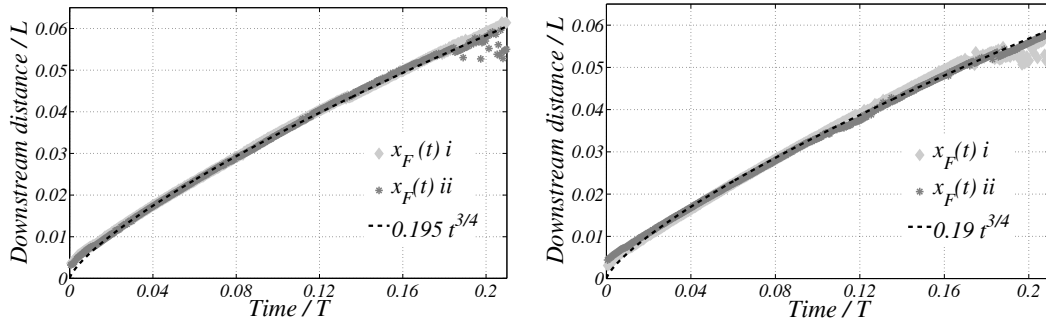


Figure 4.10: Progression of $x_F(t)$ for 3 mm (left) and 6 mm (right) beds. The two data sets correspond to two different experiments.

Using the “R” runs, it is possible to study the progression of the current as it flows across the entrainable bed surface, by measuring the position of the flow parameters $d_{max}(t)$ (the maximum depth of the interface) and $x_F(t)$ (the furthest downstream extent of the current flowing atop the bed - see figure 4.6).

Figure 4.9 shows the rate at which the current sinks into the bed, this can be thought of as digging, or displacement of the bed by the avalanche. Once the bed fluid is in motion, the current flows down the stepped geometry under gravity. During the first phase, d_{max} increases rapidly with t , then its progression slows, and finally it tends towards a constant value, when the rigid base stops any further displacement from occurring. Finally, since the gravity-driven flow is created from a finite volume the velocities are weaker in the tail, so that when the latter parts of the current are passing over the bed, they have much less of an effect. The progression of d_{max} can be fitted by the rule $d_{max}(t) = A_i \times t^{B_i} + C_i$ where $\{A_3, B_3, C_3\} = \{-0.007, -0.573, 0.186\}$ and $\{A_6, B_6, C_6\} = \{-0.0155, -0.6, 0.334\}$.

Figure 4.10 shows that the position of the interface front x_F is largely unchanged by the depth of the entrainable bed, and when a curve is fitted to the data, a similar power law with exponent $t^{3/4}$ rule for both a 6 mm- and 3 mm-deep bed apply. Any differences are probably due to effects of lighting quality on the identification of the interface.

The above trends are different from those obtained for earlier experiments with a bed 13 mm deep by 50 cm long [151], which aren't presented here. There, a clear trend was found for a range of different released volumes, with the non-dimensionalised values of d_{max} collapsing onto a curve described by a $t^{1/2}$ power law at first, and a $t^{1/5}$ law later. The interface front position x_F was also plotted but did not collapse as neatly and gave different exponents from those found above. This shows that those flows propagating over a shallow entrainable layer should be treated differently from those flowing over a deeper bed.

4.2 A model for entrainment by Newtonian gravity-driven flows

The theoretical model for this problem is inspired by Huppert's model (equation 3.7), adding an extra contribution from an entrainable layer which leads to a significant advancement of the flow front over the entrainable material as in figure 4.6. The experiment is modelled as a two-dimensional viscous dam-break in x and z , ignoring the cross-plane direction y . The current is released suddenly from a reservoir and initially flows without entrainment until the front encounters an entrainable region, exactly as in the experiments described above. The entrainable zone contains a layer of loose entrainable material, held initially at rest behind a backwards step. This material lies between $z = 0$ and $z = b(x) \leq 0$, defining a rigid base below which entrainment is impossible.

The entrainment process is considered as two separate problems: as the entrainable layer is initially at rest, there should be a short period during which this material is set into motion by the incoming current. Once in motion, the fluid from the bed flows together with the fluid from the current in the stepped geometry. The experiments showed that the bed is set into motion almost instantaneously. Thus only the leading order shearing effects of the front are important for this process. There is a boundary layer at the front of the current in which surface curvature is strong and vertical velocities are non-negligible, but its effects are second order [53]. The time scale of the setting into motion of the fluid is so fast that normal forces from the front are negligible on this timescale. The bed fluid is sheared and separates from the step, quickly being replaced by the incoming current, and thus the second of the two processes becomes dominant.

Further, from Huppert [49] the shape of the current may be approximated by a deforming box characterised by a very steep front (e.g. [152], [153]). Using this simplification

4.2. A model for entrainment by Newtonian gravity-driven flows

the problem becomes reminiscent of the Rayleigh problem of a sudden tangential motion on the surface of the half plane [154]. A brief dimensional analysis shows that the associated timescale is $T_c = (\delta h)^2/\nu$ s, which is $O(10^{-2})$ s for this problem. For this reason the suitability of Huppert's near equilibrium solution is justified from the first instances of bed-current interaction in our geometry.

As the entrainable layer has been set into motion, the entire velocity field may be treated as continuous, including the stationary material far downstream of the flow front. Fluid occupies the space between the bottom basal function $b(x) \leq 0$ and $h(x, t)$ the surface height of the flow, which comprises the surface of the flow and the surface of the entrainable bed at $z = 0$ if the flow front has not yet arrived. The time $t = 0$ corresponds to the front of the avalanche arriving at $x = l_{step}$, the location of the backwards step where the entrainable bed begins as shown in figure 4.6, thus the initial profile $h(x, t = 0) = h_0(x)$ is the Huppert solution with front position $x_H = l_{step}$ for $x < l_{step}$, and $h_0 = 0$ for $x > l_{step}$. The no-slip condition on the base is $u(x, z = b, t) = 0$ when the extra material is included in the flow. Following Huppert [49], the current is assumed to have small surface curvature (this is only violated near the front, and despite this the results are satisfactory) and that surface tension is negligible.

A dimensional analysis leads to the scalings

$$x \rightarrow L\hat{x}, \quad (h, z) \rightarrow H(\hat{h}, \hat{z}), \quad u \rightarrow U\hat{u}, \quad w \rightarrow \epsilon U\hat{w}, \quad p \rightarrow \rho g \epsilon L \hat{p}, \quad t \rightarrow \frac{L}{U} \hat{t} \quad (4.1)$$

with $\epsilon = H/L \ll 1$ and $U = \epsilon^3 L^2 g/\nu$. The new base function $b \rightarrow H\hat{b}$ describes a shallow cavity containing an entrainable layer of depth δh , where $|\delta h| \ll h$. Then, the Navier Stokes equations in the inertia-less regime become

$$\begin{aligned} \frac{\partial \hat{p}}{\partial \hat{z}} &= -1, \\ \frac{\partial^2 \hat{u}}{\partial \hat{z}^2} &= \frac{\partial \hat{p}}{\partial \hat{x}}. \end{aligned} \quad (4.2)$$

Dropping the hats for simplicity,

$$p(x, z, t) = h - z,$$

and $u(x, z, t)$ is found using the no-stress surface condition and the no-slip condition on the rigid base $b(x)$ whose geometry is non-trivial. $w(x, z, t)$ is calculated from the continuity equation, $w_z = -u_x$ with the condition $\mathbf{u} \cdot \mathbf{n} = 0$ on $b(x)$, giving expressions

Chapter 4. Entrainment by Newtonian Dam-Breaks

for the velocity field in the flow comprised of the entrainable bed and the dam-break:

$$\begin{aligned} u(x, z, t) &= \frac{h_x}{2} (z^2 - 2hz - b^2 + 2hb), \\ w(x, z, t) &= -\frac{1}{2} \left[h_{xx} \left(\frac{z^3}{3} - hz^2 + 2hbz - b^2z + \frac{2b^3}{3} - hb^2 \right) \right. \\ &\quad \left. + h_x^2 (2bz - z^2 - b^2) + h_x b_x (hz - bz + b^2 - hb) \right]. \end{aligned} \quad (4.3)$$

The kinematic boundary condition, stating that a particle on the surface remains on the surface throughout the flow, is used to relate h , u and w on the surface, $z = h(x, t)$.

$$\frac{\partial h}{\partial t} + u(x, z, t)|_{z=h} \frac{\partial h}{\partial x} = w(x, z, t)|_{z=h}. \quad (4.4)$$

So using (4.3) in (4.4) the differential equation to solve simplifies to:

$$\frac{\partial h}{\partial t} - \frac{1}{3} \frac{\partial}{\partial x} \left[\frac{\partial h}{\partial x} (h - b)^3 \right] = 0, \quad (4.5)$$

which is nothing less than the Huppert surface evolution equation with a correction for the basal geometry.

The total fluid in the system is conserved, i.e. the volume per unit width of the fluid released by the dam-break, V_0 , together with the bed fluid. When fluid is displaced below $z = 0$, experiments have shown that this is balanced by fluid uplift downstream, advancing the front $x_N(t)$ as shown in figure 4.6 and in section 4.1. Thus conservation of fluid gives

$$\int_0^{x_N(t)} h(x, t) dx = \hat{V}_0$$

where $x_N(t)$ is the value of x at the front such that $h(x_N, t) = 0$, and $\hat{V}_0 = V_0/\epsilon L^2$ is the dimensionless volume per unit width. The upwards forcing of the bed fluid means that x_N , the corrected front, lies further downstream than x_H , the Huppert solution for the front position in (3.9).

An asymptotic solution to the problem was sought as the dimensionless Huppert solution plus a correction of order δh (the small depth of the bed), yet no solution was found that satisfied the no-flux boundary condition at $x = 0$ whilst also remaining bounded in time. As the full analytical solution to this problem was not readily obtained, numerical methods had to be adopted.

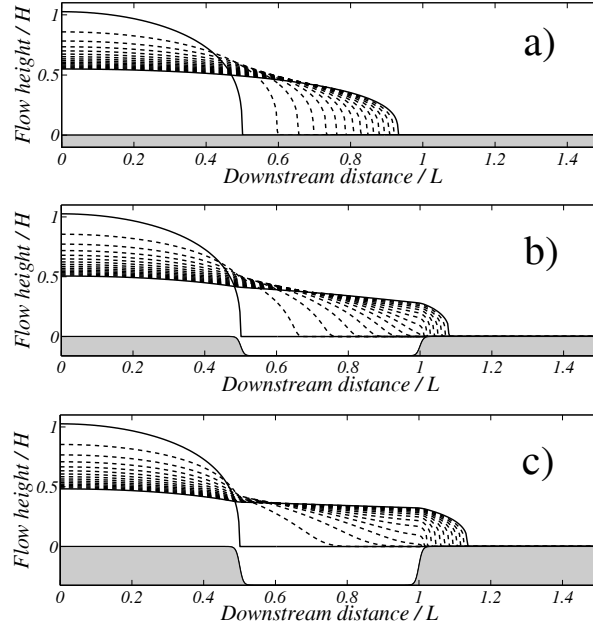


Figure 4.11: Current enters entrainable zone of length 0.5, progression from $t = 0$ to $t = 4.4984$ (60 s dimensional time). Profiles are plotted every 4 s or 0.3 dimensionless time. Top to bottom: Bed depth $\delta h = 0$, Huppert solution; $\delta h = 3 \text{ mm}/H$; $\delta h = 6 \text{ mm}/H$.

4.3 Numerical solution

The parabolic solver *pdepe* in MatLab [155] was used to solve the dimensionless problem (4.5) in order to make a comparison with the experimental results. $b(x) = -\delta h/2(\tanh(100(x - l_{step})) - \tanh(100(x - l_{step} - l_{bed})))$ was used as an approximation to the basal geometry with an entrainable bed of length l_{bed} beginning at l_{step} , before the avalanche runs out over a rigid base. This function was chosen to approximate the stepped base as smoothly as possible, thus optimizing the grid size and minimizing the calculation time. Defining no-flux boundary conditions at each end, the surface height with time is found and (4.3) gives the velocity field for $z < h(x, t)$.

Experiments showed that when entrainment occurs, the current flows onto the bed, sinking in and displacing downstream material upwards, leading to the diffusion of strong surface height gradients and the downstream propagation of the front position x_N . This also occurs in the numerical results, as shown in figure 4.11, where after 60 s dimensional time the front which has flowed over the deepest bed has progressed the furthest. Further, the surface height profiles predicted are remarkably similar to those observed in figure 4.2.

The main goal is to establish the suitability of the model for the flow it is designed to describe. Figure 4.12 shows the (dimensional) front position with time for run G, taken

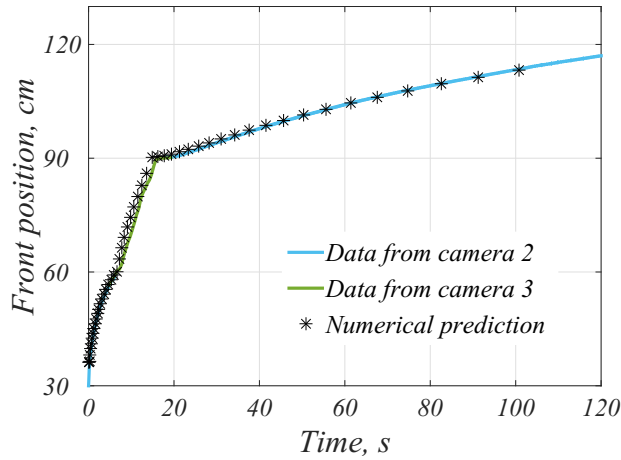


Figure 4.12: Comparing the numerical and experimental results for front progression in experiment G.

from cameras 2 and 3. A numerical simulation with exactly the same parameters was performed and the front position was identified as the furthest point downstream with $h > 0.0005$ m, chosen to correspond to the resolution of camera 3. The comparison shows a close agreement over the entire domain – before the bed, while the front passes over the bed and after the front has left the bed – thus confirming the appropriateness of this model.

The modelled internal flow features are compared with the results from the experiments performed in section 4.1 and all non-dimensionalisations use the same scalings. Contour plots for the velocity field in figure 4.13 show that during entrainment the horizontal velocity is strongest above the step and decreases downstream (plots (a) and (b)), and that there is a region of upwards motion near the flow front (plots (c) and (d)). This is in agreement with the velocity fields obtained from experiments after the same amount of time (figure 4.7). Further, the velocities are quantitatively similar to those observed: the velocity magnitude and the shape of the contours resemble the predictions, especially for the horizontal velocity. The slight difference in vertical velocity magnitudes between the numerical and experimental results can be explained by the approximation of the step by a hyperbolic tangent, chosen to minimise calculation time. In panels (c) and (d), there is a region of upwards motion above the step which was not detected in the experiments. Its origin is likely to be the steepness of the hyperbolic tangent function, which should require a smaller grid size near the step, but since the model performs well in all other aspects, this anomaly is considered to have little effect, and the grid size is kept. When the front reaches the run-out zone, the strongest velocities are again localised at the flow front (plots (e) and (f)). Finally, the surface shape has a kink above the step where the flow front has been advected

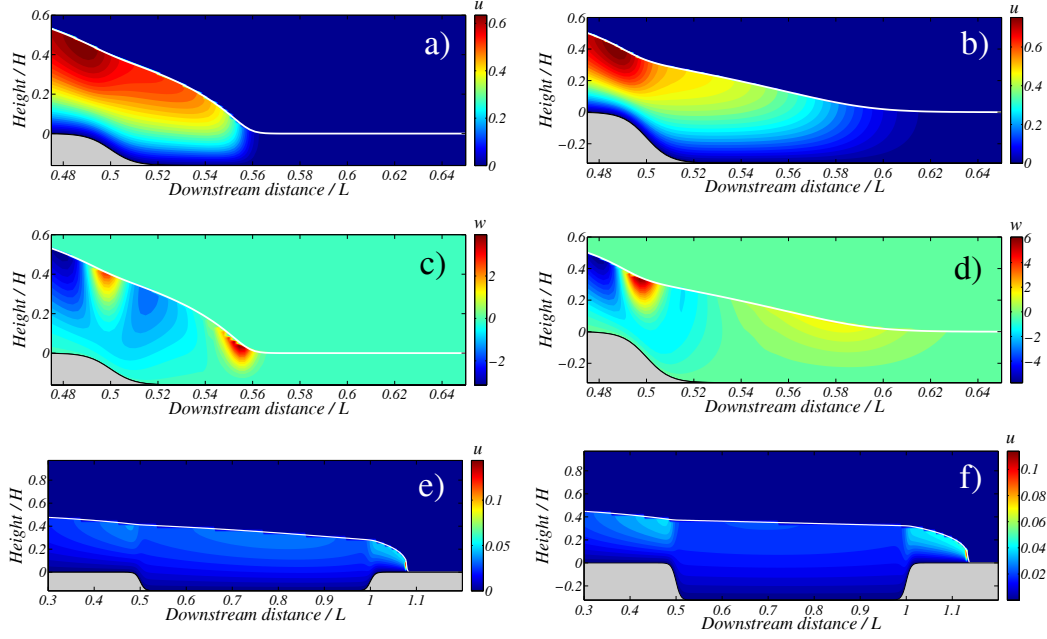


Figure 4.13: Contour plots for modelled non-dimensional velocities (u, w) inside the entraining avalanche, $l_{bed} = 1/2$. a) u , $d = 3$ mm, $t = 0.075$ (1 s); b) u , $d = 6$ mm, $t = 0.075$; c) w , $d = 3$ mm, $t = 0.075$; d) w , $d = 6$ mm, $t = 0.075$; e) u , $d = 3$ mm, $t = 4.4984$ (60 s); f) u , $d = 6$ mm, $t = 4.4984$.

over the bed, exactly as in figure 4.2.

Further, to obtain a direct comparison, the PIV and modelled measurements for the horizontal velocity are plotted on the same graph in figure 4.14. Near the step the model performs exceptionally well, despite the approximation of the step by a \tanh function. Further downstream, the surface height is overestimated, and thus the velocities are overestimated, yet the predicted values are well within the same order of magnitude as the measurements.

It is also of interest to see if the numerical current/bed interface evolves in the same way as in the experiments, with the same deformation and transport of entrained material. This was studied as a simple advection problem where an indicator function ϕ – which is equal to 1 for $-\delta h < z \leq 0$ and 0 for $z > 0$ – is used in the advection equation

$$\frac{\partial \phi}{\partial t} + u \frac{\partial \phi}{\partial x} + w \frac{\partial \phi}{\partial z} = 0 \quad (4.6)$$

on an Arakawa C-grid [156]. An external velocity field (figure 4.13), was applied to the system, found above on a non-dimensional domain $1.1 \times (1 + \delta h)$ with a grid of size 0.022×0.05 . The time step was chosen as 2.5×10^{-4} in order to satisfy the CFL condition $u_{max} \Delta t / \Delta x + w_{max} \Delta t / \Delta z \leq 1$. The shape of the interface is plotted in figure

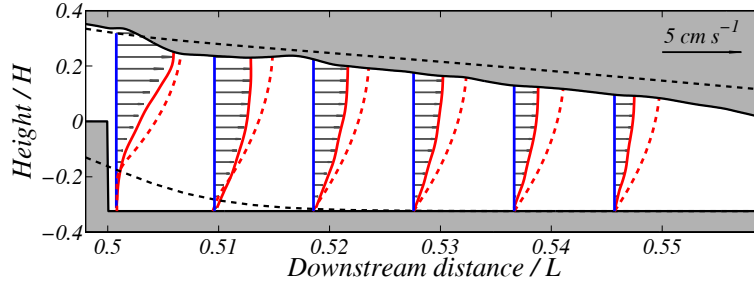


Figure 4.14: Velocity profiles in 6 mm deep bed, after 1 s flow: comparison between PIV measurements (solid lines and arrows) and model predictions (dashed lines)

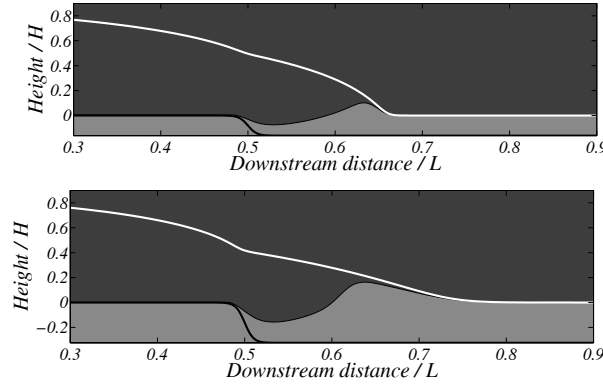


Figure 4.15: Current/bed interface for modelled flows over an entrainable bed after 4 s dimensional time. Left: $\delta h = 3 \text{ mm}/H$; Right: $\delta h = 6 \text{ mm}/H$. Rigid base function shown in black.

4.15 and it is qualitatively similar to the right-hand plots of figure 4.5. Its progression was quantified (figure 4.16) by looking for its lowest point, d_{max} , and its downstream extent, x_F (as previously defined). Near x_F the interface has been forced upwards, in accordance with the positive vertical velocities shown near the flow front in figure 4.13. Numerical diffusion of the interface occurred but the results capture the essential details of entrainment.

Looking at the progression of d_{max} in the upper panels of figure 4.16 there appears to be a slight difference between simulations and experiments. Here, the excavation of the bed is slower and shallower, being described by a $t^{1/2}$ rule at early times. An explanation for this is that the modelled step was a hyperbolic tangent, and not a full step function. However later on an excellent fit is obtained by using a similar rule as that used for the experimental data, and the bed is excavated as $\alpha_i t^{\beta_i} + \gamma_i$ where $\{\alpha_3, \beta_3, \gamma_3\} = \{-0.0121, -0.57, 0.120\}$ and $\{\alpha_6, \beta_6, \gamma_6\} = \{-0.0238, -0.6, 0.237\}$. The lower panels present $x_F(t)$. This point was found by looking at the highest point of the interface, corresponding to the front of the original current which has been forced

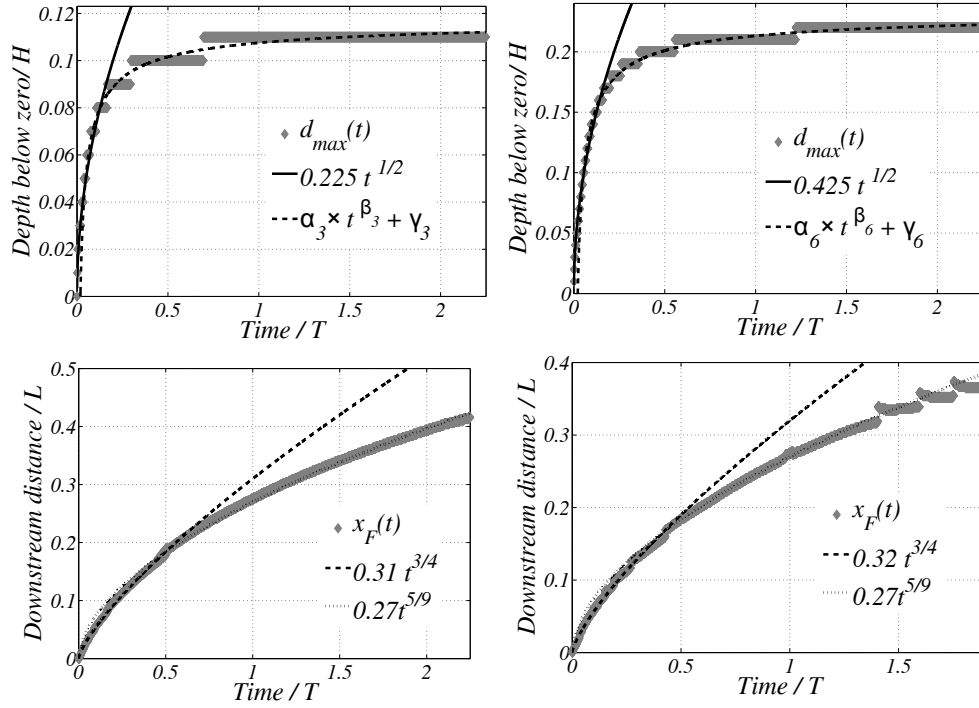


Figure 4.16: Progression of the current/bed interface (left: $\delta h = 3 \text{ mm}/H$; right: $\delta h = 6 \text{ mm}/H$). Top: d_{max} , maximum interface depth (the stepped shape is due to the grid resolution). Bottom: $x_F(t)$, interface front.

upwards (as in figure 4.16). It evolves initially with $t^{3/4}$ and later with $t^{5/9}$. There is little difference between the two cases, suggesting that the bed depth has little influence on x_F , as found in the experiments. The experiments also showed a $t^{3/4}$ rule, but the observation window was not long enough to measure the later progression.

4.4 Discussion

Figure 4.12 shows that the model (4.5) provides an excellent reproduction of bulk experimental results, despite numerous simplifications. Further, on closer examination, the model produces similar internal velocities and the current excavates the bed in a similar manner, which is encouraging given the simplifications of the geometry and the potential for experimental error.

This tells us some interesting things about the experiments. First, the model ignores surface tension and supposes that longitudinal variations and vertical velocities are small, which may not be the case in the tip of the current. Nevertheless the front propagation and the surface shape are excellently reproduced. Thus it can be inferred that these excluded effects are not important – at least to first order – in the physical problem.

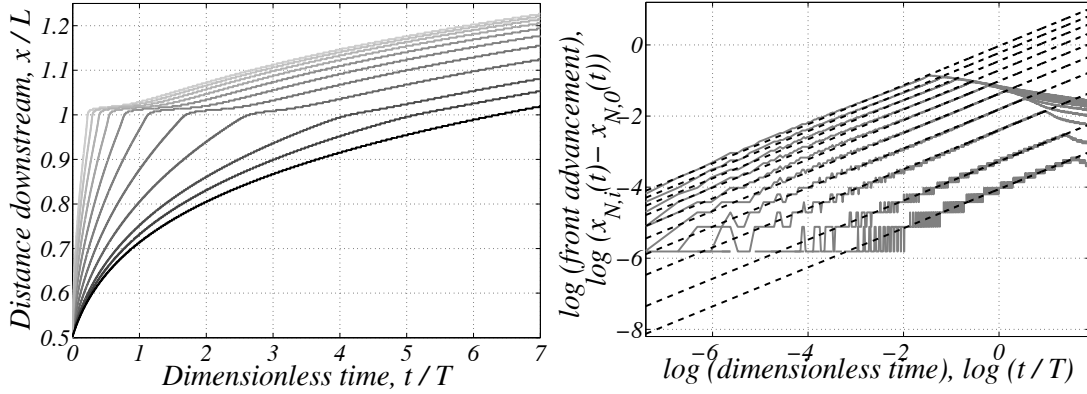


Figure 4.17: Left: Front progression with time, $x_N(t)$ for a range of bed-depths, $l_{bed} = 0.5$ over 100 s dimensional time. The dimensional bed depths b_i are $\{0, 0.5, 1, 2, 3, 4, 5, 6, 7, 8, 9\}$ mm, corresponding to lines shaded from dark to light. Right: Log-log plot of front advancement with time, $\Delta X_i(t) = x_{N,i}(t) - x_{N,0}(t)$, for a bed of i mm compared with no bed. The initial progression is fitted by $\log \Delta X_i(t) = 5/9 \log t + C_i$, where $C_i \approx \log(3.174 \max |b_i|^{1.646})$.

Second, the flow was modelled on a smooth geometry with \tanh functions instead of sharp corners. While this may have had a small effect on internal measurements, bulk measurements showed no sensitivity to this, which means that it is perhaps not worth worrying about the effects of such a singularity on the flow front as it passes from rigid base to entrainable bed surface and vice versa. When the flow front reached the end of the bed, the surface height increased until it was a few millimetres high before it continued to flow over the rigid base. As no surface tension was considered nor was there an angular corner in the model, the model's good reproduction of this bulging behaviour means that it can be attributed to the viscosity of the fluid alone, which controls the velocity gradient. The front must again travel over a rigid base, with zero velocity at $z = 0$ and so the surface must be a certain elevation for it to flow at a detectable velocity.

Finally the good agreement shows the merits of incorporating the entire bed into the flow, instead of considering a local mass exchange. Perhaps this is obvious due to the simplicity of the fluid but it will be useful when considering the more complex fluid used in the next chapter.

The success of the model and simulations in reproducing the experimental results means that rules can confidently be inferred from non-dimensional numerical experiments. In figure 4.17, the front progression over the bed is examined for different flow depths. As is shown here, the front advancement due to entrainment seems to saturate for deeper beds, showing again that the most important factor is the presence of the entrainable bed, and its depth is secondary.

Defining $\Delta X_i(t) = x_{N,i}(t) - x_{N,0}(t)$ as the front advancement over an entrainable bed i mm deep compared with the rigid base case $x_{N,0}(t)$, the distance gained by the front due to entrainment can be quantified. During the front progression over the entrainable material, the front advancement (defined as $\Delta X_i(t) = x_{N,i}(t) - x_{N,0}(t)$) can be described by a power law, as shown by the straight lines fitted on the log-log plot. The straight lines on this figure are $\log \Delta X_i(t) = 5/9 \log t + C_i$, where C_i was found to be $\{-4.056, -3.277, -2.396, -1.814, -1.373, -1.018, -0.715, -0.4535, -0.2264, -0.03068\}$, therefore $x_{N,i}(t) = x_{N,0}(t) + \exp(C_i) \times t^{5/9}$. Finally, the coefficient $\exp(C_i)$ can be related to the non-dimensional bed depth $\max|b_i|$ by a power law $\exp(C_i) = A \times \max|b_i|^B$, where $A = 3.174$ and $B = 1.646$ give an excellent fit. After the front reaches the end of the bed it slows down, and there is a transition period before the front moves according to a new regime, in which the curve is parallel to the Huppert solution. The front advancement due to the flow passing over an entrainable bed seems to be permanent. Any study at long times would probably need to take into account surface tension to see where the current stopped.

Entrainment by Viscoplastic Avalanches

This section takes what was learnt in the previous chapter and builds on it, in order to apply the developed experimental and theoretical techniques to an entraining gravity-driven flow on a slope.

5.1 Experimental results

Bulk measurements

In order to investigate the question of what happens to a viscoplastic avalanche due to the entrainment of stationary material lying in its path, experiments were performed as detailed in section 2.3. Camera 2 filmed a bird's eye view of the dam-break down the length of the flume, and from these images it was possible to isolate the front position. In what follows the front is defined as the furthest downstream point with positive surface elevation, with the entrainable bed surface at $z = 0$ for $t = 0$. Figure 5.1 shows the position of the front with time in two experiments. In contrast to the Newtonian flows, the front finding algorithm often picked up the flow front over the bed – the translucent nature of the Carbopol meant that the shallow bed (pale blue) could easily be distinguished from the steep flow front (dark blue) – but this was not always the case (usually when the bed was deeper and darker, or if dark spots were seen in the bed) and the front had to be isolated manually in some cases.

Figure 5.2 shows a comparison between a non-entraining flow and its entraining equivalent, with images taken at the same time intervals. Choosing one slope, for example 20° , the flow front can be tracked over the entrainable bed, and compared between different bed sizes. Clearly the presence of entrainable material advances the flow front. By image (d) the difference is clear – the entraining flow front has almost exited the observation zone, whereas the non-entraining flow front is several centimetres behind.

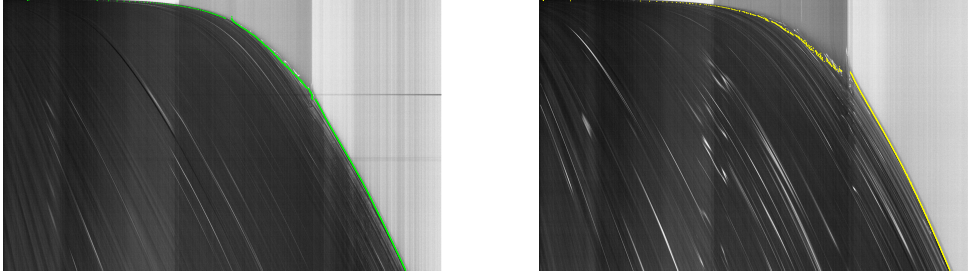


Figure 5.1: Time-space plots from camera 2, showing front progression and bed position. Experiments 16-3Cc & 16-6Cc.

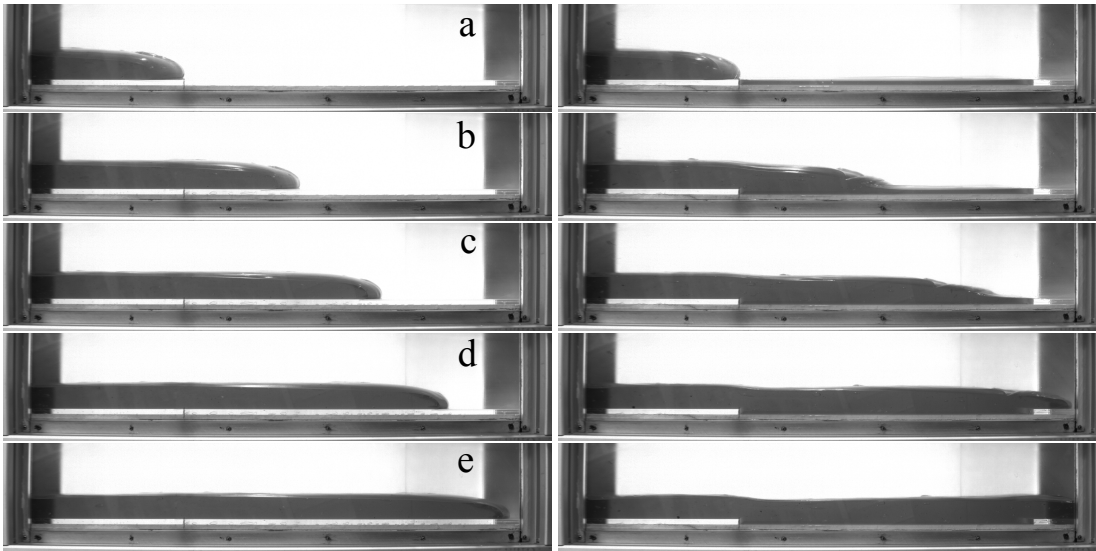


Figure 5.2: Experiments 20-0a and 20-6Ca. a: entry time, $t = t_e$. b: $t = t_e + 45$ s. c: $t = t_e + 112.5$ s. d: $t = t_e + 202.5$ s. e: $t = t_e + 315$ s.

Quantifying the effects of entrainment on the dam-break by looking at the position of the flow front allows us to determine what the most important control is on avalanche front speed. In figure 5.3 (a) four experiments are compared with increasing bed depth: 16-0c, 16-3Cc, 16-6Cc and 16-9Ca. Clearly the bed depth is an important controlling parameter as the flow front travels further over an entrainable bed than over a rigid base, and this effect increases significantly with the depth of entrainable material, in contrast to what was observed for Newtonian flows.

A longer entrainable bed also increases the flow front position in a roughly linear way, for example, in figure 5.3 (b) the flow fronts are advanced by approximately 2 cm, 5 cm and 8 cm for bed lengths of 10 cm, 20 cm and 30 cm respectively. These are experiments 20-0a, 20-6Ca 20-6Cb and 20-6Cd. In some experiments the position of the entrainable bed was varied but this comparison had no clear conclusion.

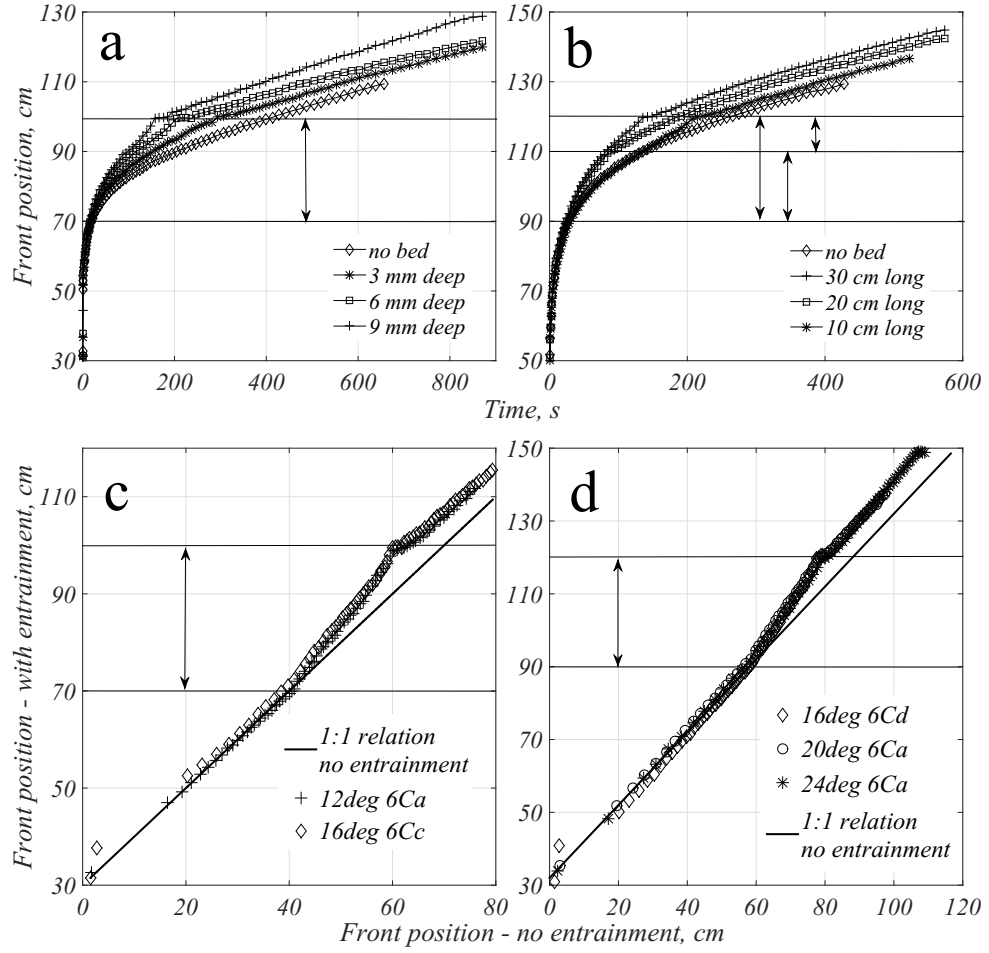


Figure 5.3: (a) Front position with time for flows over entrainable beds of increasing depth: 16° slope, 30 cm-long bed as indicated by arrow. (b) Front position with time for flows over entrainable beds of increasing lengths, indicated by arrows. 6-mm deep bed at 20°. (c & d) Comparing front position between entraining and non-entraining flows for different slopes.

Finally experiments conducted at different slopes were compared, however this posed a problem. It was expected that using the time scaling $T = (\rho g \sin \theta H^{1+n} L^n / K)^{1/n}$, in the slope-dominated regime [53] would allow a direct comparison of slope effects, but this was not found to be the case. The curves of front position against time did not collapse, with the dimensionless flow front travelling faster at steeper slopes. So in order to examine the effect of flume inclination on entrainment, at each slope the flow front of an entraining flow was plotted against its non-entraining equivalent. Figure 5.3 (c & d) shows clearly that slope has no effect on front advancement, defined as the distance gained by the avalanche front due to entrainment of loose material. For each slope considered the curves collapse neatly on top of each other, meaning that entrainment of material has the same effects at each slope studied here.

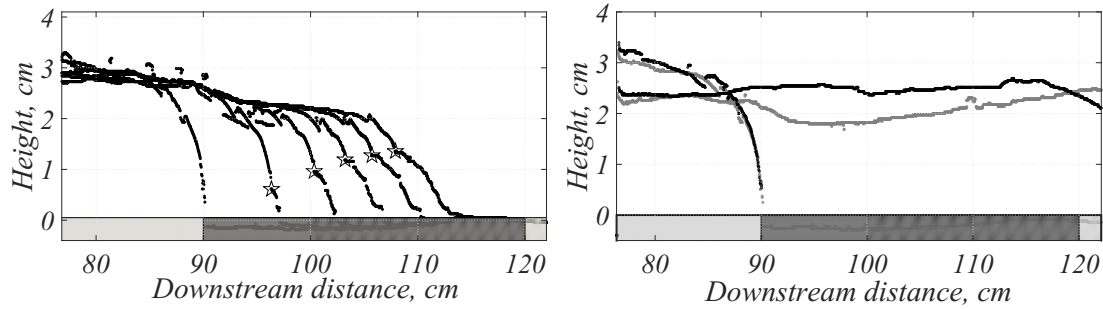


Figure 5.4: L: Progression of surface profile including surface irregularity (stars) originating from the original dam-break front. 6 mm deep by 30 cm long bed at 20° . R: Difference in surface height profiles, avalanche flowing over entrainable bed (experiment 20-6Ca, light colour) versus avalanche on a rigid base (20-0a, dark colour).

Clearly the quantity of entrainable material is the most important parameter here, causing the front to travel faster downstream when more loose material is available. To begin to answer the question of how entrainment leads to the advancement of the flow front, images from camera 3 are used to study the evolution of the surface height of the avalanche over the bed. For example, figure 5.2 shows the upright front shape when no entrainment is possible, compared to the more oblique front when there is entrainable material available.

This is due to the entrainable material lifting up downstream of the avalanche front, in a similar way as for the Newtonian case discussed in section 3. The difference here is that it occurs locally with no effect further downstream. In figure 5.4 (left) an indentation in the surface profile has been highlighted (by a star). This corresponds to the original front of the flow so that the material downstream of this point is from the bed. Unlike the Newtonian experiments, the fluid's non-Newtonian rheology means that this irregularity is not smoothed out during the flow.

This explains why the flow front crosses an entrainable bed faster than a rigid base. The avalanche may not travel faster over this distance, but the front is composed of uplifted material, like a wave whose velocity is faster than the velocities of individual fluid packets.

But if the same avalanche travels over an entrainable bed and a rigid base, why is the front position permanently advanced in the case with entrainment, and why does the quantity of entrainable material matter if the mass released is the same? Figure 5.4 (right) shows a comparison of two images – one from entraining flow 20-6Ca and one from 20-0a which flowed over a rigid base – taken the same amount of time after the avalanche front reaches 90 cm, the start of the entrainable bed when there is one. The avalanche follows the geometry, scouring out the bed material and leading to a concave flow surface above the bed in the case with entrainment. At 95 cm, the difference

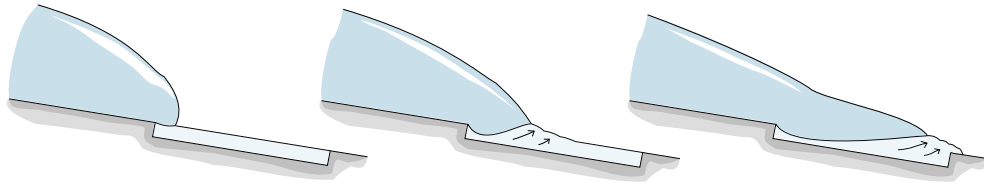


Figure 5.5: Schematic to show the displacement of the bed by the incoming avalanche.

in surface heights is significant, and corresponds to the bed depth. This displaced material travels downstream and contributes to the difference in front positions when entrainment occurs, as illustrated in the schema of figure 5.5. Thus the more loose material available for entrainment, the further downstream the front will travel.

Internal measurements

Entrainment of stationary material led to an increase in flow front position compared to the non-entraining case due to some uplift of bed material by the avalanche. Internal velocity measurements taken from camera 1 during the PIV measurements will give more detail on the exact mechanics of this process, also showing whether entrainment happens in the same way at all slopes considered.

Experiments were performed to visualise and quantify the internal velocities of the flow, specifically concentrating on the zone just downstream of the step, to see how the avalanche interacted with the entrainable material. It should be noted that all measurements were taken in a frame of reference in which the z axis is perpendicular to the slope and the x axis is tangent to the slope. As such, in what follows, “vertical” refers to this z axis and not to the direction of gravity.

As a first step, the raw images (e.g. figure 5.6) were examined, from which an idea of the flow progression can be inferred:

- The flow initially rolls out a short distance onto the bed with only a local effect on the bed material: the bed surface is deformed slightly, moving downwards underneath the avalanche’s front, and forwards just downstream of the front.
- As the flow progresses, a region of significant downwards vertical motion is established next to the step, in a similar way to that seen in the Newtonian experiments.
- The avalanche front continues to drive forwards across the entrainable bed, but remains pronounced with an indentation in the flow surface where it meets the bed.
- The protrusion of the flow into the bed near the step displaces the bed material

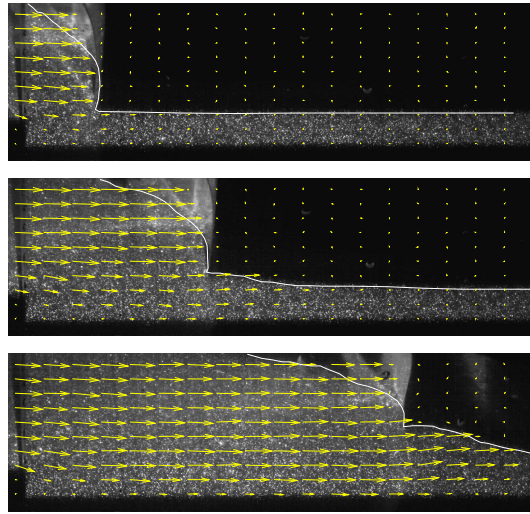


Figure 5.6: Entrainment illustrated using a sequence of raw images and velocity vectors. 6 mm deep by 30 cm long bed at 20° . Surface indicated to exclude refraction effects.

downstream, towards stationary material. As well as causing some forward motion further downstream, this causes significant upward motion just downstream of the flow front. The viscoplastic nature of the fluid means flowing bed material will more readily ride up over stationary material than cause it to overcome its yield stress.

- By this point, the bed surface has been uplifted almost in line with the original flow front, but the indentation here is still visible, and the bed is in motion much further downstream. Much of the flow behind this point is now a plug flowing over a thin shear layer on the rigid base.

Figure 5.7 shows the internal velocity profiles at two different moments in the flow for an entraining dam-break compared to a non-entraining dam-break at slopes 16° and 24° . The velocity profiles have been scaled by 5 and 0.25 respectively for clarity, and averaged over five time-steps. First, considering the non-entraining flows (a, b, e & f), figure 5.7 shows clearly that the shear layer at shallower slopes is much thinner than at steeper slopes. It is also reassuring to see that no slip occurs on the base, showing that the strategy of coating the flume with dry Carbopol was effective in avoiding the wall-depletion problem [62]. However experiments at shallower slopes with an entrainable bed showed some basal slip downstream of the step, but not at the steeper slopes (c, d, g & h). A thought-provoking question is then: if there is no slip in the non-entraining case, and apparent slip in some of the entraining cases, why do the bulk measurements presented in figure 5.3 show little or no slope dependence?

Two possible responses are then: either no slip occurs in any of the entraining flows, but for shallower slopes the shear layer is so thin that it contains no PIV seeds and

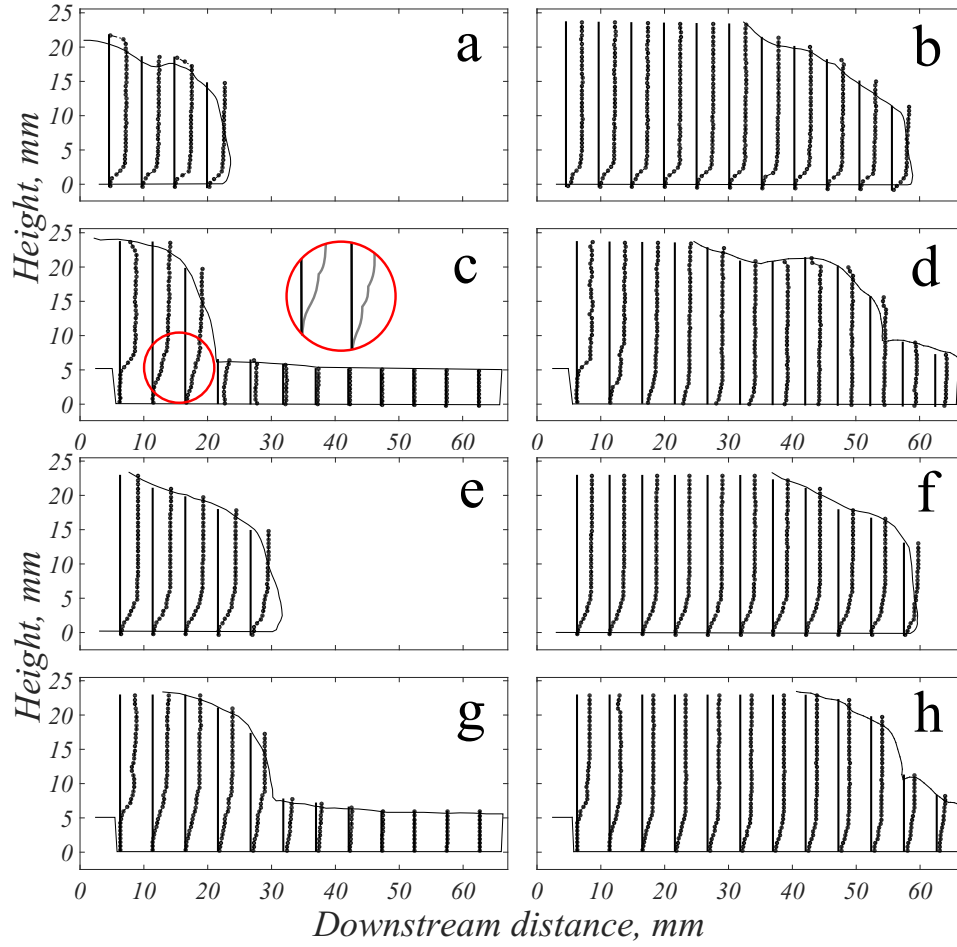


Figure 5.7: a – d: Velocity profiles for 16° slope, $l_{step} = 90$ cm, comparison between entraining (16-6Cb) and non-entraining (16-0b) cases at $t=34$ s and $t=114$ s. e – h: Velocity profiles for 24° slope, comparison between entraining and non-entraining cases at $t=2.25$ s and $t=5.5$ s.

it is not visible in the internal measurements; or the presence of slip has very little influence on the effects of entrainment.

The viscoplastic nature of the fluid used means that how the initially stationary entrainable bed is set into motion by the overriding dam-break is not a trivial question. How is the shear stress transferred down through the entrainable material, and are there differences at different slopes? Imagining a two layer flow, in which the avalanche is the upper layer ($z > 0$) and the bed is the lower layer ($z < 0$), the horizontal shear applied to the bed surface causes motion in the bed. If the shear stress at the interface $z = 0$ is greater than the fluid yield stress $\sigma_{xz}(x, z = 0, t) > \tau_c$ then the yield surface is found in the top layer, whose basal velocity is non-zero. In this case, interesting velocity profiles may appear, such as shown in the inset illustration of figure 5.7 (c). This bumpy velocity profile is more pronounced at the shallower slopes.

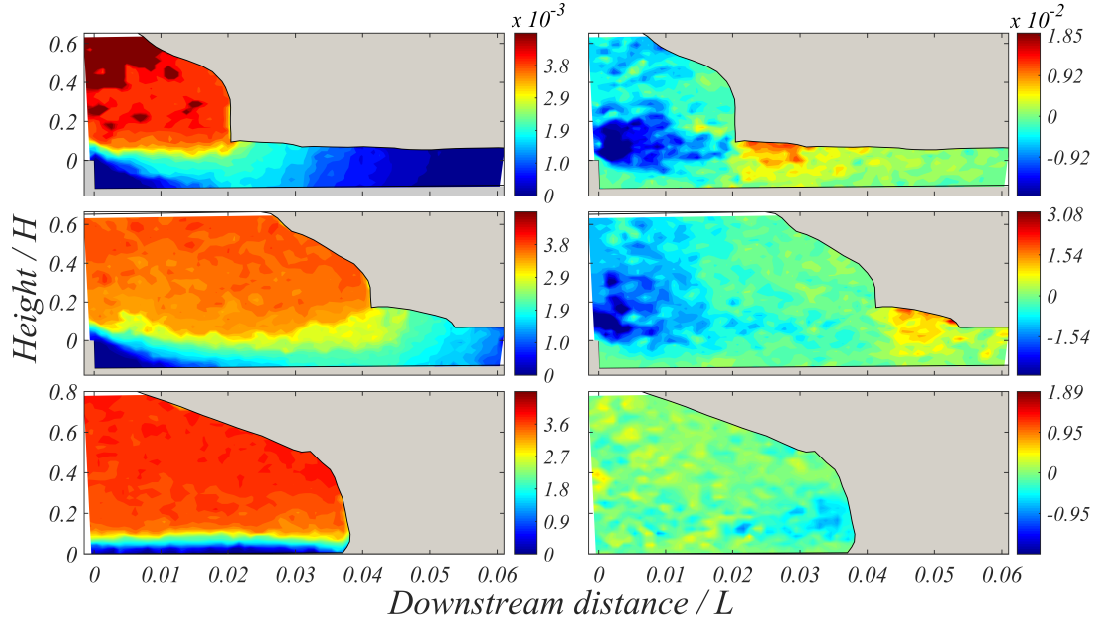


Figure 5.8: Velocity fields for horizontal (L) and vertical (R) velocity components. 16-6Ca: 16° slope, 6 mm deep by 30 cm long bed. Plotted at times 10.5 s (top) and 24 s (middle) after front entry into bed. Velocities and lengths non-dimensionalised. Bottom: equivalent non entraining flow after 24 s.

Finally, comparing an entraining flow to a non entraining flow, the velocity changes in response to entrainment. Bed material below and downstream of the original flow front is set into motion, and as a result the velocities in the overriding avalanche seem to be reduced. This is particularly obvious comparing panels (f) & (h). So with respect to the horizontal velocity, more fluid is set into motion due to entrainment, at a cost to internal avalanche velocities.

Contour plots of the velocity components complete this picture, and are particularly useful for showing regions of pronounced vertical velocities and significant shearing.

Figure 5.8 shows the internal velocity fields for the PIV experiment 16-6Ca at times 10.5 s and 24 s after front entry, and the corresponding non entraining flow at 24 s. Initially there is strong horizontal shear at the surface of the bed, with almost plug flow above and small horizontal velocities in the bed. The flow has strong downwards velocities close to the step, displacing bed material downstream. A bump is beginning to appear in the bed surface just downstream of the original flow front x_F , where strong upwards motion in a triangular region has been induced by the squeezing of bed material between regions of positive horizontal velocity upstream and zero velocity downstream.

Later, this bump has become more pronounced and vertical velocities are stronger,

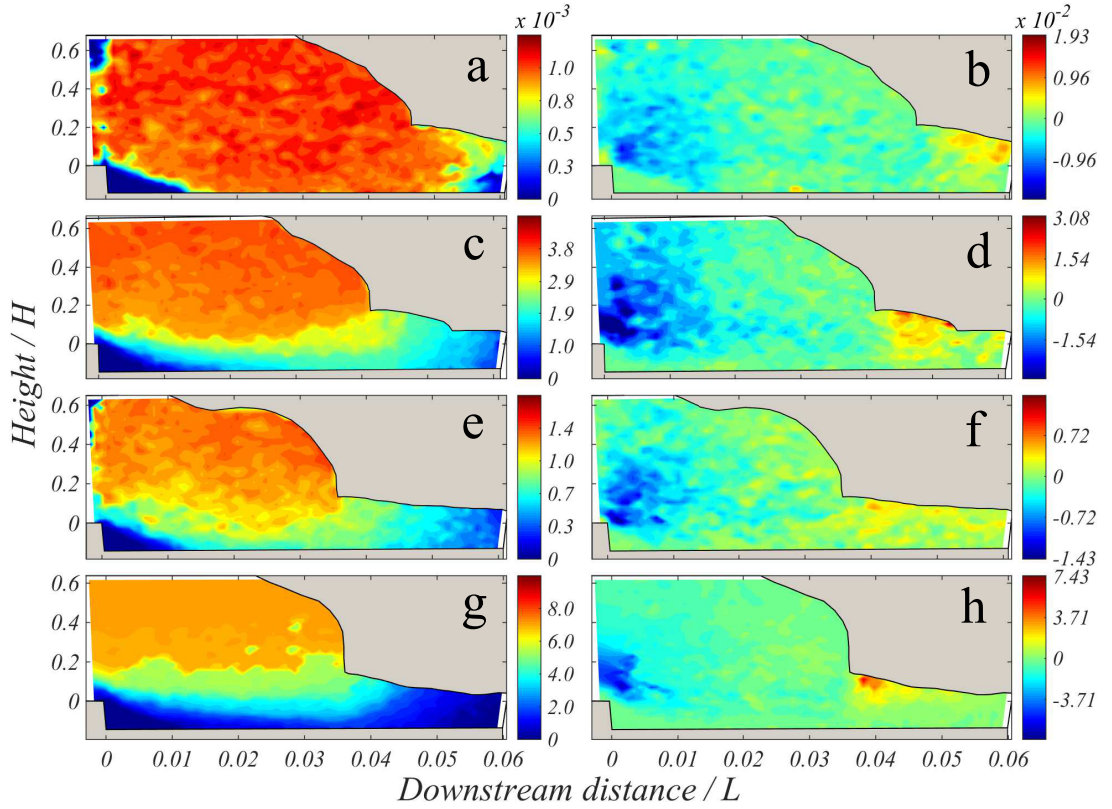


Figure 5.9: Velocity fields for horizontal (L) and vertical (R) velocity components. (a & b) 12-6Ca, 12°, bed at 70 cm, (c & d) 16-6Cc, 16°, bed at 70 cm, (e & f) 16-6Cd, 16°, bed at 90 cm, (g & h) 24-6Ca, 24°, bed at 90 cm.

as if the bed has buckled downstream of the point x_F . Motion occurs right down to the rigid base, and horizontal velocities inside the overriding avalanche have been reduced with respect to the non-entraining avalanche at the corresponding time. The flow front position is much further downstream due to the bed uplift. In this figure, and in figure 5.9, velocities have been non-dimensionalised by their slope-dependent scaling, $U_\theta = (\rho g \sin \theta H^{n+1} / K)^{1/n}$, with H kept constant at 0.03 m and $L = 1$ m, so that they can be compared between slopes.

It would be expected to see differences in the internal velocities due to the slope angle, as the effects of gravity differ. It has already been noted that the scalings suggested by lubrication theory are not sufficient to account for the differences in front position with slope, and the same applies for internal velocities. Figure 5.9 shows velocity profiles at times when their non-entraining equivalents all had matching front positions, found by advancing the same number of time-steps forward from the moment when the front arrives at the step location.

Aside from the magnitude of the velocity, the flows also differ with slope in their

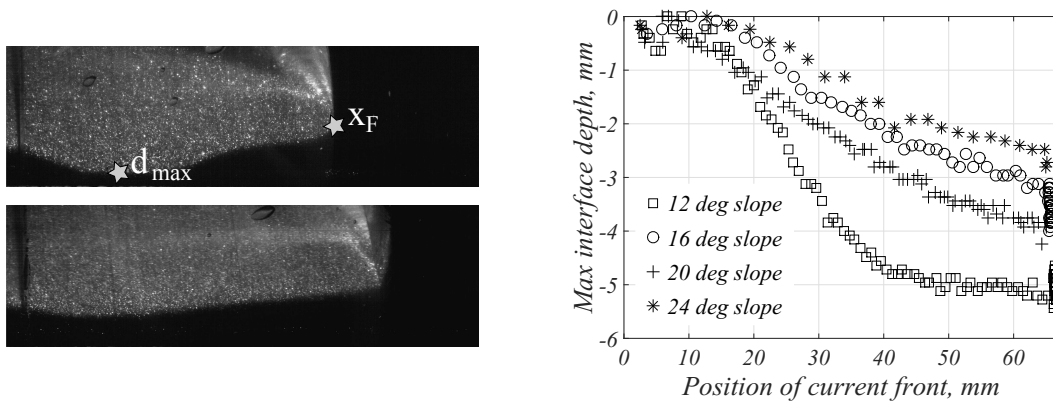


Figure 5.10: L: Raw images showing different interface shapes for 12° and 24° slopes. R: plotting the interface intrusion - maximum downstream point x_F plotted against maximum interface depth d_{max} . N.B. for 12° and 16° the bed was located at $l_{step} = 70$ cm and for 20° and 24° the bed was located at $l_{step} = 90$ cm.

viscoplastic behaviour. At 12° (a) much of the flow is a plug, with a thin region of strong horizontal shear and possibly large amounts of slip on the base, whereas in a similar flow at 16° (c) the shear layer is far thicker. Similarly the bed is more strongly sheared at 24° (g) than at 16° (e), and the region of bed uplift is much smaller (f & h). What appears to happen at shallower slopes is that the dam-break intrudes deeply into the bed, effectively bulldozing downstream material and causing the bed to buckle. This is consistent with a stronger vertical gravity component. At steeper slopes, this bulldozing motion is not seen, instead the bed is strongly sheared and is uplifted only very close to the point x_F .

The differences of flow intrusion into the bed are confirmed by examining the “R” experiments (figure 5.10). Here only the material released from the dam-break was seeded and the bed was unseeded, showing the interface between the flow and the entrainable bed as it deforms. The avalanche intrudes more deeply into the bed for shallower slopes. This is perhaps intuitive, as on a steeper slope the downslope component of gravity becomes more important and the component directed into the slope has less effect. In figure 5.10 the maximum depth of the interface, d_{max} is plotted against the maximum downstream extent of the overriding avalanche, x_F , showing this difference clearly. At shallower slopes the avalanche intrudes more deeply, and the same happens when the entrainable bed is further downstream (thus reducing the velocity of the overriding flow). Here the beginning of the bed is located at $x = 0.7$ m for slopes 12° and 16° , and at $x = 0.9$ m for 20° and 24° .

Even though there are seemingly important differences in the internal mechanics of flows entraining material at different slopes, this has no obvious difference on bulk measurements when considering the front advancement, i.e. the distance gained by the front due to entrainment, when compared to the non-entraining case (figure 5.3).

In the following sections a model is derived and then compared to these observations, which will help to explain this behaviour.

5.2 A model for entrainment by viscoplastic gravity-driven flows

The slopes considered range from small to moderate meaning that there may be significant contributions from gravitational forces. The height of the flow is again much smaller than its length. Thus a model similar to (3.18) has been developed in the case where the flow entrains loose material. As in the previous chapter on viscous flows, the entrainable layer fills a shallow cavity lying in the flow path of the avalanche. The initial condition comes from solving equation (3.18) numerically with *pdepe* for the height profile when the front has reached the beginning of the entrainable bed.

The aim is to obtain a model for the entire flow domain in order to simulate the avalanche's effect on the initially stationary bed, and to study the subsequent flow. Experiments showed that, however locally, the bed was instantaneously affected by the dam-break passing over the top surface, suggesting that the yield stress was immediately breached by the overriding flow. This can also be shown mathematically.

Duffy et al [157] studied a modified Rayleigh problem where the lower half plane was filled with a generalised Newtonian fluid and an infinite plate was placed on its surface at $z = 0$. Following their analysis, the time scale for the setting into motion of the bed can be found. In this case, the acceleration term should be kept but there is no pressure gradient in x , thus the equations to solve are

$$\begin{aligned} u_x + w_z &= 0 \\ \rho \frac{\partial u}{\partial t} &= \rho g \sin \theta + \frac{\partial \sigma_{xz}}{\partial z} \\ 0 &= -\rho g \cos \theta - \frac{\partial p}{\partial z}. \end{aligned} \tag{5.1}$$

The time-scale required for all three terms to balance in the x -momentum equation is

$$T_c = \left(\frac{\rho g^{n-1} \sin \theta^{n-1} H^{n+1}}{K} \right)^{1/n},$$

which is always $\ll 1$ when the height scale H is small. This would imply that the timescale for the transmission of stress into the bed is very quick, almost instantaneous, and it is possible to suppose that the velocity is continuous between the overriding avalanche and the bed from the outset. The experimental results agree: there is no evidence for shocks with discontinuous velocities.

To proceed, the set of equations (3.3) has been solved in the same way as in chapter

3 – with tangential shear stress given by (3.11) – but for one crucial difference. The zero velocity boundary condition on $z = 0$ is replaced by a condition on an arbitrary base function $b(x) \leq 0$ which represents the rigid bottom of the geometry. The stepped geometry used in the experiments can be approximated using hyperbolic tangents, thus removing the corner singularities of the steps, exactly as in section 4.3.

Applying the no slip boundary condition $u_S(x, z = b(x), t) = 0$ on the surface $b(x)$ and solving (3.12) gives an equation for the velocity below the yield surface, in the shear layer. The yield surface is now defined as $Y(x, t) = \max(h - h_c/|1 - \cot \theta \partial h / \partial x|, b(x))$.

$$u_S(x, z, t) = \frac{n}{n+1} A (1 - Sh_x)^{\frac{1}{n}} \left[(Y(x, t) - b(x))^{\frac{n+1}{n}} - (Y(x, t) - z)^{\frac{n+1}{n}} \right], \quad (5.2)$$

u_P describes the plug flow above the yield surface and is defined to first order as constant with z , thus $u_P(x, t) = u_S(x, z = Y(x, t), t)$

$$u_P(x, t) = \frac{n}{n+1} A (1 - Sh_x)^{\frac{1}{n}} \left[(Y(x, t) - b(x))^{\frac{n+1}{n}} \right], \quad (5.3)$$

with $S = \cot \theta$ and $A = (\rho g \sin \theta / K)^{1/n}$.

Then the mass conservation equation is used to obtain expressions for $\partial w_S / \partial z$ and $\partial w_P / \partial z$. These can be integrated with the no-normal velocity condition $\mathbf{u} \cdot \mathbf{n} = 0$ fixing the constant of integration below the yield surface, and the continuity of the velocity across the yield surface fixing the constant in the pseudo-plug region.

Thus:

$$\begin{aligned} w_S(x, z, t) &= \frac{Sh_{xx}}{n+1} (1 - Sh_x)^{1/n-1} A \left[\frac{n}{2n+1} \left((Y - z)^{2+1/n} - (Y - b)^{2+1/n} \right) \right. \\ &\quad \left. + (Y - b)^{1+1/n} (z - b) \right] - (1 - Sh_x)^{1/n} A \left[(Y_x - b_x)(Y - b)^{1/n} (z - b) \right. \\ &\quad \left. + \frac{nY_x}{n+1} \left((Y - z)^{1+1/n} - (Y - b)^{1+1/n} \right) \right], \\ w_P(x, z, t) &= \frac{Sh_{xx}}{n+1} (1 - Sh_x)^{1/n-1} A \left[(Y - b)^{1+1/n} (z - b) - \frac{n(Y - b)^{2+1/n}}{2n+1} \right] \\ &\quad - (1 - Sh_x)^{1/n} A \left[(Y_x - b_x)(Y - b)^{1/n} (z - b) - \frac{nY_x(Y - b)^{1+1/n}}{n+1} \right] \end{aligned} \quad (5.4)$$

Finally, equations (5.2), (5.3) and (5.4) may be linked by solving for the kinematic boundary condition on the surface $z = h(x, t)$ so that

$$h_t + u_P h_x = w_P,$$

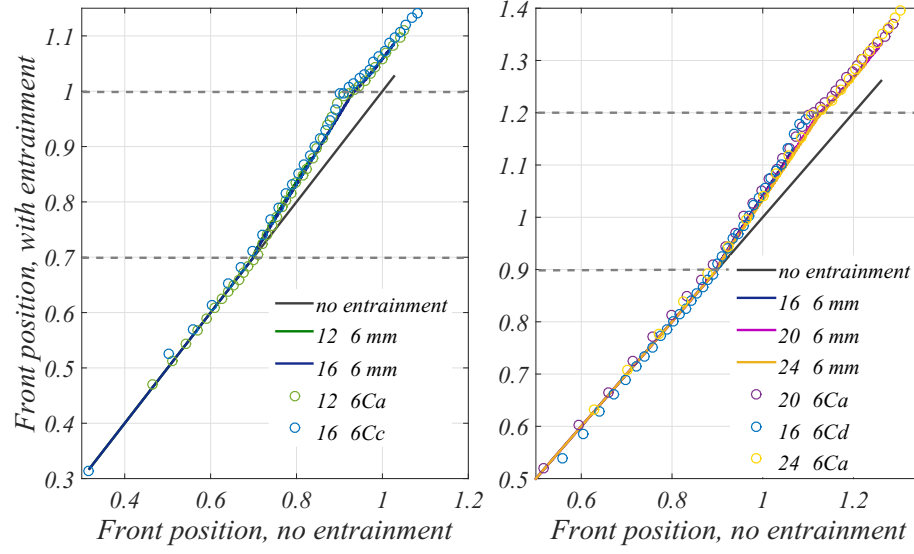


Figure 5.11: A reproduction of figure 5.3 (c & d), showing the numerical solution overlaid by experimental observations.

giving

$$\frac{\partial h}{\partial t} = -\frac{An}{(1+n)(1+2n)} \frac{\partial}{\partial x} (\mathcal{F}(h)), \quad (5.5)$$

$$\mathcal{F}(h) = (Y-b)^{1+1/n} \left| 1 - S \frac{\partial h}{\partial x} \right|^{1/n} \text{sign} \left(1 - S \frac{\partial h}{\partial x} \right) [(2n+1)h - nY - (n+1)b].$$

This equation has the form of a parabolic partial differential equation and as such may be solved using the inbuilt MatLab solver *pdepe*. In this way we may compare theoretical predictions with the measurements taken in the laboratory.

5.3 Numerical solution

Various theoretical approximations to gravity-driven flows were tested by Ancey & Cochard [117]. They found that the lubrication model for non entraining flows performed qualitatively well, but that front positions were overestimated due to an overestimation of initial acceleration. For this reason, the model will not be compared to absolute experimental results, but used to examine the effect of entrainment, for example by reproducing figure 5.3.

The parabolic solver *pdepe* in MatLab [155] was again used to solve the problem (5.5) in order to make a comparison with the experimental results. The grid size was $dx = 10^{-3}$, and the time-steps were exponentially increasing to save computing time while still

guaranteeing accuracy at the early stages of flow when velocities and gradients were strong.

The problem was solved in two steps: first equation (3.18) was solved until the front arrived at $x = l_{step}$, in this case the time evolution was designated as $t = \exp[b \times (no_T - 1)] - 1$, where no_T was the number of time-steps required (either 10 000 or 20 000) and $b = \log(t_F + 1)/(no_T(end) - 1)$, where t_F is specified by the user as an upper limit for the time. The value for h at the moment where $x_F = l_{step}$, defined as the furthest downstream point where $h(x_F, t) > 0$ is then used as the initial condition for the second step: entrainment.

In this step, the new evolution equation for h , (5.5) is solved on a domain including a layer of fluid lying between $z = b(x) \leq 0$ and $z = 0$. At $x = l_{step}$ the base function $b(x) = \delta h/2 \tanh(-100 \times l_{bed}) \approx -\delta h/2$ and so any problem that would have been posed by the flow contacting the bed for the first time has been removed. Contact is already established and the bed and flow are connected. The time evolution continues in exactly the same way as in the solution for the initial condition, thus allowing large steps at later times when the flow moves more slowly.

Figure 5.11 shows that when comparing the entraining flow to its corresponding non-entraining flow, the effect of entrainment on the front position is well reproduced at all slopes. Thus, even though the original model was shown to be inaccurate at simulating non-entraining flows, it was successfully adapted to model the effects of entrainment.

The experiments showed that entrainment effects can be quantified by looking at the advancement of the front position. From the numerics the following can be inferred: the rate of front advancement (i.e. the distance gained due to entrainment) over the entrainable bed, the relative importance of bed depth, bed length and bed position, and their effects on the surface height and front position.

Solving the problem numerically with the rheology as defined in section 2.3, the velocities of the avalanche are greatly reduced compared to the experiments. The problem was solved for different rheological parameters as a basic sensitivity test, and it was found that τ_c had the most significant effect on the flow velocities. So if there is uncertainty surrounding the value of τ_c , this could explain the discrepancy between the numerical results and the experiments: the elevation of the yield surface $Y(x, t)$ depends linearly on τ_c and if Y is higher then the flow is faster. However, figure 5.11 shows that rheological uncertainties have no effect when comparing the entraining case to the non-entraining case, and so in the mechanism of entrainment alone, the yield stress τ_c seems not to play a role.

A further comment about this discrepancy concerns lateral surface height variations. The model produces a 2-D flow originating from a dam-break where the initial volume has been divided by the flow width. In reality as the flow develops, its surface becomes

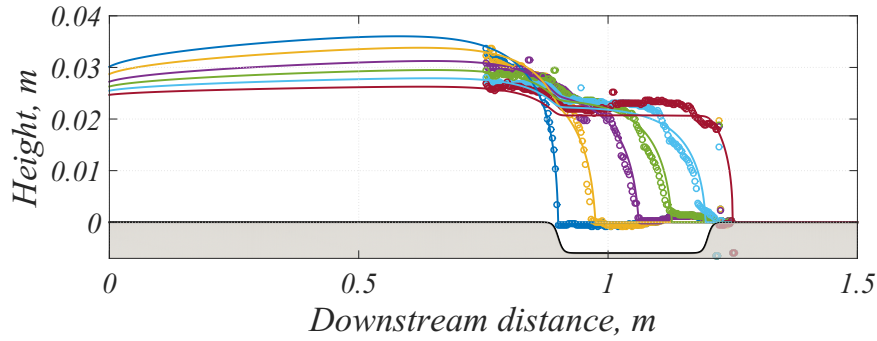


Figure 5.12: Comparison of surface height profiles for front travelling over entrainable bed, 6 mm-deep at 20° . For qualitative comparison only – times do not correspond. Experiment 20-6Ca.

slightly curved, with a maximum at the flume centre and a minimum at each wall, which is especially pronounced near the flow front. This would imply that more material is involved in the dam break at the centre than at the sides, contrary to the assumption of constant volume per unit width in the model, and this may also help explain the observed difference.

Finally, the model took only the first order terms into account. Inertial terms were dropped from the governing equations. Even though inertia is clearly second order here, it may still have a small effect on the flow, and thus its absence in the model may be the most likely explanation for the slowness of the numerical results compared to the experiments. For example, at 16° , $Re \approx 1.8$ for $H = 0.03$ m so that inertial terms, although small, may have some effect.

In any case, the shape of the flow is qualitatively well reproduced, with a hollowed out surface above the entrainable bed, and a stronger upstream effect the larger the bed (in both dimensions). Figure 5.12 shows an example of this qualitative agreement: the essential characteristics are captured. There is a large kink in the surface near the step, the surface height upstream of $x = l_{step}$ decreases in agreement with the modelled profile, and the front shape is quite well reproduced, although the times at which the experimental surfaces are plotted do not correspond to those for the model. There are also some local errors but these could partly be due to measurement inaccuracies.

Figure 5.13 shows how the flow follows the geometry, highlighting the effects of different slopes. The yield surface is shown as a dashed line and it is clear that at steeper slopes the shear layer is deeper, as found in the experiments. The same flows are modelled over bed depths of 3 and 6 mm, showing clearly the surface height response to a deeper entrainable layer. When the bed is deeper, the avalanche is able to scour to a deeper level, which is evident in the more pronounced surface features around the

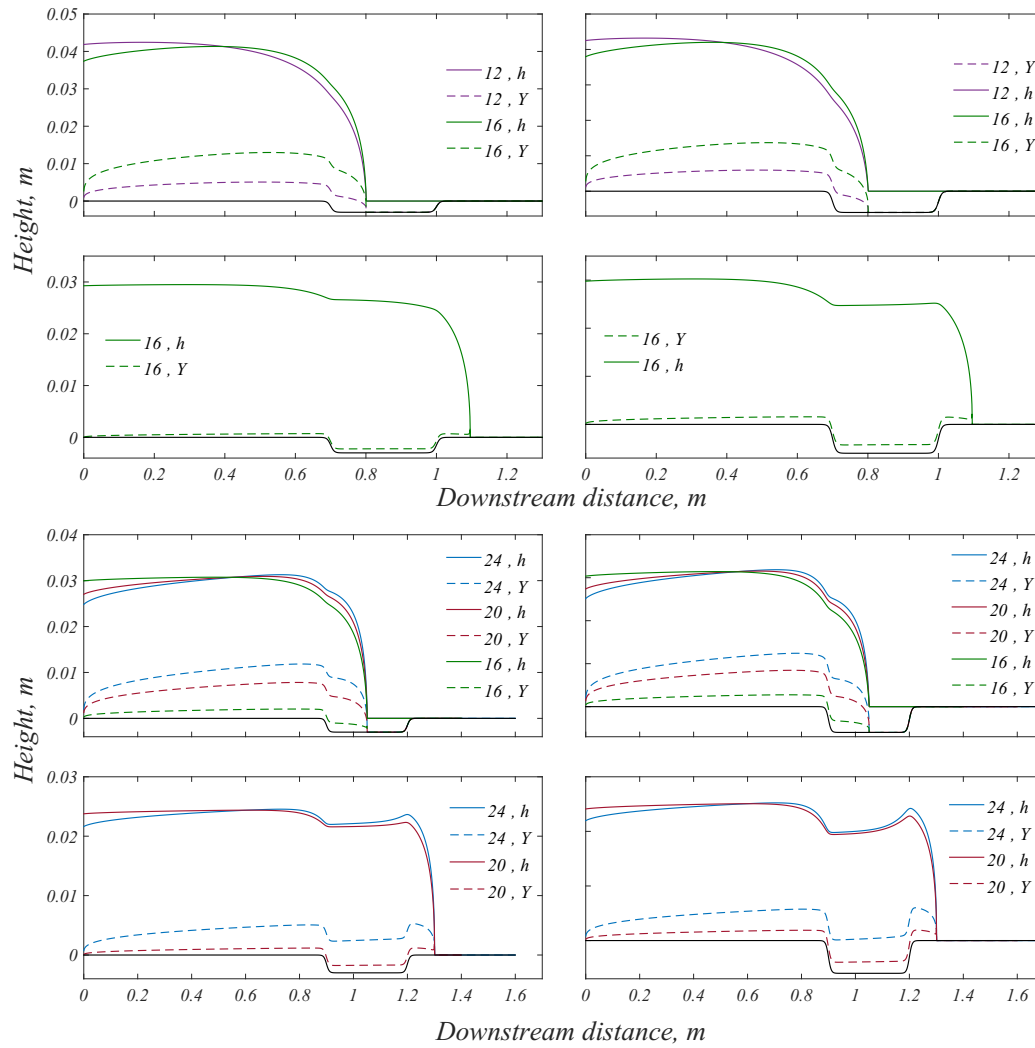


Figure 5.13: Comparison of surface height profiles (solid line) and yield surfaces (dashed line) for flows travelling over entrainable beds 3 (L) and 6 mm-deep (R). From top to bottom: flow front at 90 cm, bed at 70 cm for 12° and 16°; flow front at 110 cm, bed at 70 cm for 16°; flow front at 105 cm, bed at 90 cm for 16°, 20° and 24°; flow front at 130 cm, bed at 90 cm for 20° and 24°.

entrainable bed. Equally, the surface height differences due to slope – such as a steeper flow front at higher slopes – lead to more exaggerated effects on the flow surface as shown by the bottom two panels.

Finally, the internal velocities can be calculated by solving equations (5.2), (5.3) and (5.4). Figure 5.14 gives an idea of what the internal velocity profile resembles for a flow at 20° entraining a 6 mm-deep by 30 cm-long bed. Exactly as in the experiments, a significant part of the flow front experiences upwards motion as the bed material is forced upwards. The velocities can be compared roughly to values found in PIV

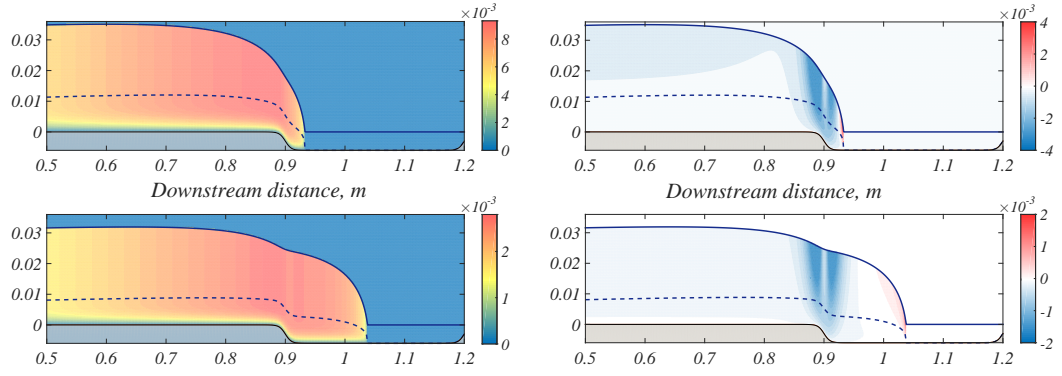


Figure 5.14: A sample of modelled velocity fields for experiment 20-6Ca.

experiments for the top case, $x_N = 0.934$ m. The observed horizontal velocities ranged from 0 to around $2.2 \times 10^{-3} \text{ m s}^{-1}$, compared with around $8 \times 10^{-3} \text{ m s}^{-1}$ in the numerics. However the observed vertical velocities ranged from around $-4.5 \times 10^{-3} \text{ m s}^{-1}$ to $2 \times 10^{-3} \text{ m s}^{-1}$, similar to those predicted by the model.

Simulations were run at 20° inclination to investigate the effects of entrainable bed geometry on the flow, specifically looking at the advancement of front position compared to a non-entraining flow $\Delta X_i(t) = x_{N,i}(t) - x_{N,0}(t)$. The results are shown in figure 5.15. The simulations were run for 70 000 time steps ($O(10^9)$ s) and behaviour that seemed asymptotic in e.g. figure 5.11 was found not to be so, although the time-scale over which it changes is very long.

In the top left panel, the bed depth is varied and its length remains constant at 30 cm. When the front reaches the end of the 9 mm deep bed – at 1.2 m – it is 10.6 cm further downstream than the non-entraining flow front. Then as it leaves the entrainable bed it slows down temporarily, but ΔX_i continues to increase afterwards, instead of reaching an asymptote, as shown in the middle panels. These local maxima of ΔX_i , corresponding to $x_{N,i}(t) = 1.2$ m, are $\{1.4, 2.7, 3.9, 5.1, 6.3, 7.4, 8.5, 9.6, 10.6\}$ cm, for bed depths of 1 mm up to 9 mm deep.

When the bed is 30 cm long, $\Delta X_i(i)$ is related to $x_{N,0}(t)$ approximately linearly, apart from the initial moments. The top right panel shows, however, that this approximation is no longer adequate for a 50 cm long bed.

Further investigation into the effects of slope in the numerical results show something that was not clear from the experimental results - slope does indeed have an effect on front advancement but only a small one. The difference in front position ΔX_i is actually greater for a shallower slope, but only by a few millimeters. For example, when the non-entraining flow front is at 1.05 m, at 24° its corresponding entraining flow front is 48 mm further downstream, for 20° this value is 52 mm and for 16° this increases

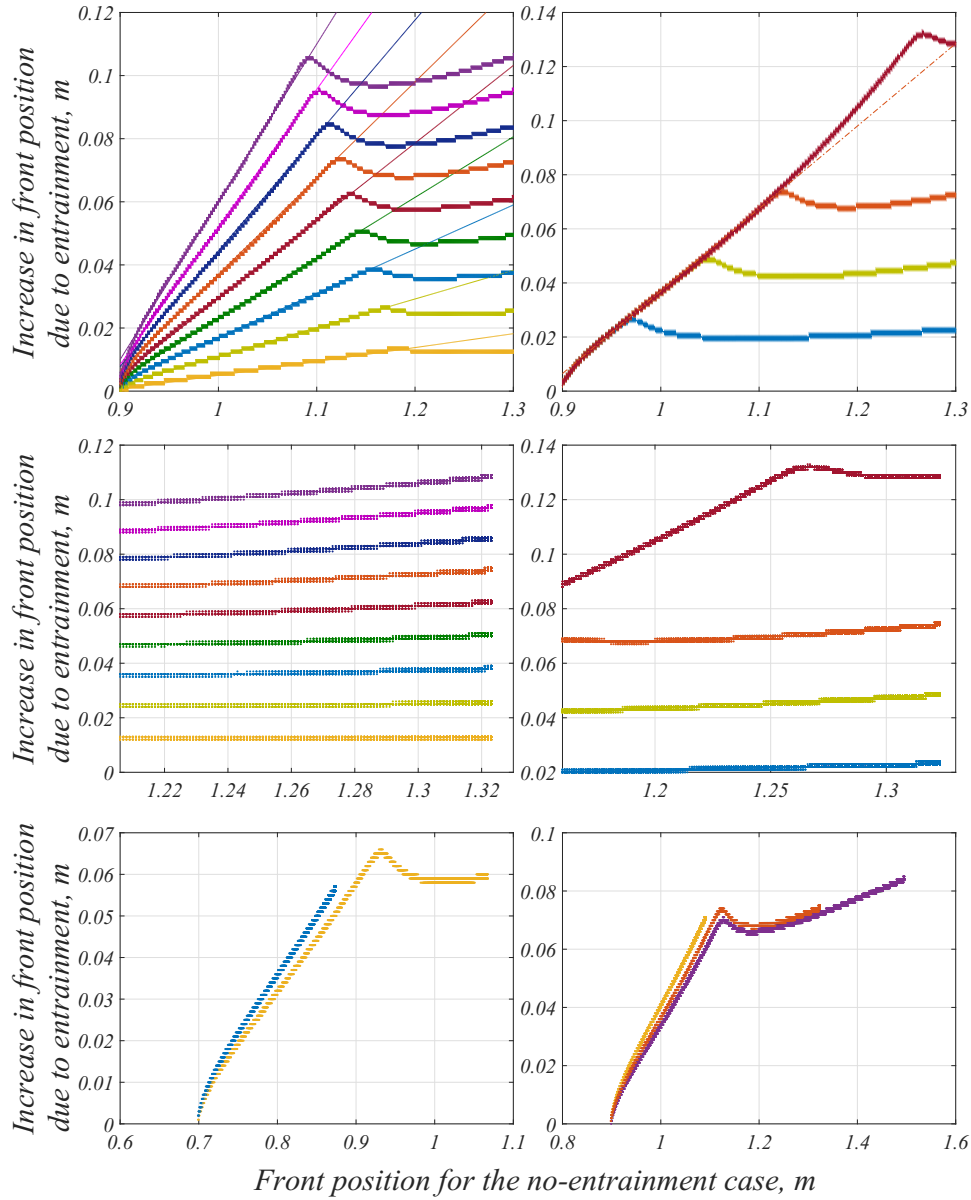


Figure 5.15: Difference in front position between entraining and non-entraining flows $\Delta X_i(t) = x_{N,i}(t) - x_{N,0}(t)$. Top: 20°, different bed depths (1-9 mm) and bed lengths (10, 20, 30 or 50 cm); Middle: 20°, different bed depths and bed lengths – later time; Bottom: different slopes: 12° and 16° with $l_{step} = 70$ cm, 16°, 20° and 24° with $l_{step} = 90$ cm.

to 57 mm. When the front flows over a rigid base once again, this difference becomes even smaller.

This slight difference due to slope inclination is reassuring. It would have perhaps been paradoxical that differences in bed excavation were seen in figures 5.9 and 5.10 yet this had no effect at all on the bulk flow. Further, this is consistent with the fact that the bed is scoured out faster at shallower slopes than at steeper slopes, as would be expected due to the relative strengths of the perpendicular and downslope components of gravity. In this way more bed fluid is pushed downstream at shallower slopes than at steeper slopes. The bottom panels illustrate this: the increase at 12° (blue) was more than for 16° and the increase at 16° (yellow) was more than 20° (orange) or 24° (purple).

5.4 Discussion

In this chapter it has been found that when a viscoplastic avalanche travels down a slope and entrains identical stationary material, its front propagates downstream faster than if there was no material to entrain, due to the uplift of bed material contributing to the flow front. Testing flows at slope inclinations of 12° to 24° showed that slope played a negligible role and the graphs of figure 5.3 – which compare the front position in entraining flows to its non-entraining equivalent – appear to collapse onto the same curve. Not only the length of the entrainable layer, but also its depth had clear effects on the front position.

Internal measurements showed that the bed was quickly accelerated from rest and began to deform as the avalanche flowed down the step. Downstream material was forced upwards, thus advancing the flow front, defined as the furthest downstream point of positive surface height. Surface measurements showed that the avalanche followed the shape of the geometry closely, hollowing out the region containing entrainable material. This hollowing out happened differently for different slopes: at 12° the avalanche dug quickly down behind the step, excavating the bed faster than at 24° , which is consistent with the direction of gravity relative to the slope.

A model was developed following the lubrication theory discussed in section 3.2, due to the success of the Newtonian entrainment model developed in section 4.2. It was difficult to find quantitative agreement between the modelled flow parameters and their experimental equivalents perhaps due to the lack of inertia in the model.

The model's success in describing entrainment is evident in figure 5.11. Because the model performed qualitatively well in both entraining and non-entraining flows, I decided to compare the front positions in each case. Here, the model performs excellently, showing that even if the flow itself is not accurately described, the effects

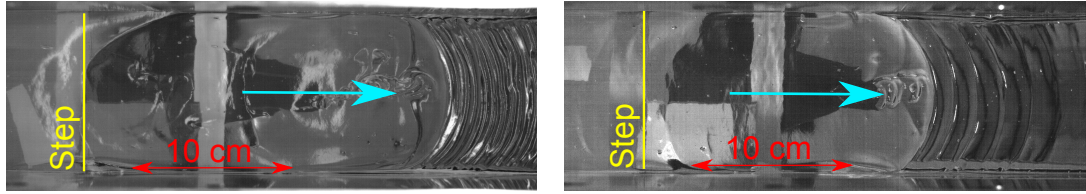


Figure 5.16: Bed buckling on a 12° slope, L: 3 mm deep bed. R: 6 mm deep bed.

of entrainment are. In a way, the errors in a non-entraining flow are balanced by those in an entraining flow.

Two questions arose, which are beyond the scope of this thesis, but could be interesting problems. These are described below.

Buckling

In many of the experiments the bed was significantly buckled downstream, especially at shallower slopes like in figure 5.16. This was particularly obvious when the bed did not contain blue dye. The buckling led to a regular series of bumps whose wavelength was longer for a deeper bed, as in figure 5.16. The model derived above makes the long wave assumption that variable changes in the x direction are gentle compared to the z direction, and thus does not capture this behaviour. Figure 5.8 shows that these bumps develop due to the local squeezing of fluid, between moving upstream fluid and stationary downstream fluid. It is beyond the scope of this work, but it could be interesting to see if the kind of bulldozing problem described by Bagnold [158] and Sauret et al [159] could be applicable to this problem, particularly given that in the latter study some interesting effects were observed due to slip.

Non-identical flow/bed

As described in table 2.2, the experiments designed to give bulk measurements were often performed in two configurations. In one configuration the bed was composed of dyed Carbopol (denoted c for combined), and in the other it was composed of clear Carbopol (denoted r for reservoir-only). The r experiments were not used in the above analysis, but offered some interesting complementary information. On one hand they were useful to see that slip was indeed minimised: when the flow exited the entrainable bed its front was made up of clear fluid, but rapidly this clear layer was overtopped by blue fluid as would be expected in a flow obeying the no-slip condition on its base.

These flows were analysed in the same way to find their flow front speed, which seemed to be slower than the c runs in most cases. This suggests that there was some sort of difference between the blue stained Carbopol and the un-dyed Carbopol, which may

affect the results. Considering that in nature avalanches and debris flows rarely entrain identical material (e.g. [160]), investigating how to adapt this model to an avalanche flowing over a non-identical bed would be a worthwhile extension of this work.

Entrainment by Granular Suspensions

In this section, the experimental techniques applied successfully in chapters 4 and 5 are tested for granular suspensions and an exploratory experimental campaign is carried out. A noteworthy problem encountered involved the reproducibility of the experiments. Each time an experiment was performed, a small amount of the fluid drained away underneath the steps, and was left on the flume afterwards. A sufficiently large amount of suspension was prepared so that this fluid loss had minimal effect on the suspension composition, however over time the suspension became slightly more concentrated. As such, each experiment is slightly different and a full comparison of the data may not be possible.

For this reason, the analysis of the data in this section remains qualitative, and this study represents an exploration of the mechanisms involved without placing too much importance on quantitative details. The technique requires some improvements before full quantitative measurements are possible but these early results are promising and there is great potential for a more detailed study which is recommended as a continuation of this thesis.

6.1 Experimental results

Three example images are shown in figure 6.1 from different runs. The top image is from run 12-6b and shows a 3.8 kg mass which flows over a 6 mm-deep entrainable bed at 12° . The middle image is from run 12-3b and shows a 3.25 kg mass flowing over a 3 mm-deep bed at 12° . The bottom image shows a 3.8 kg mass entraining a 3 mm-deep bed at a slope of 16° . The image quality is the best at the base, as the camera films from below. The quality deteriorates towards the surface due to bubbles in the flow entrained by the front, slight differences of refractive index between fluid and particles, and because some of the beads were not transparent. Despite this, most images are of a sufficiently good quality to use in PIV, and for other image analysis. An unexpected

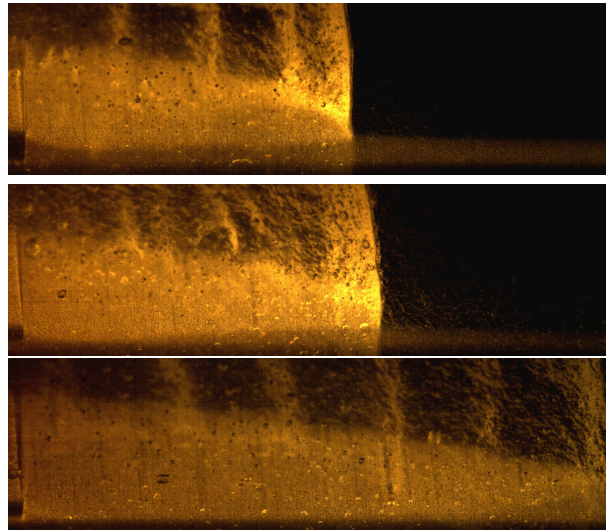


Figure 6.1: Raw images from Camera 1. Top: 3.8 kg released on a slope of 12° , 6 mm-deep bed. Middle: 3.25 kg released on a slope of 12° , 3 mm-deep bed. Bottom: 3.8 kg released on a slope of 16° , 3 mm-deep bed

result was that the rhodamine in the bed was gradually depleted by the laser, so that the incoming flow glowed more brightly upon arrival, showing the interface between the avalanche and the bed material, which was similar in shape to that seen in the viscoplastic experiments. This also means that in the time-space images the moment of front arrival is observable, by the bright line in figure 6.4.

In all cases, the progression was as follows:

- The avalanche moves out onto the surface of the entrainable layer with no initial effect.
- The flow sinks very slightly into the bed, the front skimming some top layers of beads from the bed surface, disturbance is local.
- After the avalanche travels some distance over the entrainable bed, massive failure occurs and material downstream of the front is ploughed downstream in an apparent plug flow. Near the step, the avalanche entrains the bed material progressively - the suspension flows into the bed replacing the material that has been advected downstream.

The bed material began to slip on the rigid base, around 5 cm downstream of the step. The flow was a mixture of shear flow (near the step) and plug flow regions (further downstream).

PIV can be performed on the images obtained, so long as they are not too blurred or

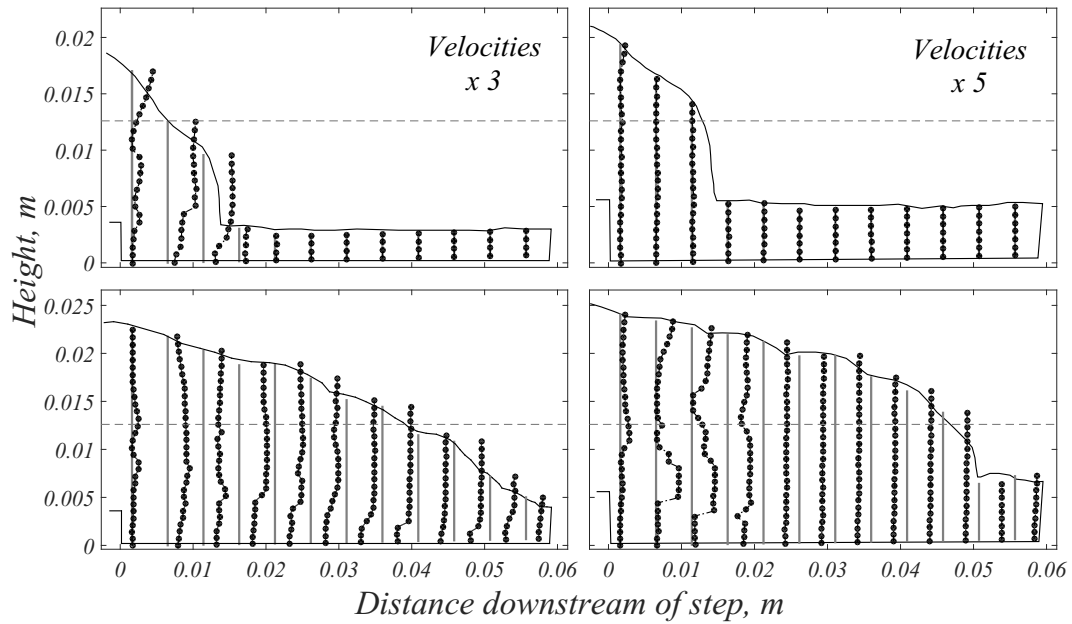


Figure 6.2: Velocity profiles. L: Run 16-3b, at times (im 320 and 1020) R: Run 16-6a, at times (im 420 and 1500). In all images the dotted grey line shows a limit above which the image is significantly blurred. Velocities averaged over 5 timesteps.

contain too many bubbles. This study is concerned with the entrainment of a basal layer, and in this region the images are the clearest, as camera 1 filmed from below. Not all of the experiments produced satisfactory results and so only a couple of runs will be used as examples.

Analysing the velocity fields in the experiments performed showed that the depth of the bed had a different effect from that seen before, illustrated in figure 6.2. Velocities in experiment 16-3b, which has a 3 mm-deep bed, are greater than in experiment 16-6a which has a 6 mm-deep bed. The initial phase in which the flow rolled out over the bed with little or no effect lasted much longer when the bed was deeper, as if the bed was braking the avalanche's flow. In the top panels, the front is at the same position, but the 3 mm bed has already yielded in contrast to the 6 mm-deep bed. Later, both beds have yielded and slip occurs in both cases. Interestingly the flow moves as a single plug in experiment 16-6a, but there is some shear in experiment 16-3b. Finally, there is a significant unyielded corner of flow next to the step in experiment 16-6a, which is smaller in experiment 16-3b.

This all suggests that a deeper bed initially provides greater resistance to entrainment. Shear stress is exerted on the rough surface by the flow which is transmitted downwards through the suspension which eventually gives and slips over the base. The smaller shear stress required to entrain the 3 mm-deep bed seems not to cause as much basal

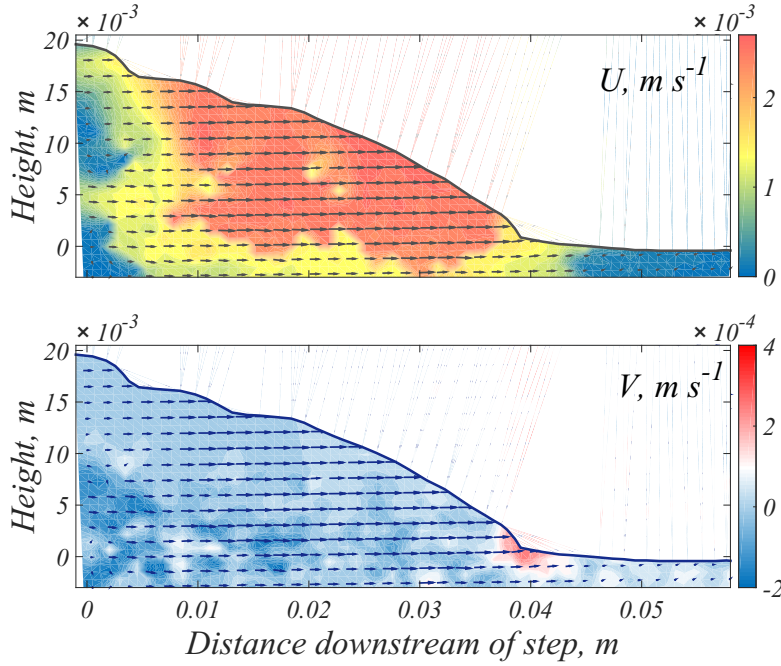


Figure 6.3: Images converted to velocity field using PIV. Experiment 16-3b.

slip, and some internal shear is possible.

In figure 6.3, the velocity fields at $t = t_e + 12.8$ s (image 750) are shown for experiment 16-3b. Upwards motion is seen at the flow front, and some downstream material is displaced. This upwards motion is more localised than in the viscoplastic experiments.

In figure 6.4 time-space plots are created by sampling a line of streamwise pixels at regular intervals, and repeating it vertically. In the top image, images from camera 2 are used during the flow 12-3a. The front of the avalanche arrives from the left hand side, and enters the entrainable zone as shown. The rough surface of the suspension in the entrainable bed means that it reflects light irregularly so that the motion of the bed surface can be tracked by studying trajectories of surface particles. In figure 6.4 this can be seen as streaks of light and dark which begin straight and slightly diagonal, and begin to curve as the front arrives and pushes the suspension downstream.

These lines are diagonal because the entrainable material is gradually moving downstream before the front arrives, either under gravity or as an initial effect of the front entering the bed (implying that either no yield stress exists or it has already been breached). Then as the front approaches, the material just downstream is pushed upwards and entrained into the flow, as shown by the curved trajectory and the addition of material to the flow front.

In the lower images, images are taken from camera 1, filming the flow internally. In the

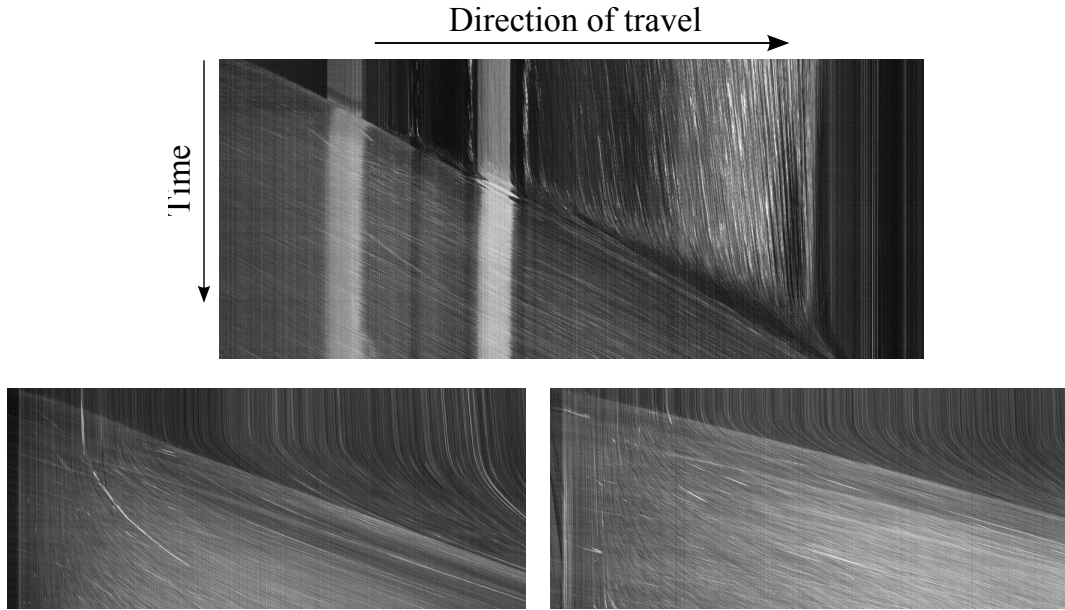


Figure 6.4: Front progression during entrainment. The entrainable bed begins on the left and is 30 cm long. Top: Bird's eye view: The three dark lines show three of the pressure sensors, at 3.5, 7 and 10.5 cm from the beginning of the bed. Bottom: Time-space images from camera 1 show a line of pixels in the entrainable bed, for experiments 12-6c (L) and 16-6a (R).

same way, a line of pixels is sampled from the bed regularly (here each 0.06 s, or every third image), and these lines are put together to create a time-space plot. The position of the original flow front is shown by the line separating the bright and dark sectors.

The left hand image shows flow 12-6c, where 3.8 kg of suspension was released at 12° over a 6 mm-deep bed and the right hand image shows a similar experiment 16-6a at 16° . In both images, pixels are sampled from the same depth in the bed, because surface particles were entrained more quickly than deeper particles. As would be expected, the front travels faster at 16° and material is therefore entrained earlier. Other comparisons are difficult to make, as information about the exact composition of the bed is not available. It seemed as if fluid drained more quickly from the bed at 16° .

Between experiments 16-6a and 16-6b, the flume was not properly cleaned upstream leading to some interesting results for campaign 16-6b. As the plastic steps were just inserts placed in the flume, there was a narrow gap down each side. This did not have a visible effect in the two previous experimental campaigns for viscous and viscoplastic fluids, however in this campaign some fluid separated from the suspension and leaked into these gaps. As experiment 16-6b was being set up, this fluid ran downstream, and entered the entrainable bed, making a dilute area just next to the step. Then, when the

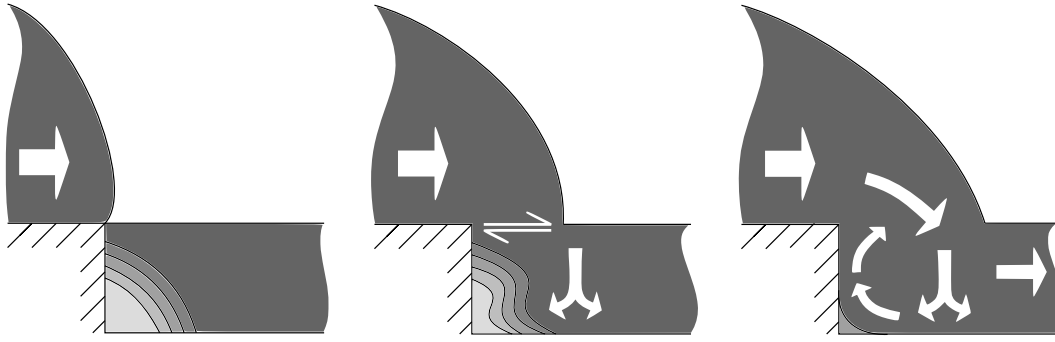


Figure 6.5: Schema showing a recirculation zone being set up due to a concentration difference in the bed. Lighter = less concentrated.

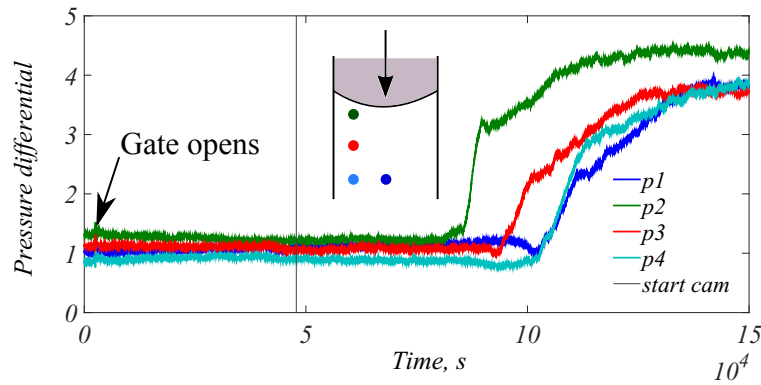


Figure 6.6: Differential pressure sensor signals, showing arrival of the front.

avalanche began to flow over the entrainable bed, large shear stresses were exerted on the bed surface. Previous studies (e.g. [124, 134, 147]) have shown that particles migrate from regions of high to low stress, and so some beads began to flow upstream into the dilute zone, thus setting up a recirculation zone where some beads moved upwards next to the step only to be entrained by the avalanche at the bed surface, as shown in the schema of figure 6.5.

Figure 6.6 shows an example of the pressure response to the front arriving in the bed. It was possible to compare the timing of the pressure signals with the arrival of the front, by comparing images with the timing of the pressure increase. Here, the pressure increased exactly when the front arrived, after a small prior drop which means that no pressure signal is transmitted downstream ahead of the front. Calibration would need to be performed in future studies in order to get absolute measurements, which would show whether the pressure increase corresponds with expected hydrodynamic pressures in the flow, or whether there is an extra contribution due to stress-induced excess pore-pressure.

6.2 Discussion

Rheological behaviour

Similar experiments were carried out without entrainment [63, 137] for a range of concentrations of suspension. In these experiments the suspending fluid differed in that it was density matched, and the slope was 25° , an inclination that was not possible for the present study due to logistical constraints imposed by the loose bed. However they consistently found no slip at the base, in the same flume as was used for this study. Away from the front their velocity profiles were well fitted by a power law, and close to the front a parabolic profile performed better. For this reason it is expected that the rheological behaviour is more complicated than a viscoplastic model, and indeed the velocity profiles shown on the right of figure 6.2 differ somewhat from those shown in figure 5.7 (c & d).

A particular difference is that the earlier profiles show almost no velocity for the suspension – the flow must exert a certain stress on the bed before it yields. This could be due to the roughness of the surface of the bed, something that was not encountered in viscoplastic experiments. However once the bed material has yielded, some similarities are observed: a corner of no flow is observed next to the step and basal slip occurs downstream. The interface between avalanche and bed material has qualitative similarities and the bed material moves upwards just downstream of the front in a similar way to that seen in viscoplastic experiments.

An improved series of experiments, including a comparison with the no-entrainment case should be performed in order to obtain a reliable set of results which gives information about the rheological behaviour of an entraining gravity-driven flow of granular suspension. This preliminary set of results shows that the experimental technique is applicable to granular suspensions, pending a few improvements.

Finally the recirculation zones set up in flows with dilute areas in the bed hint at some interesting effects of having differing concentrations in the bed and in the granular dam-break. How this kind of experiment might be implemented in the lab is an interesting question which deserves some consideration.

Problems encountered and suggested improvements

In every experiment, when the loose bed failed, it began to slip on the base. A solution to this problem could be to stick similar PMMA beads on the flume base with PMMA glue of the same refractive index, as the camera must still be able to film through the base. However it is unclear whether even this would stop the flows from slipping. Ancy et al [63, 137] found no slip when using the same flume for non-entraining flows of a similar suspension, yet Sanvitale & Bowman [61] found significant slip when

filming flows with multiple sizes of rough particles in the centre, despite covering the flume with a slip-resistant layer. Performing experiments on a rough base would at least indicate the origin of the slip, e.g. if slip still occurs at the base, even over a rough base, then perhaps the slip is inherent to the problem, originating from increased pore pressure as the overriding flow increases stresses at the base.

The pressure sensors were difficult to use, and their results were not always satisfactory, however with proper calibration it could be shown whether there is increased pore pressure in the base of the flow. Already it was found that the pressure increased when the avalanche front flowed over the entrainable bed at that point, but it remains to be seen whether this pressure was in line with hydrodynamic pressure or whether it had extra contributions from shear-induced excess pore-pressure due to particle interactions.

Finally, measures should be taken to stop the fluid draining away from the loose bed, and down the sides of the step. The suspension seemed to thicken with time, indicating that more fluid than particles was lost, but this was not measurable as some particles were also lost due to cleaning methods. Similarly, the concentration of the suspension probably increased in the bed during the experiments due to drainage, and the overall concentration of the suspension used probably increased during the campaign. It is suggested to seal the entrainable bed and the sides of the steps to avoid drainage, but this would not avoid fluid filtering downstream through the loose material and potentially overflowing the bed. Some innovation is required in this problem, indeed the suspension may have to be density-matched to avoid this, but using the density- and refractive index-matched suspending fluid Trimix [63, 137] adds the problems of chemical damage to the flume and to the beads.

7.1 Summary

During this thesis three experimental campaigns were undertaken, in order to address the lack of good-quality experimental data on entrainment by gravity-driven flows. Specifically, no study until now had taken continuous velocity measurements during entrainment in the interior of the flow, far from the sidewalls.

Viscous dam-breaks

The first experimental campaign used a Newtonian fluid which encountered a shallow layer of loose material some way down a horizontal channel. It was shown that even when this layer was very shallow, its presence significantly advanced the flow front, leading to a seemingly permanent increase in flow position compared to the non-entraining case. The length of the entrainable zone was the most influential parameter, and increasing the depth of available material had a smaller effect. This suggests that the increase was due to the sudden removal of the fluid-air-solid contact line and no-slip condition on $z = 0$.

Internal measurements showed that the fluid in the entrainable bed was set into motion instantaneously, and the fluid from the dam-break gradually displaced the bed fluid, causing upwards motion inside the bed downstream of the front. Internal velocities were shown to increase with increasing bed depth both in the vertical and horizontal direction.

When the flow front arrived at the end of the bed, it slowed down until the front was steep enough and the front height was great enough. In light of a model developed without surface tension, simulating flow in a geometry without sharp corners, this behaviour is attributed to the fact that a large enough velocity gradient must be set up before the flow can exit the entrainable zone and flow on a rigid surface once more,

obeying the no-slip condition at $z = 0$.

A theoretical model was developed from first principles based on Huppert [49], in which a layer of stationary material lying below $z = 0$ is incorporated immediately into the flow. When $h(x, t) = 0$ fluid at x is stationary, and the no-slip condition is applied on the bottom of this material $z = b(x) \leq 0$. This model successfully reproduced the trajectory of the flow front along the flume, including over the entrainable region. Further, the model was able to simulate the internal velocities, surface height and avalanche/bed interface deformation.

The model did not take into account surface tension nor strong horizontal variations in surface height or velocity, and yet it performed excellently. The corners of the bed were modelled as hyperbolic tangents, removing the singularity at the steps. Therefore none of these three complications was important in the evolution of the flow.

Viscoplastic avalanches on a slope

In light of the success of the first experimental campaign, similar methods were applied to viscoplastic material flowing down a slope. In order to have a stationary layer of identical material on a slope, the fluid properties and the slopes studied had to be chosen carefully. Flume inclination and quantity of entrainable material were both studied to see their effects on an entraining gravity-driven flow.

In order to compare the different slopes, entraining flows were contrasted with non-entraining flows at each inclination. At a first glance the curves for flow front position appear to collapse perfectly one upon the other at each slope. Both the depth and length of the entrainable zone had significant effects on front advancement, in contrast to the Newtonian case. The avalanche progressively hollowed out the entrainable material, and the surface shape followed the rigid geometry, with the bed material eventually pushed downstream, explaining the dependence on bed depth.

Similarly to the previous experiments, it was found that the avalanche sank into the entrainable bed, forcing downstream material upwards, however the viscoplastic nature of the fluid meant that this happened more locally than for the viscous case. Significant apparent slip was observed at shallower slopes during entrainment, but not in the non-entraining flows or at steeper slopes. The avalanche appeared to lose momentum to the bed, with a decrease in internal velocities compared to the non-entraining avalanche, except where significant basal slip occurred. Considering the bed excavation, shown by the avalanche/bed interface, the avalanche intruded much more prominently into the bed at shallower slopes. It was interesting to note that internal velocities should exhibit slope-dependence of internal measurements and not bulk measurements.

The success of the lubrication model for entraining viscous dam-breaks suggested a similar model for viscoplastic flows. However these models have been less successful than their Newtonian counterparts in reproducing experimental results. For this reason, the theoretical model developed in this thesis was used to compare entraining flows to non-entraining flows in order to model the effect of entrainment but not the outright flow.

In all cases, the model showed excellent agreement with experimental results when comparing the flow front to its non-entraining equivalent. It also reproduced velocity fields and surface heights qualitatively well. Further study of the numerical results showed that front advancement did depend on slope, but only slightly, that front advancement over the bed was roughly linear, and that bed depth and length does indeed appear to increase the front position in a permanent way.

Dam-breaks of granular suspension

A set of preliminary experiments was performed in order to test the feasibility of this kind of experiment for granular suspensions. Although some improvements are required (summarised below in the suggestions for future work), the results are promising, and a qualitative description of entrainment by avalanches of granular suspension has been obtained. The avalanche moves out onto the entrainable bed with no initial effect, and after some shallow skimming of particles from the top layer of the bed, the bed layer fails. Interestingly, a deeper bed presented more flow resistance and reduced flow velocities compared to a shallower bed, which shows that the type of model derived in the previous section might not be suitable, as surface roughness and particle jamming might need to be taken into account.

7.2 Suggestions for future work

Improved granular suspension experiments

As mentioned above, the work carried out in chapter 6 is a promising first attempt at experiments on entraining granular avalanches. Some improvements need to be made, however, before full and reliable results can be obtained:

- A series of experiments should be carried out on a flume with a rough base, for example by glueing PMMA beads onto a thin plastic insert. Care must be taken that camera 1 can still obtain images through this layer. In this way the origin of the slip that has been observed at the base can be identified. For example, if slip still occurs at the base, even over a rough base, then perhaps the slip is inherent to the problem, originating from increased pore pressure as the overriding flow

shears the entrainable bed.

- During the experiments, the suspension separated somewhat, losing fluid down the sides of the step inserts placed in the flume. For better experimental results, the gaps down the sides of the steps should be filled in, and the entrainable bed should be made leak-proof, so that no fluid drains away downstream.
- The pressure sensors installed could provide useful information about pore-fluid pressure, if properly calibrated. In this case, non-entraining flows should be compared with entraining flows, with surface height profiles closely monitored, in order to see whether the pressure readings correspond to the expected hydrodynamics of the system, or are elevated in line with increased pore pressure.
- It may be necessary to use a density-matched suspension, to avoid drainage of the fluid phase downstream through the entrainable bed, however this would require adding Dibromohexane which is known to corrode PMMA.

Testing the models on more complex cases

The models that were developed here looked at entrainment in a new, global way: instead of a local mass exchange between the avalanche and the bed through a static/flowing surface, the entire loose bed was included in the flow domain from the moment the avalanche front entered the entrainable zone and the flow was modelled as a continuum. This may have implications for avalanche and debris flow models which include entrainment. Instead of requiring exchange and growth parameters for the avalanche and the bed, models may need only to know the quantity of loose material available for example the total snow lying above a hard surface, or the total loose sediment lying in a debris flow gully.

However more research is necessary before it is known whether this is possible. The models developed here were based on a simple geometry with a flat bed surface at $z = 0$. In nature this is not the case and studies could be undertaken with either more complex rigid bed geometry, filled with entrainable material, or with an entrainable zone which has a non-zero or variable bed surface.

Further, entrainable material may not have the same properties as that in the overriding avalanche, it would be interesting to see how far the model could be pushed, and what differences are produced when the bed has a different composition from the avalanche, as discussed in section 5.4. A more complicated model could be developed based on system (5.5), but with two layers of fluid of different properties. For example, solving system (3.2) simultaneously for two different layers that have continuous velocities on an evolving interface $I(x, t)$ may be possible.



Glossary

PMMA, Polymethyl Methacrylate

PIV, Particle Image Velocimetry

l_{bed} , length of entrainable zone

l_{step} , length from reservoir back wall to entrainable zone

δh , depth of entrainable layer

θ , channel inclination

Runs C and R , combined (all dyed) or reservoir run (only dam-break dyed)

ρ , fluid density

μ , dynamic viscosity

ν , kinematic viscosity

V_0 , volume per unit width

$\mathbf{d} = 1/2(\partial u_i/\partial x_j + \partial u_j/\partial x_i)$, rate of strain tensor

$\dot{\gamma} = \sqrt{1/2\text{tr}(\mathbf{d}^2)}$, second invariant of rate of strain tensor

τ , total stress

K , consistency (Herschel Bulkley)

n , index (Herschel Bulkley)

τ_c , critical yield stress (Herschel Bulkley)

σ , extra stress tensor

H , characteristic height

L , characteristic length

$B = \tau_c/(\rho g H \sin \theta)$, Bingham number

$h_c = \tau_c/\rho g \sin \theta$

$A = (\rho g \sin \theta / K)^{1/n}$

$S = \cot \theta$

t_e , time of front entry into entrainable zone

$b(x)$, function describing arbitrary rigid base

$p(x, z, t)$, pressure

$(u(x, z, t), w(x, z, t))$, horizontal and vertical velocity components

$h(x, t)$, current surface height

$h_0(x)$, initial condition for entrainment, comes from solution over rigid bed

T_c , time-scale for bed acceleration

$x_H(t)$, Huppert solution for flow front position

η_H , value of similarity variable η at flow front

$Y(x, t)$, yield surface (viscoplastic)

$x_N(t)$, front position: furthest downstream point with $h > 0$

$x_F(t)$, front of the overriding current

$d_{max}(t)$, maximum depth of bed/current interface

$\Delta X_i(t) = x_{N,i}(t) - x_{N,0}$, front advancement due to entrainment

RI, refractive index (suspensions)

μ_b , bulk viscosity (suspension)

ϕ , solid fraction

ϕ_m , random close packing fraction



Bibliography

- [1] N. Hilker, A. Badoux, and C. Hegg. The swiss flood and landslide damage database 1972-2007. *Nat. Hazard. Earth Sys.*, 9(3):913–925, 2009.
- [2] W. J. Ammann. *Der Lawinenwinter 1999*. Eidgenössisches Institut für Schnee- und Lawinenforschung, Davos, 2000.
- [3] R. M. Iverson, D. L. George, K. Allstadt, M. E. Reid, B. D. Collins, J. W. Vallance, S. P. Schilling, J. W. Godt, C. M. Cannon, C. S. Magirl, R. L. Baum, J. A. Coe, W. H. Schulz, and J. B. Bower. Landslide mobility and hazards: implications of the 2014 oso disaster. *Earth Planet. Sci. Lett.*, 412:197–208, 2015.
- [4] C. C. Mei, K. F. Liu, and M. Yuhi. *Mud flow - Slow and fast*, volume 582, pages 548–577. Springer, 2001.
- [5] T. C. Pierson. Flow characteristics of large eruption-triggered debris flows at snow-clad volcanos - constraints for debris-flow models. *J. Volcanol. Geotherm. Res.*, 66(1-4):283–294, 1995.
- [6] D. Hungr and S. G. Evans. Entrainment of debris in rock avalanches: An analysis of a long run-out mechanism. *Geol. Soc. Am. Bull.*, 116(9-10):1240–1252, 2004.
- [7] B. Sovilla, P. Burlando, and P. Bartelt. Field experiments and numerical modeling of mass entrainment in snow avalanches. *J. Geophys. Res.-Earth*, 111(F3), 2006.
- [8] D. Rickenmann. Empirical relationships for debris flows. *Nat. Hazards*, 19(1): 47–77, 1999.
- [9] D. Rickenmann and M. Zimmermann. The 1987 debris flows in switzerland - documentation and analysis. *Geomorphology*, 8(2-3):175–189, 1993.
- [10] G. H. Wang, K. Sassa, and H. Fukuoka. Downslope volume enlargement of a debris slide-debris flow in the 1999 hiroshima, japan, rainstorm. *Eng. Geol.*, 69 (3-4):309–330, 2003.
- [11] J. D. Stock and W. E. Dietrich. Erosion of steepland valleys by debris flows. *Geol. Soc. Am. Bull.*, 118(9-10):1125–1148, 2006.

Bibliography

- [12] S. A. Sepulveda, S. Rebolledo, and G. Vargas. Recent catastrophic debris flows in Chile: Geological hazard, climatic relationships and human response. *Quatern. Int.*, 158:83–95, 2006.
- [13] D. Issler, A. Errera, S. Priano, H. Gubler, B. Teufen, and B. Krummenacher. Inferences on flow mechanisms from snow avalanche deposits. *Ann. Glaciol.*, 49: 187–192, 2008.
- [14] S. J. Conway, A. Decaulne, M. R. Balme, J. B. Murray, and M. C. Towner. A new approach to estimating hazard posed by debris flows in the westfjords of Iceland. *Geomorphology*, 114(4):556–572, 2010.
- [15] J. A. Coe, J. W. Kean, J. W. Godt, R. L. Baum, E. S. Jones, D. J. Gochis, and G. S. Anderson. New insights into debris-flow hazards from an extraordinary event in the Colorado Front Range. *GSA Today*, 24(10):4–10, 2014.
- [16] J. Vallet, U. Gruber, and F. Dufour. Photogrammetric avalanche volume measurements at Vallee de la Sionne, Switzerland. *Ann. Glaciol.*, 32:141–146, 2001.
- [17] P. Gauer, D. Issler, K. Lied, K. Kristensen, H. Iwe, E. Lied, L. Rammer, and H. Schreiber. On full-scale avalanche measurements at the Ryggfjonn test site, Norway. *Cold Reg. Sci. Technol.*, 49(1):39–53, 2007.
- [18] M. Hurlimann, D. Rickenmann, and C. Graf. Field and monitoring data of debris-flow events in the Swiss Alps. *Can. Geotech. J.*, 40(1):161–175, 2003.
- [19] W. J. Ammann. A new Swiss test-site for avalanche experiments in the Vallee de la Sionne/Valais. *Cold Reg. Sci. Technol.*, 30(1-3):3–11, 1999.
- [20] B. Sovilla, M. Schaer, and L. Rammer. Measurements and analysis of full-scale avalanche impact pressure at the Vallee de la Sionne test site. *Cold Reg. Sci. Technol.*, 51(2-3):122–137, 2008.
- [21] B. Sovilla, J. N. McElwaine, M. Schaer, and J. Vallet. Variation of deposition depth with slope angle in snow avalanches: Measurements from Vallee de la Sionne. *J. Geophys. Res.-Earth*, 115, 2010.
- [22] N. M. Vriend, J. N. McElwaine, B. Sovilla, C. J. Keylock, M. Ash, and P. V. Brennan. High-resolution radar measurements of snow avalanches. *Geophys. Res. Lett.*, 40(4):727–731, 2013.
- [23] M. Ash, P. V. Brennan, C. J. Keylock, N. M. Vriend, J. N. McElwaine, and B. Sovilla. Two-dimensional radar imaging of flowing avalanches. *Cold Reg. Sci. Technol.*, 102:41–51, 2014.
- [24] R. M. Iverson. The physics of debris flows. *Rev. Geophys.*, 35(3):245–296, 1997.
- [25] T. Takahashi. Debris flow. *Annu. Rev. Fluid Mech.*, 13:57–77, 1981.

- [26] J. M. N. T. Gray and C. Ancey. Segregation, recirculation and deposition of coarse particles near two-dimensional avalanche fronts. *J. Fluid Mech.*, 629:387–423, 2009.
- [27] C. G. Johnson, B. P. Kokelaar, R. M. Iverson, M. Logan, R. G. LaHusen, and J. M. N. T. Gray. Grain-size segregation and levee formation in geophysical mass flows. *J. Geophys. Res.-Earth*, 117, 2012.
- [28] P. Bartelt and B. W. McArdell. Granulometric investigations of snow avalanches. *J. Glaciol.*, 55(193):829–833, 2009.
- [29] J. J. Major and T. C. Pierson. Debris flow rheology - experimental-analysis of fine-grained slurries. *Water Resour. Res.*, 28(3):841–857, 1992.
- [30] C. Ancey. Plasticity and geophysical flows: A review. *J. Non-Newton. Fluid*, 142 (1-3):4–35, 2007.
- [31] S. W. McCoy, J. W. Kean, J. A. Coe, D. M. Staley, T. A. Wasklewicz, and G. E. Tucker. Evolution of a natural debris flow: In situ measurements of flow dynamics, video imagery, and terrestrial laser scanning. *Geology*, 38(8):735–738, 2010.
- [32] T. C. Pierson and K. M. Scott. Downstream dilution of a lahar - transition from debris flow to hyperconcentrated streamflow. *Water Resour. Res.*, 21(10):1511–1524, 1985.
- [33] P. Bartelt, O. Buser, and K. Platzer. Starving avalanches: Frictional mechanisms at the tails of finite-sized mass movements. *Geophys. Res. Lett.*, 34(20), 2007.
- [34] J. W. Kean, S. W. McCoy, G. E. Tucker, D. M. Staley, and J. A. Coe. Runoff-generated debris flows: Observations and modeling of surge initiation, magnitude, and frequency. *J. Geophys. Res.-Earth*, 118(4):2190–2207, 2013.
- [35] R. M. Iverson. The debris-flow rheology myth. In D. Rickenmann and C. L. Chen, editors, *Debris-Flow Hazards Mitigation: Mechanics, Prediction, and Assessment, Vols 1 and 2*, pages 303–314, 2003.
- [36] P. Schurch, A. L. Densmore, N. J. Rosser, and B. W. McArdell. Dynamic controls on erosion and deposition on debris-flow fans. *Geology*, 39(9):827–830, 2011.
- [37] R. M. Iverson, M. Logan, R. G. LaHusen, and M. Berti. The perfect debris flow? aggregated results from 28 large-scale experiments. *J. Geophys. Res.-Earth*, 115, 2010.
- [38] B. W. McArdell, P. Bartelt, and J. Kowalski. Field observations of basal forces and fluid pore pressure in a debris flow. *Geophys. Res. Lett.*, 34(7), 2007.
- [39] M. A. Kern, F. Tiefenbacher, and J. N. McElwaine. The rheology of snow in large chute flows. *Cold Reg. Sci. Technol.*, 39(2-3):181–192, 2004.

Bibliography

- [40] R. M. Iverson. Scaling and design of landslide and debris-flow experiments. *Geomorphology*, 2015 - in press.
- [41] M. Larcher, L. Fraccarollo, A. Armanini, and H. Capart. Set of measurement data from flume experiments on steady uniform debris flows. *J. Hydraul. Res.*, 45: 59–71, 2007.
- [42] M. A. Cabrera, D. Gollin, R. Kaitna, and W. Wu. *Viscous Effects on Granular Mixtures in a Rotating Drum*, pages 57–71. Springer, 2015.
- [43] R. Kaitna, W. E. Dietrich, and L. Hsu. Surface slopes, velocity profiles and fluid pressure in coarse-grained debris flows saturated with water and mud. *J. Fluid Mech.*, 741:377–403, 2014.
- [44] A. Leonardi, M. Cabrera, F. K. Wittel, R. Kaitna, M. Mendoza, W. Wu, and H. J. Herrmann. Granular front formation in free-surface flow of concentrated suspensions. Submitted to *Soft Condensed Matter*, 2015.
- [45] L. Caballero, D. Sarocchi, L. Borselli, and A. I. Cardenas. Particle interaction inside debris flows: Evidence through experimental data and quantitative clast shape analysis. *J. Volcanol. Geotherm. Res.*, 231:12–23, 2012.
- [46] L. Hsu, W. E. Dietrich, and L. S. Sklar. Experimental study of bedrock erosion by granular flows. *J. Geophys. Res.-Earth*, 113(F2), 2008.
- [47] G. Chambon, A. Ghemmour, and M. Naaïm. Experimental investigation of viscoplastic free-surface flows in a steady uniform regime. *J. Fluid Mech.*, 754: 332–364, 2014.
- [48] J. Hubl and H. Steinwendtner. Estimation of rheological properties of viscous debris flow using a belt conveyor. *Phys. Chem. Earth Pt. B*, 25(9):751–755, 2000.
- [49] H. E. Huppert. The propagation of two-dimensional and axisymmetric viscous gravity currents over a rigid horizontal surface. *J. Fluid Mech.*, 121(Aug):43–58, 1982.
- [50] J. R. Lister and R. C. Kerr. The propagation of two-dimensional and axisymmetric viscous gravity currents at a fluid interface. *J. Fluid Mech.*, 203:215–249, 1989.
- [51] S. Longo, V. Di Federico, and L. Chiapponi. Propagation of viscous gravity currents inside confining boundaries: the effects of fluid rheology and channel geometry. *Proc. R. Soc. Lon. Ser.-A*, 471:20150070, 2015.
- [52] H. E. Huppert. Flow and instability of a viscous current down a slope. *Nature*, 300(5891):427–429, 1982.
- [53] C. Ancey and S. Cochard. The dam-break problem for herschel-bulkley viscoplastic fluids down steep flumes. *J. Non-Newton. Fluid*, 158(1-3):18–35, 2009.

- [54] K. N. Kowal and M. G. Worster. Lubricated viscous gravity currents. *J. Fluid Mech.*, 766, 2015.
- [55] P. Coussot and S. Proust. Slow, unconfined spreading of a mudflow. *J. Geophys. Res.-Sol Ea*, 101(B11):25217–25229, 1996.
- [56] X. Huang and M. H. Garcia. A herschel-bulkley model for mud flow down a slope. *J. Fluid Mech.*, 374:305–333, 1998.
- [57] P. Coussot, Q. D. Nguyen, H. T. Huynh, and D. Bonn. Avalanche behavior in yield stress fluids. *Phys. Rev. Lett.*, 88(17), 2002.
- [58] N. J. Balmforth, R. V. Craster, A. C. Rust, and R. Sassi. Viscoplastic flow over an inclined surface. *J. Non-Newton. Fluid*, 139(1-2):103–127, 2006.
- [59] N. J. Balmforth, R. V. Craster, P. Perona, A. C. Rust, and R. Sassi. Viscoplastic dam breaks and the bostwick consistometer. *J. Non-Newton. Fluid*, 142(1-3):63–78, 2007.
- [60] S. Cochard and C. Ancey. Experimental investigation of the spreading of viscoplastic fluids on inclined planes. *J. Non-Newton. Fluid*, 158(1-3):73–84, 2009.
- [61] N. Sanvitale and E. T. Bowman. Internal imaging of saturated granular free-surface flows. *Int. J. Phys. Modell. Geotech.*, 12(4):129–142, 2012.
- [62] N. Andreini, G. Epely-Chauvin, and C. Ancey. Internal dynamics of newtonian and viscoplastic fluid avalanches down a sloping bed. *Phys. Fluids*, 24(5), 2012.
- [63] C. Ancey, N. Andreini, and G. Epely-Chauvin. The dam-break problem for concentrated suspensions of neutrally buoyant particles. *J. Fluid Mech.*, 724: 95–122, 2013.
- [64] A. Mangeney-Castelnau, J. P. Vilotte, M. O. Bristeau, B. Perthame, F. Bouchut, C. Simeoni, and S. Yerneni. Numerical modeling of avalanches based on saint-venant equations using a kinetic scheme. *J. Geophys. Res.-Sol Ea*, 108(B11), 2003.
- [65] E. B. Pitman and L. Le. A two-fluid model for avalanche and debris flows. *Philos. T. R. Soc. A*, 363(1832):1573–1601, 2005.
- [66] D. Berzi and J. T. Jenkins. A theoretical analysis of free-surface flows of saturated granular-liquid mixtures. *J. Fluid Mech.*, 608:393–410, 2008.
- [67] S. P. Pudasaini. A general two-phase debris flow model. *J. Geophys. Res.-Earth*, 117, 2012.
- [68] J. Kowalski and J. N. McElwaine. Shallow two-component gravity-driven flows with vertical variation. *J. Fluid Mech.*, 714:434–462, 2013.

Bibliography

- [69] M. Christen, J. Kowalski, and P. Bartelt. Ramms: Numerical simulation of dense snow avalanches in three-dimensional terrain. *Cold Reg. Sci. Technol.*, 63(1-2): 1–14, 2010.
- [70] S. B. Savage and K. Hutter. The motion of a finite mass of granular material down a rough incline. *J. Fluid Mech.*, 199:177–215, 1989. T5058 Times Cited:659 Cited References Count:63.
- [71] B. Salm. Flow, flow transition and runout distances of flowing avalanches. *Ann. Glaciol.*, 18:221–226, 1993.
- [72] P. Bartelt, O. Buser, and K. Platzer. Fluctuation-dissipation relations for granular snow avalanches. *J. Glaciol.*, 52(179):631–643, 2006.
- [73] D. Rickenmann, D. Laigle, B. W. McArdell, and J. Hubl. Comparison of 2d debris-flow simulation models with field events. *Computat. Geosci.*, 10(2):241–264, 2006.
- [74] D. L. George and R. M. Iverson. A two-phase debris-flow model that includes coupled evolution of volume fractions, granular dilatancy, and pore-fluid pressure. In R. Genevois, D. L. Hamilton, and A. Prestinzi, editors, *Fifth international conference on debris-flow hazards mitigation, mechanics, prediction and assessment*, pages 415–424, 2011.
- [75] P. Gauer and D. Issler. Possible erosion mechanisms in snow avalanches. *Ann. Glaciol.*, 38:384–392, 2004.
- [76] S. W. McCoy, J. W. Kean, J. A. Coe, G. E. Tucker, D. M. Staley, and T. A. Wasklewicz. Sediment entrainment by debris flows: In situ measurements from the headwaters of a steep catchment. *J. Geophys. Res.-Earth*, 117, 2012.
- [77] R. M. Iverson, M. E. Reid, M. Logan, R. G. LaHusen, J. W. Godt, and J. P. Griswold. Positive feedback and momentum growth during debris-flow entrainment of wet bed sediment. *Nat. Geosci.*, 4(2):116–121, 2011.
- [78] S. McDougall and O. Hungr. Dynamic modelling of entrainment in rapid landslides. *Can. Geotech. J.*, 42(5):1437–1448, 2005.
- [79] H. Chen, G. B. Crosta, and C. F. Lee. Erosional effects on runout of fast landslides, debris flows and avalanches: a numerical investigation. *Geotechnique*, 56(5): 305–322, 2006.
- [80] B. Sovilla, S. Margreth, and P. Bartelt. On snow entrainment in avalanche dynamics calculations. *Cold Reg. Sci. Technol.*, 47(1-2):69–79, 2007.
- [81] J. M. N. T. Gray. Granular flow in partially filled slowly rotating drums. *J. Fluid Mech.*, 441:1–29, 2001.

-
- [82] M. E. Eglit and K. S. Demidov. Mathematical modeling of snow entrainment in avalanche motion. *Cold Reg. Sci. Technol.*, 43(1-2):10–23, 2005.
- [83] R. M. Iverson and C. J. Ouyang. Entrainment of bed material by earth-surface mass flows: Review and reformulation of depth-integrated theory. *Rev. Geophys.*, 53(1):27–58, 2015.
- [84] J. P. Bouchaud, M. E. Cates, J. R. Prakash, and S. F. Edwards. A model for the dynamics of sandpile surfaces. *J. Phys. I*, 4(10):1383–1410, 1994.
- [85] C. Lusso, F. Bouchut, A. Ern, and A. Mangeney. A simplified model of thin layer static/flowing dynamics for granular materials with yield. <hal-00992309v2>, 2015.
- [86] F. Bouchut, I. R. Ionescu, and A. Mangeney. A shallow model including static-flowing transition for viscoplastic drucker-prager materials. <hal-01081213v2>, 2014.
- [87] D. Issler and M. P. Perez. Interplay of entrainment and rheology in snow avalanches: a numerical study. *Ann. Glaciol.*, 52(58):143–147, 2011.
- [88] M. E. Eglit and A. E. Yakubenko. Numerical modeling of slope flows entraining bottom material. *Cold Reg. Sci. Technol.*, 108:139–148, 2014.
- [89] D. Issler. Dynamically consistent entrainment laws for depth-averaged avalanche models. *J. Fluid Mech.*, 759, 2014.
- [90] L. Le and E. B. Pitman. A model for granular flows over an erodible surface. *Siam J. Appl. Math.*, 70(5):1407–1427, 2009.
- [91] B. Q. Luna, A. Remaitre, T. W. J. van Asch, J. P. Malet, and C. J. van Westen. Analysis of debris flow behavior with a one dimensional run-out model incorporating entrainment. *Eng. Geol.*, 128:63–75, 2012.
- [92] I. S. Aranson and L. S. Tsimring. Continuum theory of partially fluidized granular flows. *Phys. Rev. E*, 65(6), 2002.
- [93] A. Mangeney, L. S. Tsimring, D. Volfson, I. S. Aranson, and F. Bouchut. Avalanche mobility induced by the presence of an erodible bed and associated entrainment. *Geophys. Res. Lett.*, 34(22), 2007.
- [94] A. Mangeney, O. Roche, O. Hungr, N. Mangold, G. Faccanoni, and A. Lucas. Erosion and mobility in granular collapse over sloping beds. *J. Geophys. Res.-Earth*, 115, 2010.
- [95] M. Farin, A. Mangeney, and O. Roche. Fundamental changes of granular flow dynamics, deposition, and erosion processes at high slope angles: Insights from laboratory experiments. *J. Geophys. Res.-Earth*, 119(3):504–532, 2014.

Bibliography

- [96] M. Barbolini, A. Biancardi, F. Cappabianca, L. Natale, and M. Pagliardi. Laboratory study of erosion processes in snow avalanches. *Cold Reg. Sci. Technol.*, 43 (1-2):1–9, 2005.
- [97] O. Roche, Y. Nino, A. Mangeney, B. Brand, N. Pollock, and G. A. Valentine. Dynamic pore-pressure variations induce substrate erosion by pyroclastic flows. *Geology*, 41(10):1107–1110, 2013.
- [98] J. Estep and J. Dufek. Substrate effects from force chain dynamics in dense granular flows. *J. Geophys. Res.-Earth*, 117, 2012.
- [99] A. Dufresne. Granular flow experiments on the interaction with stationary runout path materials and comparison to rock avalanche events. *Earth Surf. Proc. Land.*, 37(14):1527–1541, 2012.
- [100] M. Papa, S. Egashira, and T. Itoh. Critical conditions of bed sediment entrainment due to debris flow. *Nat. Hazard. Earth Sys.*, 4(3):469–474, 2004.
- [101] P. J. Rowley, P. Kokelaar, M. Menzies, and D. Waltham. Shear-derived mixing in dense granular flows. *J. Sediment. Res.*, 81(11-12):874–884, 2011.
- [102] R. E. Altenhofen. *Rectification*, volume 14. American Society of Photogrammetry, 1952.
- [103] J. K. Sveen. *An introduction to MatPIV v. 1.6.1*. Mechanics and Applied Mathematics, technical report no. 2 edition, 2004.
- [104] B. M. Wilson and B. L. Smith. Uncertainty on piv mean and fluctuating velocity due to bias and random errors. *Meas. Sci. Technol.*, 24(3), 2013.
- [105] N. Didden and T. Maxworthy. The viscous spreading of plane and axisymmetric gravity currents. *J. Fluid Mech.*, 121(Aug):27–42, 1982.
- [106] P. Moller, A. Fall, V. Chikkadi, D. Derks, and D. Bonn. An attempt to categorize yield stress fluid behaviour. *Philos. T. R. Soc. A*, 367(1909):5139–5155, 2009.
- [107] H. A. Barnes. *A Handbook of elementary rheology*. University of Wales Institute of Non-Newtonian Fluid Mechanics, 2000.
- [108] G. P. Roberts and H. A. Barnes. New measurements of the flow-curves for carbopol dispersions without slip artefacts. *Rheol. Acta*, 40(5):499–503, 2001.
- [109] P. Coussot. Yield stress fluid flows: A review of experimental data. *J. Non-Newton. Fluid*, 211:31–49, 2014.
- [110] G. Baek and C. Kim. Rheological properties of carbopol containing nanoparticles. *J. Rheol.*, 55(2):313–330, 2011.

-
- [111] H. A. Barnes. A review of the slip (wall depletion) of polymer-solutions, emulsions and particle suspensions in viscometers - its cause, character, and cure. *J. Non-Newton. Fluid*, 56(3):221–251, 1995.
- [112] N. J. Balmforth, R. V. Craster, and R. Sassi. Shallow viscoplastic flow on an inclined plane. *J. Fluid Mech.*, 470:1–29, 2002.
- [113] A. J. Hogg and G. P. Matson. Slumps of viscoplastic fluids on slopes. *J. Non-Newton. Fluid*, 158(1-3):101–112, 2009.
- [114] K. F. Liu and C. C. Mei. Slow spreading of a sheet of bingham fluid on an inclined plane. *J. Fluid Mech.*, 207:505–529, 1989.
- [115] G. P. Matson and A. J. Hogg. Two-dimensional dam break flows of herschel-bulkley fluids: The approach to the arrested state. *J. Non-Newton. Fluid*, 142(1-3):79–94, 2007.
- [116] N. J. Balmforth and R. V. Craster. *Geophysical aspects of non-Newtonian fluid mechanics*, volume 582, pages 34–51. Springer, 2001.
- [117] C. Ancey, N. Andreini, and G. Epely-Chauvin. Viscoplastic dambreak waves: Review of simple computational approaches and comparison with experiments. *Adv. Water Resour.*, 48:79–91, 2012.
- [118] M. J. Lighthill and G. B. Whitham. On kinematic waves .1. flood movement in long rivers. *Proc. R. Soc. Lon. Ser.-A*, 229(1178):281–316, 1955.
- [119] P. Coussot and C. Ancey. Rheophysical classification of concentrated suspensions and granular pastes. *Phys. Rev. E*, 59(4):4445–4457, 1999.
- [120] J. J. Stickel and R. L. Powell. Fluid mechanics and rheology of dense suspensions. *Annu. Rev. Fluid Mech.*, 37:129–149, 2005.
- [121] E. Guazzelli and J. F. Morris. *A Physical Introduction to Suspension Dynamics*, volume 45 of *Cambridge Texts in Applied Mathematics*. Cambridge University Press, 2012.
- [122] C. J. Koh, P. Hookham, and L. G. Leal. An experimental investigation of concentrated suspension flows in a rectangular channel. *J. Fluid Mech.*, 266:1–32, 1994.
- [123] T. Ward, C. Wey, R. Glidden, A. E. Hosoi, and A. L. Bertozzi. Experimental study of gravitation effects in the flow of a particle-laden thin film on an inclined plane. *Phys. Fluids*, 21(8), 2009.
- [124] R. J. Phillips, R. C. Armstrong, R. A. Brown, A. L. Graham, and J. R. Abbott. A constitutive equation for concentrated suspensions that accounts for shear-induced particle migration. *Phys. Fluids*, 4(1):30–40, 1992.

Bibliography

- [125] D. M. Hanes and D. L. Inman. Experimental evaluation of a dynamic yield criterion for granular fluid-flows. *J. Geophys. Res.-Solid*, 90(Nb5):3670–3674, 1985. Agt69 Times Cited:42 Cited References Count:26.
- [126] D. Leighton and A. Acrivos. Measurement of shear-induced self-diffusion in concentrated suspensions of spheres. *J. Fluid Mech.*, 177:109–131, 1987.
- [127] D. Leighton and A. Acrivos. The shear-induced migration of particles in concentrated suspensions. *J. Fluid Mech.*, 181:415–439, 1987.
- [128] G. Ovarlez, F. Bertrand, and S. Rodts. Local determination of the constitutive law of a dense suspension of noncolloidal particles through magnetic resonance imaging. *J. Rheol.*, 50(3):259–292, 2006.
- [129] A. W. Chow, S. W. Sinton, J. H. Iwamiya, and T. S. Stephens. Shear-induced particle migration in couette and parallel-plate viscometers - nmr imaging and stress measurements. *Phys. Fluids*, 6(8):2561–2576, 1994.
- [130] S. Mueller, E. W. Llewellyn, and H. M. Mader. The rheology of suspensions of solid particles. *Proc. R. Soc. Lon. Ser.-A*, 2009.
- [131] L. Heymann, S. Peukert, and N. Aksel. On the solid-liquid transition of concentrated suspensions in transient shear flow. *Rheol. Acta*, 41(4):307–315, 2002.
- [132] C. Bonnoit, T. Darnige, E. Clement, and A. Lindner. Inclined plane rheometry of a dense granular suspension. *J. Rheol.*, 54(1):65–79, 2010.
- [133] N. Huang, G. Ovarlez, F. Bertrand, S. Rodts, P. Coussot, and D. Bonn. Flow of wet granular materials. *Phys. Rev. Lett.*, 94(2), 2005.
- [134] A. Fall, F. Bertrand, G. Ovarlez, and D. Bonn. Yield stress and shear banding in granular suspensions. *Phys. Rev. Lett.*, 103(17), 2009.
- [135] M. K. Lyon and L. G. Leal. An experimental study of the motion of concentrated suspensions in two-dimensional channel flow. part 1. monodisperse systems. *J. Fluid Mech.*, 363:25–56, 1998.
- [136] B. D. Timberlake and J. F. Morris. Particle migration and free-surface topography in inclined plane flow of a suspension. *J. Fluid Mech.*, 538:309–341, 2005.
- [137] C. Ancey, N. Andreini, and G. Epely-Chauvin. Granular suspension avalanches. i. macro-viscous behavior. *Phys. Fluids*, 25(3), 2013.
- [138] S. Wiederseiner, N. Andreini, G. Epely-Chauvin, and C. Ancey. Refractive-index and density matching in concentrated particle suspensions: a review. *Exp. Fluids*, 50(5):1183–1206, 2011.

-
- [139] I. M. Krieger and T. J. Dougherty. A mechanism for non-newtonian flow in suspensions of rigid spheres. *T. Soc. Rheol.*, 3:137–152, 1959.
- [140] S. Torquato, T. M. Truskett, and P. G. Debenedetti. Is random close packing of spheres well defined? *Phys. Rev. Lett.*, 84(10):2064–2067, 2000.
- [141] A. M. Leshansky and J. F. Brady. Dynamic structure factor study of diffusion in strongly sheared suspensions. *J. Fluid Mech.*, 527:141–169, 2005.
- [142] P. R. Nott and J. F. Brady. Pressure-driver flow of suspensions: simulation and theory. *J. Fluid Mech.*, 275:157–199, 1994.
- [143] D. F. McTigue and J. T. Jenkins. *Channel flow of a concentrated suspension*. Elsevier, 1992.
- [144] J. F. Morris and J. F. Brady. Pressure-driven flow of a suspension: Buoyancy effects. *Int. J. Multiphase Flow*, 24(1):105–130, 1998.
- [145] P. Mills and P. Snabre. Rheology and structure of concentrated suspensions of hard-spheres - shear-induced particle migration. *J. Phys. II*, 5(10):1597–1608, 1995.
- [146] N. Andreini and C. (Dir.) Ancey. Dam break of newtonian fluids and granular suspensions: Internal dynamics measurements. 2012.
- [147] I. E. Zarraga, D. A. Hill, and D. T. Leighton. The characterization of the total stress of concentrated suspensions of noncolloidal spheres in newtonian fluids. *J. Rheol.*, 44(2):185–220, 2000.
- [148] A. Fall, H. de Cagny, D. Bonn, G. Ovarlez, E. Wandersman, J. A. Dijksman, and M. van Hecke. Rheology of sedimenting particle pastes. *J. Rheol.*, 57(4):1237–1246, 2013.
- [149] E. Brown and H. M. Jaeger. The role of dilation and confining stresses in shear thickening of dense suspensions. *J. Rheol.*, 56(4):875–923, 2012.
- [150] E. B. Dussan and S. H. Davis. Motion of a fluid-fluid interface along a solid-surface. *J. Fluid Mech.*, 65:71–95, 1974.
- [151] B. Bates, C. Ancey, and J. Busson. Visualization of the internal flow properties and the material exchange interface in an entraining viscous newtonian gravity current. *Env. Fluid Mech.*, 14(2):501–518, 2014.
- [152] A. J. Hogg, M. Ungarish, and H. E. Huppert. Particle-driven gravity currents: asymptotic and box model solutions. *Eur. J. Mech. B-Fluid.*, 19(1):139–165, 2000.
- [153] C. Gladstone and A. Woods. On the application of box models to particle-driven gravity currents. *J. Fluid Mech.*, 416:187–195, 2004.

Bibliography

- [154] E. J. Watson. Boundary-layer growth. *Proc. R. Soc. Lon. Ser.-A*, 231(1184):104–116, 1955.
- [155] R. D. Skeel and M. Berzins. A method for the spatial discretization of parabolic equations in one space variable. *SIAM J. Sci. Stat. Comp.*, 11:1–32, 1990.
- [156] A. Arakawa and V. R. Lamb. Computational design of the basic dynamical processes of the ucla general circulation model. *Methods of Comp. Phys.*, 17:173–265, 1977.
- [157] B. R. Duffy, D. Pritchard, and S. K. Wilson. The shear-driven rayleigh problem for generalised newtonian fluids. *J. Non-Newton. Fluid*, 206:11–17, 2014.
- [158] R. A. Bagnold. Shearing and dilatation of dry sand and singing mechanism. *Proc. R. Soc. Lon. Ser.-A*, 295(1442):219, 1966.
- [159] A. Sauret, N. J. Balmforth, C. P. Caulfield, and J. N. McElwaine. Bulldozing of granular material. *J. Fluid Mech.*, 748:143–174, 2014.
- [160] W. Steinkogler, B. Sovilla, and M. Lehning. Influence of snow cover properties on avalanche dynamics. *Cold Reg. Sci. Technol.*, 97:121–131, 2014.

We can only see a short distance ahead,
but we can see plenty there that needs to be done.

— Alan Turing, 1950

BELINDA MARGARET BATES

Nationality: *British*

D.O.B: *10/11/1986*

Applied mathematician specialising in the modelling of geophysical hazards

Contact: 1belindabates@gmail.com

EDUCATION	<p>PhD, Doctoral Programme in Mechanics <i>École Polytechnique de Lausanne, Switzerland, 2011 - 2015</i></p> <p>MSc Atmosphere, Ocean and Climate (Distinction) <i>University of Reading UK, 2010 - 2011</i></p> <p>MMath Mathematics (Class I), BA Mathematics (Class I) <i>Lincoln College, University of Oxford UK, 2005 - 2009</i></p>
LANGUAGES	<p>English: Native Language</p> <p>French: Fluent</p> <p>German: CEFR level B1-B2, Intermediate</p>
PUBLICATIONS	<ul style="list-style-type: none">• Bates, B., Ancey, C. & Busson, J. (2013), Visualization of the internal flow properties and the material exchange interface in an entraining viscous Newtonian gravity current, <i>Environmental Fluid Mechanics</i>• Coutu, S., Kramer, S., Bates, B. & Roudier, P. (2013), Assessing dominant uncertainties in urban buildup/washoff processes under climate change: A case study in Western Switzerland, <i>Urban Climate</i>• Bates, B. Andreini, N. & Ancey, C. (2015), Basal entrainment by viscous gravity currents: theory and experiments, <i>in preparation</i>• Bates, B. & Ancey, C. (2015), Entrainment by viscoplastic avalanches on slopes: controls and effects, <i>in preparation</i>• Bates, B. & Ancey, C. (2015), Entrainment by viscoplastic avalanches on slopes: a Herschel Bulkley lubrication model incorporating an entrainable layer, <i>in preparation</i>
CONFERENCE PROCEEDINGS	<ul style="list-style-type: none">• Bates, B., C. Ancey & J. Busson, 2012. AGU Fall Meeting, San Francisco. Laboratory-Scale Dam-Break Study of Gravity Currents with Basal Entrainment: PIV Measurements of a Viscous Newtonian Fluid over a Horizontal Bed of the same fluid showing Erosion and Deposition.

	<ul style="list-style-type: none"> • Bates, B. & C. Ancey, 2013. EGU General Assembly, Vienna. Effect of available entrainable material on a viscous gravity current including run-out characteristics and internal flow properties. • Bates, B. & C. Ancey, 2014. EGU General Assembly, Vienna. Entraining avalanches on slopes: results from experiments using PIV on viscoplastic gravity currents. • Bates, B. & C. Ancey, 2014. EGU General Assembly, Vienna. A model for entrainment in avalanches and debris flows from PIV measurements of viscous gravity currents. • Bates, B. & C. Ancey, 2015. EGU General Assembly, Vienna. A viscoplastic lubrication model for entrainment by avalanches and debris flows, and comparison with experiments. • Bates, B. & C. Ancey, 2015. EGU General Assembly, Vienna. Refractive index matched suspensions as a tool for investigating entrainment by avalanches and debris flows.
RESEARCH TOPICS	<p>Mathematical & experimental modelling of avalanches and debris flows</p> <p>Landslide-generated Tsunami</p> <p>WRF forecasting of orographic convective precipitation in the UK</p> <p>Pressure induced particle transport in curved tubes</p>
TEACHING ASSISTANT	<p>Risques hydrologiques et aménagement du territoire</p> <p>Mécanique des fluides</p> <p>Analyse II</p> <p>Ondes de crue et rupture de barrage</p> <p>Supervisor for 2 masters & 4 bachelors semester projects (EPFL)</p> <p>Supervisor for 1 research internship (ENS Paris)</p>
OTHER	<p>Founding committee member: EPFL EDME PhD Seminars, promoting links between PhD students in different branches of the EPFL Mechanics doctoral programme.</p>
AWARDS AND NOMINATIONS	<p>MSc Scholarship: Natural Environment Research Council, UK, <i>2010-2011</i></p> <p>Nomination: UK National Science, Engineering and Technology Student of the Year, Mathematics category, <i>2009</i></p>
PREVIOUS EMPLOYMENT	<p>Picnic Foods, Reading, UK. <i>2010 - 2011</i></p> <p>Oxbridge Applications, London, UK. <i>Educational consultant, 2009</i></p> <p>Collineige Luxury Chalets, Chamonix, France. <i>2009 - 2010</i></p> <p>Motor Yacht “Stromboli”, Mediterranean Sea. <i>2010</i></p> <p>Oxford Centre for Industrial and Applied Mathematics. <i>Research intern, 2008</i></p>